

**Eddy Current Pulsed Thermography for Non-Destructive Evaluation of Carbon Fibre Reinforced Plastic for Wind Turbine Blades**

**Liang Cheng, BSc MSc**

**A thesis submitted to Newcastle University in fulfilment of the requirements for the degree of Doctor of Philosophy**



**School of Electrical and Electronic Engineering  
Newcastle University**

**June 2013**

## TABLE OF CONTENTS

Table of contents .....	i
Abstract .....	iv
Acknowledgement.....	vi
List of Publications .....	vii
List of Figures .....	ix
List of Tables.....	xiv
Abbreviations .....	xv
Chapter 1. Introduction .....	1
1.1 Research background .....	1
1.2 Aims and objectives .....	2
1.2.1 Research aims.....	2
1.2.2 Research objectives .....	3
1.3 Main achievements.....	4
1.4 Thesis layout .....	4
1.5 Chapter summary .....	6
Chapter 2. Literature Survey.....	7
2.1 Reviews of failure models for wind turbine systems .....	7
2.1.1 Brief introduction to wind turbine systems and their reliability .....	7
2.1.2 Failure models for wind turbines .....	9
2.1.3 Failure in composite wind turbine blades .....	14
2.2 State-of-the-art of NDE and SHM methods relevant to composites.....	17
2.2.1 Acoustic methods .....	19
2.2.2 Fibre Optics .....	24
2.2.3 Electromagnetic methods .....	26
2.2.4 Thermographic methods.....	30
2.3 Overviews of interpretation and characterisation algorithms for ECPT .....	34
2.3.1 Optical flow for the investigation of local areas .....	35

2.3.2 PCA and ICA for pattern investigation.....	36
2.4 Chapter summary .....	37
Chapter 3. Methodology .....	40
3.1 Theoretical background of ECPT.....	41
3.1.1 Maxwell's equations.....	42
3.1.2 Heat diffusion equations .....	45
3.2 Numerical simulation models of ECPT .....	46
3.3 Experimental systems and samples for case studies .....	48
3.4 Interpretation and characterisation algorithms.....	53
3.4.1 Optical Flow for NDE at the local area level.....	53
3.4.2 PCA/ICA for NDE at the pattern level .....	56
3.5 Chapter summary .....	61
Chapter 4. ECPT Investigation at the Pixel Level.....	63
4.1 Transient response extraction at pixel level.....	63
4.2 Case study 1: crack detection and characterisation.....	65
4.2.1 Sample description .....	65
4.2.2 Numerical simulation study .....	66
4.2.3 Experimental study.....	74
4.2.4 Discussion .....	79
4.3 Case study 2: impact damage detection and characterisation .....	79
4.3.1 Sample description .....	80
4.3.2 Numerical simulation results.....	81
4.3.3 Experimental results.....	86
4.3.4 Discussion .....	91
4.4 Defect classification using ECPT investigation at pixel level .....	92
4.5 Chapter summary .....	94
Chapter 5. ECPT Investigation at the Local Area Level .....	96
5.1 Optimisation of Optical Flow for ECPT .....	96
5.1.1 Time slot selection of OF for defect characterisation.....	96
5.1.2 Threshold selection for optical flow .....	98
5.2 Defect classification at local area level .....	99
5.2.1 Thermal images of three types of defects .....	99
5.2.2 Optical flow results .....	101
5.2.3 Discussion .....	107
5.3 Case study 3: QNDE for impact damage .....	107

5.4 Case study 4: Uni-directional sample under directional tensile stress.....	111
5.5 Chapter summary .....	114
Chapter 6. ECPT Investigation at the Pattern Level.....	116
6.1 ECPT investigation at the pattern level using PCA .....	117
6.1.1 Cracks.....	117
6.1.2 Impact damages.....	119
6.1.3 Delaminations .....	120
6.1.4 Discussions.....	122
6.2 ECPT investigation at pattern level using ICA .....	122
6.3 Chapter summary .....	130
Chapter 7. Conclusion and future work.....	132
7.1 Conclusion .....	132
7.1.1 Failure models and state-of-the-art of NDE for composite blades .....	133
7.1.2 Numerical modelling and the experimental system .....	134
7.1.3 ECPT investigation at the three levels .....	134
7.2 Future work .....	139
7.2.1 System refinement and reduction in size for online monitoring .....	139
7.2.2 Automatic defect identification and characterisation.....	140
7.2.3 3D reconstruction of defects and material properties .....	141
List of References .....	142

## ABSTRACT

The use of Renewable energy such as wind power has grown rapidly over the past ten years. However, the poor reliability and high lifecycle costs of wind energy can limit power generation. Wind turbine blades suffer from relatively high failure rates resulting in long downtimes. The motivation of this research is to improve the reliability of wind turbine blades via non-destructive evaluation (NDE) for the early warning of faults and condition-based maintenance. Failure in wind turbine blades can be categorised as three types of major defect in carbon fibre reinforced plastic (CFRP), which are cracks, delaminations and impact damages. To detect and characterise those defects in their early stages, this thesis proposes eddy current pulsed thermography (ECPT) NDE method for CFRP-based wind turbine blades. The ECPT system is a redesigned extension of previous work. Directional excitation is applied to overcome the problems of non-homogeneous and anisotropic properties of composites in both numerical and experimental studies. Through the investigation of the multiple-physical phenomena of electromagnetic-thermal interaction, defects can be detected, classified and characterised via numerical simulation and experimental studies.

An integrative multiple-physical ECPT system can provide transient thermal responses under eddy current heating inside a sample. It is applied for the measurement and characterisation of different samples. Samples with surface defects such as cracks are detected from hot-spots in thermal images, whereas internal defects, like delamination and impact damage, are detected through thermal or heat flow patterns.

For quantitative NDE, defect detection, characterisation and classification are carried out at different levels to deal with various defect locations and fibre textures. Different approaches for different applications are tested and compared via samples with crack, delamination and impact damage. Comprehensive transient feature extraction at the three different levels of the pixel, local area and pattern are developed and implemented with respect to defect location in terms of the thickness and complexity of fibre texture. Three types of defects are detected and classified at those three levels. The transient responses at pixel level, flow patterns at local area level, and principal or independent components at pattern level are derived for defect classification. Features at the pixel

and local area levels are extracted in order to gain quantitative information about the defects. Through comparison of the performance of evaluations at those three levels, the pixel level is shown to be good at evaluating surface defects, in particular within unidirectional fibres. Meanwhile the local area level has advantages for detecting deeper defects such as delamination and impact damage, and in specimens with multiple fibre orientations, the pattern level is useful for the separation of defective patterns and fibre texture, as well as in distinguishing multiple defects.

## ACKNOWLEDGEMENT

I would like to express my sincere appreciation to a number of people who have helped me during the past years of PhD study. Firstly, special thanks to Prof. Gui Yun Tian, my supervisor, for giving hints on the work, and providing regular help and guidance on the project.

I would like to thank my colleagues, Dr. John Wilson, Dr. Yong Li, Dr. Ilham Mukriz Zainal Abidin, Mr. Mohammed Alamin, Prof. Xianzhang Zuo, Mr. Hong Zhang, Dr. Yunze He, Mr. Libing Bai, Prof. Mengchun Pan, Dr. Aijun Yin, Dr. Bin Gao and all in the Sensor Technology research team at Newcastle University, who have provided fruitful discussion and advice on both simulation and experiment.

Special appreciations to the Engineering and Physical Sciences Research Council (EPSRC), and the Frame Programme 7 (FP7) for funding me to undertake the research projects entitled ‘Future reliable renewable energy conversion systems & networks: A collaborative UK-China project’ (EP/F06151X/1) and ‘Health Monitoring of Offshore Wind Farms’ (FP7-PEOPLE-2010-IRSES, 269202), and School of Electrical and Electronic Engineering, Newcastle University for assistance with simulation and experimental work.

My deepest thanks go to my parents and families, for always supporting and encouraging me during my education. Also I would like to thank my girlfriend, Miss Sining Meng, for always being along with me during my PhD study.

Last but not least, I offer my regards and blessing to all those who support me in any respect during the completion of the study.

## LIST OF PUBLICATIONS

### Journal Papers

- [J1]. L. Cheng and G.Y. Tian, "Surface crack detection for carbon fibre reinforced plastic (CFRP) materials using pulsed eddy current thermography", *IEEE Sensors Journal*, vol. 11, No. 12, pp. 3261-3268, 2011.
- [J2]. L. Cheng and G.Y. Tian, "Comparison of nondestructive testing methods on detection of delaminations in composites", *Journal of Sensors*, vol. 2012, Article ID 408437, pp. 1-7. DOI:10.1155/2012/408437, 2012.
- [J3]. L. Cheng and G.Y. Tian, "Transient thermal behaviour of eddy current pulsed thermography for non-destructive evaluation of composites", *IEEE Transaction on Instrumentation and Measurement*, vol. 62, issue 5, pp. 1215-1222, 2013.
- [J4]. Z.J. Wan, L.B Liao, G.Y. Tian and L. Cheng, "Investigation of drag effect using the field signature method", *Measurement Science and Technology*, vol. 22, issue 8, 085708, 2011.
- [J5]. G.Y. Tian, J. Wilson, L. Cheng, D.P. Almond, E. Kostson and B. Weekes, "Pulsed eddy current thermography and applications", *New Developments in Sensing Technology for Structural Health Monitoring*, vol. 96, pp. 205-231, DOI: 10.1007/978-3-642-21099-0\_10, 2011.
- [J6]. G.Y. Tian, Y. He, L. Cheng, P. Jackson, "Pulsed eddy current thermography for corrosion characterisation", *International Journal of Applied Electromagnetics and Mechanics*, vol. 39, Issue 1, pp. 269-276, 2012.



## Conference Papers

- [C1]. L. Cheng, G.Y. Tian and B. Szymanik, “Feasibility studies on microwave heating for non-destructive evaluation of glass fibre reinforced plastic composites”, *Proceedings of IEEE International Instrumentation and Measurement Technology Conference, I<sup>2</sup>MTC*, China, pp. 47-52, May 2011.
- [C2]. L. Cheng and G.Y. Tian, "Pulsed electromagnetic NDE for defect detection and characterisation in composites," *Proceedings of IEEE International Instrumentation and Measurement Technology Conference, I<sup>2</sup>MTC*, Austria, pp. 1902-1907, May 2012.
- [C3]. G.Y. Tian, L. Cheng, M. Alamin, H. Zhang and Y. He, “Electromagnetic non-destructive methods for corrosion characterisation”, *ISEM 2011-15th International Symposium on Applied Electromagnetics and Mechanics*, Napoli, Italy, Sep 2011.
- [C4]. Y. He, G.Y. Tian, L. Cheng, H. Zhang and P. Jackson, “Parameters influence in steel corrosion evaluation using PEC thermography”, *Proceedings of the 17<sup>th</sup> International Conference on Automation & Computing*, Huddersfield, UK, Sept 2011.
- [C5]. Y. He, G. Tian, L. Cheng, H. Zhang, and P. Jackson, “Corrosion characterisation under coating using pulsed eddy current thermography”, in *50th Annual Conference of The British Institute of Non-Destructive Testing*, Telford, UK, 2011.

## LIST OF FIGURES

Figure 2.1 Configuration of wind turbines ( <a href="http://www.nwip.org">http://www.nwip.org</a> ) .....	8
Figure 2.2 Failure causes, modes and relevant condition monitoring methods for major components in wind turbine systems. ....	10
Figure 2.3 Data from a survey of failure in wind power systems [13] .....	11
Figure 2.4 Statistics of failure rates and downtimes per failure comparison for critical subsystem of wind turbines [15] .....	12
Figure 2.5 The Bathtub curve [15].....	13
Figure 2.6 The main elements of a wind turbine blade [8] .....	15
Figure 2.7 A sketch illustrating some of the common types of damage found in a wind turbine blade [8] .....	16
Figure 2.8 Category of NDE techniques reviewed in this thesis. ....	19
Figure 2.9 Schematic diagram of pulse-echo ultrasonic technique.....	20
Figure 2.10 Schematic representation of AE signal [51]: 1. Maximal amplitude of pulse, 2. Noise level, 3. Voltage, 4. Single oscillations, 5. Standard deviation of amplitude, 6. Interval between pulses, 7. Discrimination level, 8. Time, 9. Pulse duration, 10. Events. ....	22
Figure 2.11 The propagation of light through a fibre optic [56].....	24
Figure 2.12 The principle of eddy currents .....	26
Figure 2.13 The principle of MFL .....	28

Figure 3.1 Research diagram for ECPT .....	41
Figure 3.2 ECPT system diagram .....	48
Figure 3.3 Experimental setting-up at Newcastle University .....	49
Figure 3.4. (a) Rectangular coil used in Newcastle and (b) circular coil used in NUAA .....	50
Figure 3.5 Experimental set-up at NUAA.....	51
Figure 3.6 Illustration of (a) transmission mode and (b) reflection mode .....	52
Figure 3.7 Procedure for defect identification and separation .....	57
Figure 3.8 PCA procedure with thermal videos.....	58
Figure 4.1 Illustration of capture of transient temperature response from a thermal image sequence. ....	64
Figure 4.2 Cracked sample (a) photograph ; (b) diagram of the fibre texture in top view. .....	65
Figure 4.3 (a) 3D geometry setup of numerical model in COMSOL; (b) 2D side view of sample with crack.....	66
Figure 4.4 Simulation results of thermal images at the maximum heating (200 ms) for a crack with $w=1$ mm and $d= 2$ mm.....	68
Figure 4.5 Simulation results for transient temperature against time at “pos 1” shown in Figure 4.3 at the crack bottom for varied crack depth at crack width $w=1$ mm: (a) normalised responses; (b) non-normalised (raw) responses. ....	70
Figure 4.6 The amplitude of temperature rise (a) versus crack depth $d$ . ....	72
Figure 4.7 Simulation results for transient temperature against time at “pos 1” shown in Figure 1 at crack bottom for varied crack width at crack depth $d = 2$ mm: (a) normalised responses; (b) non-normalised (raw) responses. ....	73

Figure 4.8 Thermal image of sample at maximum heating for: (a) horizontal current excitation; (b) vertical current excitation .....	75
Figure 4.9 Experimental results of thermal image at the maximum heating (200ms) for 2mm deep and 1mm wide crack.....	76
Figure 4.10 Experimental results for transient temperature change against time at “pos 1” as shown in Figure 4.9 at crack bottom for cracks with $w = 1$ mm and varied depths: (a) normalised responses; (b) non-normalised (raw) responses. ....	78
Figure 4.11 (a) a photograph of impacted sample; (b) scheme of 5HS carbon fibre woven. ....	80
Figure 4.12 Geometry of sample and impact damage, marked in blue.....	81
Figure 4.13 (a) Transient temperature and (b) first derivatives at the origin $(x, y, z) = (0, 0, 0)$ . ....	84
Figure 4.14 $dT/dt$ against variation in electrical conductivity at $t=0.1$ s (red line with crosses); and $(dT/dt)/T(0.2)$ averaging from 0.2s to 1s against variation in thermal conductivity (blue line with dots). ....	86
Figure 4.15 Thermal image of the sample with 8J impact at 0.2s showing the point investigated. ....	87
Figure 4.16 Transient temperature at impact point against time: (a) non-normalised response; (b) normalised response and 1 <sup>st</sup> derivatives of temperature; (c) non-normalised response; (d) normalised response. ....	89
Figure 4.17 Impact energy against average $dT/dt$ , which stands for variation in electrical conductivity (red line with crosses); and against $(dT/dt)/T(0.2)$ which stands for variation in thermal conductivity (blue line with dots).....	90
Figure 4.18 Picture under microscope of impact area in 12J sample.....	91
Figure 4.19 PCA classification for cracks, impact damages and delaminations at the pixel level.....	93

Figure 5.1 Number of pixels with OF amplitudes over the threshold 'thres' =5.5 against time.....	97
Figure 5.2 Specific time in a typical transient thermal response (temperature response in blue and the first derivative of temperature in red).....	98
Figure 5.3 (a)Thermal image for 12J-impaced sample from “Set 3” at maximum heating, where the unit is digital level (DL) and OF amplitude maps with varing thresholds: (b) thres =5; (c) thres =5.5; (d) thres =8. ....	99
Figure 5.4 Thermal images at maximum heating for (a) crack, (b) impact damage, (c) delamination. The marked area 1 in each image shows the defective region and area 2 indicates the defect-free region. ....	100
Figure 5.5 Optical flow distribution images at the end of heating compared with thermal images within “Area 1” in Figure 5.4 for: (a) crack, sample Set 1, (b) impact damage, sample Set 2, (c) delamination, sample Set 4 respectively. Transmission mode is used. The time-slot for optical flow is from 175 ms to 200 ms. The length and direction of arrows in figures denote the magnitude and orientation of heat flow.....	102
Figure 5.6 (a) Schematic of heat propagation at the crack in top and cross-section views; (b) simulation result of heat flux density for 2 mm deep crack, cross- section view....	104
Figure 5.7 Simulation results of heat flux density in (a) top view and (b) cross-section view along the central horizontal line as shown in (a).....	106
Figure 5.8 Schematic of heat propagation at delamination in top and cross-section views .....	107
Figure 5.9 Optical flow images at the end of heating compared with thermal images within selected regions for samples with (a) 4J, (b) 6J, (c) 8J, (d) 10J, (e) 12J impact energies. Transmission mode is used. The time-slot for optical flow is from 175 ms to 200 ms. The purple arrows denote the OF with the amplitude above the threshold....	109
Figure 5.10 Pixel number (area) above OF threshold vs impact energy at maximum heating time.....	110
Figure 5.11 Woven structure of sample set 3.....	111

Figure 5.12 Instron model 3369 universal test machine and Flir thermal camera. ....	112
Figure 5.13 Thermal images for the sample under tensile stress at maximum heating (the fixed line with respect to the pin marker is in red; the horizontal and vertical coordinates denote the $x$ and $y$ position in the thermal image). ....	112
Figure 5.14 Optical flow at end of heating along the red line marked in Figure 5.13: (a) amplitude for overall flow; (b) amplitude in horizontal direction; (c) amplitude in vertical direction. Frame interval is 10. The $y$ position 0 denotes the top of the line and position 256 denotes the bottom of the line. ....	113
Figure 6.1 (a) 1 <sup>st</sup> PC; (b) 2 <sup>nd</sup> PC; (c) 3 <sup>rd</sup> PC; (d) 4 <sup>th</sup> PC of PCA for the thermal sequences in heating phase. ....	118
Figure 6.2 (a)-(h): 1 <sup>st</sup> -8 <sup>th</sup> PCs of PCA for the thermal sequences in heating phase, rear of the sample. ....	120
Figure 6.3(a) 1 <sup>st</sup> PC; (b) 2 <sup>nd</sup> PC; (c) 3 <sup>rd</sup> PC; (d) 4 <sup>th</sup> PC of PCA for the thermal sequences in heating phase; (e) numbered delaminations and fibre orientation definition. ....	121
Figure 6.4 Thermal image on the back side of the impact damage sample (sample set 2) at 200ms, reflection mode. ....	123
Figure 6.5 Coil positions and recorded areas for 'impact' and 'non-defect' videos .....	127
Figure 7.1. Flow chart for selection of investigation levels .....	138
Figure 7.2 Matlab GUI for thermal video display and processing .....	140

## LIST OF TABLES

Table 2-I Typical damage to wind turbine blades [8], [27], [35]-[37].....	17
Table 2-II Parameters of AE and their informative content [51].....	22
Table 3-I Defect descriptions and sample selections .....	52
Table 4-I Description of impacted samples .....	80
Table 4-II Electrical and thermal conductivities settings for simulation .....	83
Table 6-I MMCA results for impact damage, rear side of sample set 2: the first eight ICs and their mixing vectors.....	125
Table 6-II MMCA results for 'non-defect' video, rear side of sample set 2: the first eight ICs and their mixing vectors .....	128
Table 6-III Cross-Correlation between the mixing vectors from the 'impact' and the 'non-defect' videos.....	130
Table 7-I Comparison and merits of three investigation levels .....	135

## ABBREVIATIONS

AE	Acoustic Emission
CFRP	Carbon Fibre Reinforced Plastic
DL	Digital Level
ECPT	Eddy Current Pulsed Thermography
EM	Electromagnetic
EPSRC	Engineering and Physical Sciences Research Council
FBG	Fibre Bragg Grating
FDTD	Finite Difference Time Domain
FEM	Finite Element Method
FIT	Finite Integral Technology
FO	Fibre Optics
GFRP	Glass Fibre Reinforced Plastic
GUI	Graphic User Interface
HTS-SQUID	High Temperature Superconductor -SQUID
ICA	Independent Component Analysis
IR	Infrared
LCA	Life Cycle Assessment
MFEC	Multi-frequency Eddy Current
MFL	Magnetic Flux Leakage
MMCA	Multichannel Morphological Component Analysis
NDT&E	Non-Destructive Testing and Evaluation
NREL	National Renewable Energy Laboratory
NUAA	Nanjing University of Aeronautics and Astronautics
OF	Optical Flow
PC	Principal Component
PCA	Principal Component Analysis
PEC	Pulsed Eddy Current



PN <sub>OF</sub>	Pixel Number of OF above the Threshold
POF	Plastic Optical Fibre
PZT	Piezoelectric Transducer
QNDE	Quantitative Non-Destructive Evaluation
ROI	Region of Interest
SHM	Structural Health Monitoring
SNL	Sandia National Laboratory
SNR	Signal-to-Noise Ratio
TSR	Thermographic Signal Reconstruction

## Chapter 1. INTRODUCTION

### 1.1 Research background

Electrical power generation from renewable sources, mainly wind, has grown rapidly over the past ten years. However, the key feature that differentiates renewable energy from conventional power generation is the inherent fluctuation of its sources. Research indicates that, in the case of wind power, this gives rise to products with poor reliability and high lifecycle costs [1]-[4].

This research is part of a collaborative UK-China project supported by the Engineering and Physical Sciences Research Council (EPSRC) entitled ‘Future reliable renewable energy conversion systems & networks’. The participants in this UK-China consortium are based at five UK universities (Edinburgh, Durham, Newcastle, Nottingham and Warwick), five Chinese universities (Chongqing, Sichuan, Tsinghua, Zhejiang, and Nanjing University of Aeronautics and Astronautics) and several other organisations (New & Renewable Energy Centre, Control Techniques, EM Renewables and Converteam from the UK, and GE Research, Goldwind and Mott MacDonald from China).

This research concentrates on failure models and life cycle assessment (LCA) with the help of non-destruction testing and evaluation (NDT&E) for wind turbine blades in a wind power system. Wind turbine blades are normally made from composite materials such as glass fibre reinforced plastic (GFRP) or carbon fibre reinforced plastic (CFRP). Because of extreme environment conditions such as lightning, icing, storms, as well as bird strikes, wind turbine blades suffer from damage, which often results in the operational failure of wind power systems. In order to improve the reliability of wind turbine blades, failure models and NDT&E are required because failure models can give knowledge about weak points and failures, where NDT&E will provide qualitative and quantitative information useful in detecting faults at the early stages so that the critical

damage to important and expensive components can be prevented. The failure of wind turbine blades is mainly caused by crack, delamination and impact damage. In this thesis, one NDT&E approach, the so-called eddy current pulsed thermography (ECPT), is proposed as a tool to interpret and characterise these types of defect or damage in CFRP wind turbine blades through simulation and experiment.

Three challenges have arisen for defect detection and characterisation in CFRP using NDT&E approaches: (1) the non-homogenous and anisotropic properties and multiple-layered structure in CFRP materials; (2) the detection and classification of different types of defects at the surface or inside samples; (3) the quantitative non-destructive evaluation (QNDE) of different defects and in various fibre textures. To address these issues, an integration of two NDE techniques, eddy current and thermography, is implemented to maximise the advantages of the two techniques, which are that they are non-contact, rapid and directional, allowing large-scale inspection. Previous research has illustrated the capability of ECPT in detecting surface defects in homogeneous metallic specimens, but not much attention has been paid to the above three issues.

To address the above challenges, the research fulfils: (1) a failure model analysis of composite wind turbine blades; (2) numerical modelling and experimental ECPT system development; (3) comprehensive transient feature extraction at the pixel, local area and pattern levels to give time-spatial information as well as defect classification and characterisation, based on multiple-physical phenomena through numerical modelling and experimental studies.

## **1.2 Aims and objectives**

### ***1.2.1 Research aims***

The aims of the research are: (1) to understand and analyse failure models for wind power systems; and (2) to develop an NDT&E system for wind turbine blades, especially for CFRP blades, to achieve defect detection and characterisation. Based on failure models and numerical simulations, a novel system is to be designed which includes sensor selection and configuration, data acquisition and processing, and defect characterisation according to feature extraction and pattern recognition. The classification and quantitative information about defects are achieved dealing with

varied defect locations and fibre textures at the pixel level, local area level and pattern level.

### ***1.2.2 Research objectives***

The objectives of this project are listed as follows:

- To undertake a literature survey on wind power systems, failure models, NDT&E, and SHM, as well as the state-of-the-art in relevant numerical and experimental research in this areas;
- To design and develop a sensing and imaging system for wind turbine blades made from CFRP, which includes the elements below:
  - to re-design eddy current pulsed thermography (ECPT) systems for non-homogeneous and anisotropic materials, *e.g.* CFRP materials and to develop 3D finite element method (FEM) numerical models concerning the visualisation and mapping of transient temperature responses and multiple physics distribution, including electromagnetic field distribution, Joule heating and the resultant temperature distribution;
  - to develop feature extraction algorithms from transient thermal responses at the pixel level and to demonstrate QNDE for defect detection and quantification through case studies, and to verify the experimental results with FEM numerical models;
  - to implement heat flow analysis at the local area level to extract flow features from thermal image sequences for defect detection, classification and quantification, comparing the three types of defects of crack, delamination and impact damage in different fibre textures;
  - to apply algorithms to extract abnormal patterns from thermal image sequences at the pattern level for defect classification and QNDE for crack, delamination and impact damage;
  - To compare the processing algorithms used at different levels and to identify the most suitable processing level under different conditions for various types of defects and complexities of fibre texture.

### 1.3 Main achievements

The main achievements of the research are:

- Undertaking a literature survey which provides failure models for wind power systems, and wind turbine blades in particular; and identifying the major types of damage to CFRP wind turbine blades, which are crack, delamination and impact damage; reviewing the state-of-the-art of NDT&E techniques for composite materials and proposing an ECPT technique;
- Re-designing experimental systems and 3D FEM numerical models of ECPT inspections on CFRP composite materials in an effort to: (1) reveal the electromagnetic and thermal phenomena occurring within specimens as well as their interaction with defects in non-homogeneous and multi-layered specimen; and (2) analyse the transient temperature responses and extract their features;
- Determining successful approaches to defect detection and characterisation via the evaluation of algorithms at the pixel, local area and pattern levels for the characterisation of crack, delamination and impact damage. The research identifies the most suitable evaluation level depending on the defect type and fibre texture complexity, solving non-homogeneous and anisotropic problems in composites:
  - The pixel level is the most efficient for identifying surface defects such as cracks, in particular within uni-directional fibres;
  - The local area level has advantages for evaluating inner defects such as delamination and impact damage in specimens with multiple fibre orientations;
  - The pattern level is effective at separation of defective patterns and fibre texture or distinguishing multiple defects, especially in complex fibre textures.
- Implementing defect classification through features of transient thermal responses at the pixel level, flow patterns at the local area level and defect patterns at the pattern level; and realising QNDE of the area and diameter of defects;
- Publishing papers in journals and presenting the work at conferences.

### 1.4 Thesis layout

Chapter 1 describes the research background, the aims and objectives of the research, and the main achievements related to the work, as well as an outline of the thesis.

Chapter 2 begins with reviews of failure models for wind turbine systems, and especially wind turbine blades, to identify the major defects leading to failure. The state-of-the-art NDT&E methods used for wind turbine blades are presented. An overview and comparison of the direction and capabilities of the NDT&E and QNDE approaches related to composite materials, CFRP in particular, is then presented. Focusing on the ECPT technique, algorithms at the pixel, local area and pattern levels are reviewed and discussed. A summary of the literature review is provided at the end of the chapter with a discussion on the problems identified which are the focus of the study.

Chapter 3 presents a theoretical background to electromagnetic NDE (EMNDE) and thermography, which begins with an introduction to Maxwell's governing equations and the heat diffusion equations, followed by the governing equations for EM and thermal phenomena in EMNDE. FEM numerical simulation in solving multi-physics problems is then introduced along with its advantages over other methods with respect to the complexities of defect location and fibre texture. Furthermore, the research methodology used in the thesis is presented in this chapter, which outlines the numerical modelling approach and experimental designs in conjunction with the relevant processing algorithms at the pixel, local area and pattern levels respectively.

Chapter 4 illustrates the defect characterisation investigation at pixel level via the ECPT technique, including numerical and experimental studies. Two case studies comparing different complexities of defects and fibre texture are reported for crack and impact damage. For crack case, features are extracted from transient temperature responses at selected pixels to quantify the depth and width of cracks. For impact damage case, the results reveal problems and inaccuracies due to the interior defect with an irregular shape, blurred hot-spots and a more complex fibre texture, which leads to the need for further processing algorithms at the local area and pattern levels as shown in Chapters 5 and 6. The advantages and disadvantages of pixel level investigation are then discussed.

Chapter 5 elaborates the defect classification and QNDE investigation at the local area level via optical flow (OF) algorithms used in order to evaluate deeper defects, such as delamination and impact damage. Flow patterns at defective regions for crack, delamination and impact damage are retrieved respectively and used for defect classification at the local area level. Moreover, an OF investigation on a case study of impact damage is carried out to estimate defective area against impact energy. In addition, variations in physical properties in CFRP with uni-directional fibre orientation

are quantified via OF. As to samples with multiple fibre orientation or more complex textures, the use of OF shows the shortcomings of the analysis of physical property variations, which leads to the pattern level investigation reported in Chapter 6. The advantages and disadvantages of local area level investigation are then discussed.

Chapter 6 gives details of the study of the pattern recognition of defects and fibre textures using principal component analysis (PCA) and independent component analysis (ICA) at the pattern level to allow the evaluation of defects within complex fibre texture. A case study of impact damage and its resultant delamination is conducted to show the multiple-defected condition in complex fibre texture. Defect patterns and fibre texture patterns are obtained and identified into different independent components. The advantages and disadvantages of pattern level investigation using PCA and ICA are then considered.

Chapter 7 summarises the research work with conclusions from the findings and the major contributions made to NDT&E. Future work based on the current investigation is proposed.

### **1.5 Chapter summary**

This chapter introduces the research work which has been conducted on “eddy current pulsed thermography for non-destructive evaluation for wind turbine blades” as part of a UK-China collaborative project. The research background is elaborated and the aims and objectives of the research are presented. The major contributions of the research are listed, and the layout of this thesis and the contents of each chapter are briefly summarised.

## Chapter 2. LITERATURE SURVEY

Having given a general introduction to this thesis, this chapter begins with reviews of failure models for wind turbine systems, including a brief introduction to these systems and their reliability, a summary of failure models for wind turbines as well as for wind turbine blades which are identified as a most crucial component with relatively high failure rates and long consequent downtimes. In order to improve the reliability of wind turbine blades, the NDE approach is a powerful tool to investigate the health condition of and existence of damage in blades. Thus, the state-of-the-art of NDE methods for composite blades is subsequently discussed in terms of their through acoustic, optic, electromagnetic and thermographic aspects. Though comparison of the advantages and disadvantages of current NDE methods, a hybrid technique, the so-called ECPT, is proposed in this thesis. This aims to quantify damages or defects in composite blades, and therefore the interpretation and characterisation algorithms of QNDE are reviewed.

### 2.1 Reviews of failure models for wind turbine systems

#### *2.1.1 Brief introduction to wind turbine systems and their reliability*

According to their location, wind turbine systems can be categorised as onshore or offshore. Onshore systems suffer fewer failures, whereas offshore turbines generate more electricity due to their larger dimensions and the stronger winds present in large open spaces without restrictions caused by the environment, noise limits and urban planning. In terms of axis orientation, there are horizontal and vertical axis wind turbines. Horizontal axis wind turbines are more popular due to the higher efficiency of electricity generation.



Taking the horizontal axis wind turbine as an example, a typical configuration is shown in Figure 2.1. The rotor blade converts the kinetic energy of the wind into mechanical power, and then rotating speed is shifted at the gearbox. Subsequently the mechanical power is converted into electric energy by a generator [1]. The AC electricity is converted into DC at a converter and then independently modulated to a certain frequency of AC compatible with the utility grid [2]. A pitch drive is used to change the angle of the blade in order to enhance the wind harvest, and a yaw system aims to adjust the nacelle to increase the efficiency and can also protect the wind turbines.

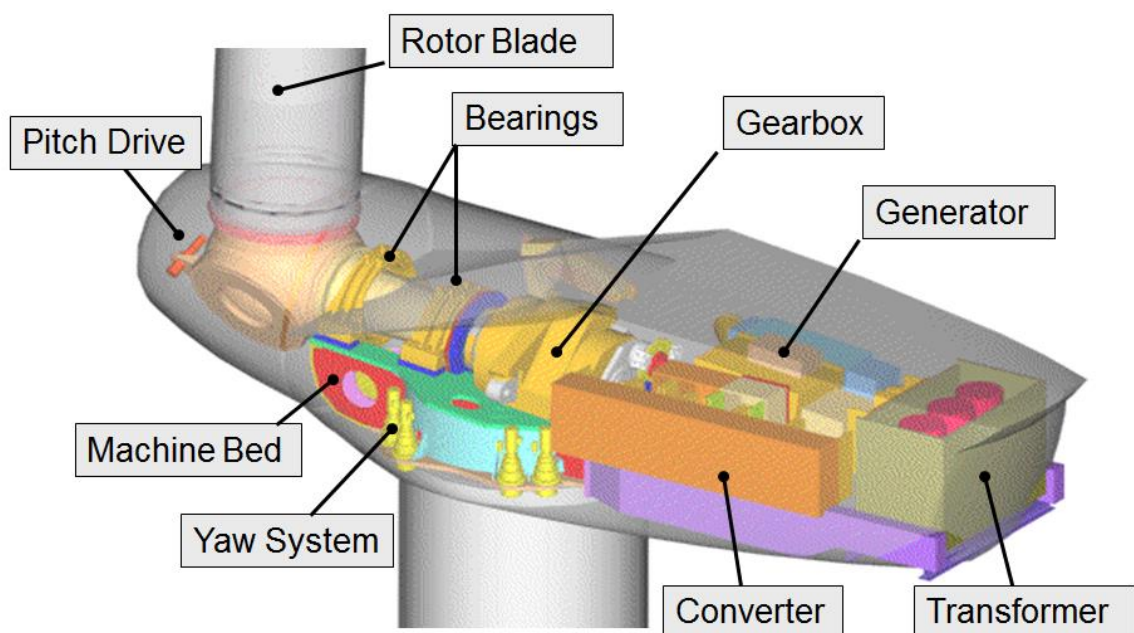


Figure 2.1 Configuration of wind turbines (<http://www.nwip.org>)

The key problem in wind energy conversion systems is the inherent fluctuation of winds. Variations in wind not only have a major effect on power output but also lead to sharp changes in either mechanical or electrical conditions, which are the primary causes of poor reliability and high lifecycle costs. The failure rate of wind turbines is three times higher than that of conventional generators, and the maintenance costs are also much higher, especially for offshore turbines [3]. The very large size of offshore turbines, and severe environments, including very large variation in temperature at wind farms [4], lighting, rain, storm, *etc.*, as well as the difficulty of access to offshore turbines, also

cause high failure rates, long downtimes and expensive repair costs. In next sub-section, failure models for wind turbines will be summarised in order to identify the major problems involved.

### ***2.1.2 Failure models for wind turbines***

Any component of a wind turbine can suffer damage. Cases of structural damage on wind turbines are reported from time to time, and the purpose of using failure models is to identify critical components and to determine where and how often failure occurs as well as how long it takes to repair, to characterise and understand failure modes and causes. With information from the literature survey [5]-[12], a failure map for wind turbines is summarised in Figure 2.2, which illustrates different major critical components and regions as well as the relevant failure models and popular methods for failure monitoring.

From the literature survey, it is clear that approaches for further study are required to give information about the causes of failures, how they occur and where damage is most likely to occur. In this research, further study of wind turbine blades is conducted for various reasons: the blade is one of the components which has the highest failure rate known from failure model analysis; and the mean downtime for repair is relatively long [4], [13]; the cost involved in repairing damage to blades is also the highest and the blade itself is very expensive, accounting for 15-20% of total turbine cost [14]. In particular, offshore turbine blades are larger than onshore ones, and as the size of blades increases, the failure rates and repair costs are much higher.

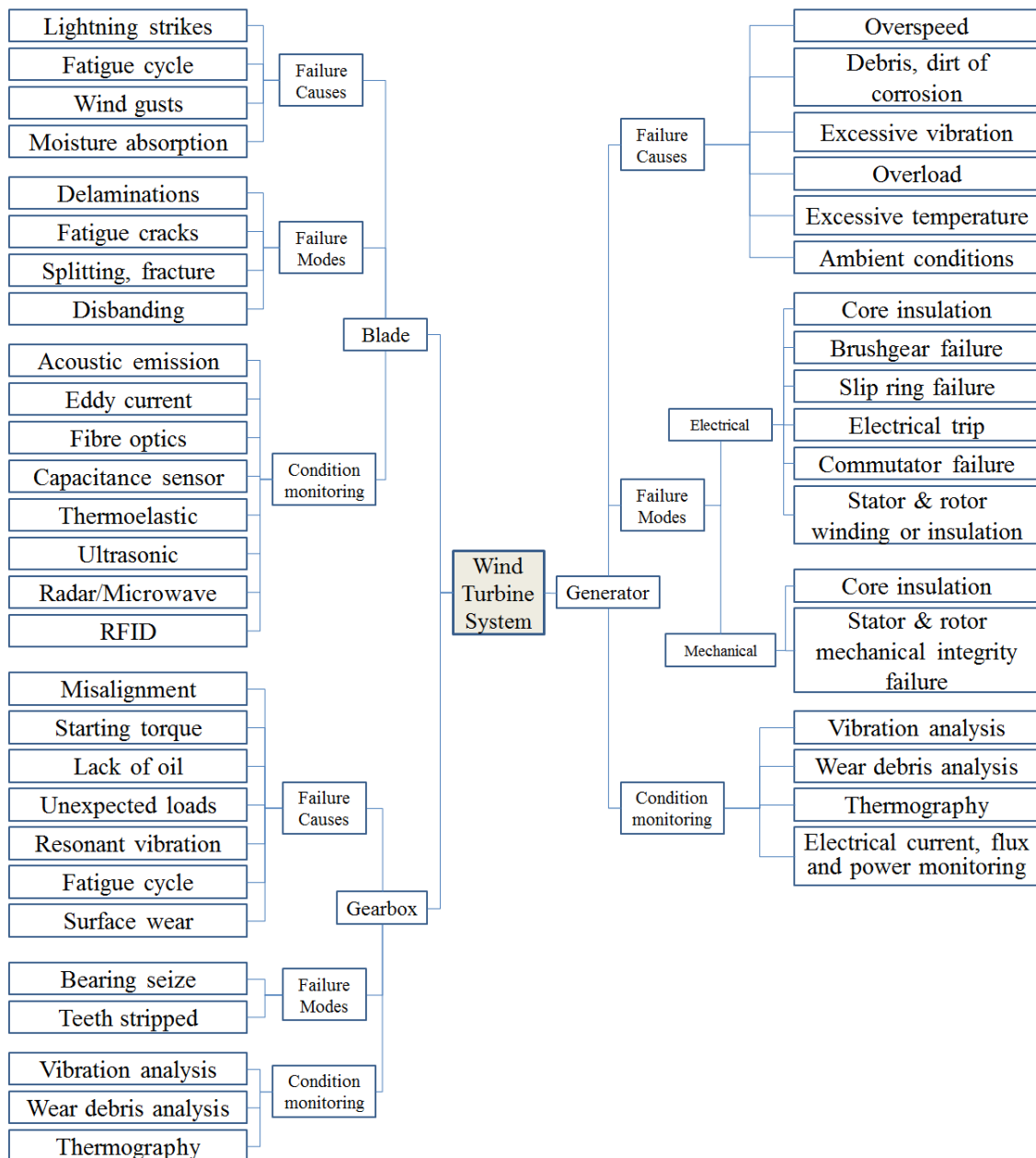


Figure 2.2 Failure causes, modes and relevant condition monitoring methods for major components in wind turbine systems.

Through the literature survey, three approaches for research on failure models and reliability are summarised below:

- (1) Historical statistical data can be used to analyse failure in different components/systems and to build failure models. Surveys have been conducted of the failure rates of components of wind turbine sited in Sweden, Finland, Germany and Denmark [4], [13], as shown in Figure 2.3. The data shown in Figure 2.4 were obtained

from Landwirtschaftskammer (LWK in the figure), Wissenschaftliche Mess- und Evaluierungsprogramm (WMEP) and Swedish [15] over a relative longer period. From the figure, it can be found that the component with the highest failure rate in Sweden, LWK and WMEP is the electric system, meanwhile hydraulic system are yaw system are components with the highest failure rate in Finland and Denmark, respectively. Gearboxes, blades, control systems are also have high failure rates in these countries. From Figure 2.4, it is also clear that faults in blades, generator, gearbox, yaw system and drive train have relatively long downtimes. Overall, considering the failure rates and downtimes for repair, as well as the necessary for a removal from a nacelle and replacement, the understanding of failure in gearboxes, blades and generators is important for further design, manufacture and maintenance.

The main limitation of this method is that it relies on failure statistics. The data used and models developed may be out-of-date, and inapplicable to new wind power systems which involve newly-developed materials and structures. In addition, data is always difficult to gather since it is sometimes considered confidential by wind turbine manufacturers and operators.

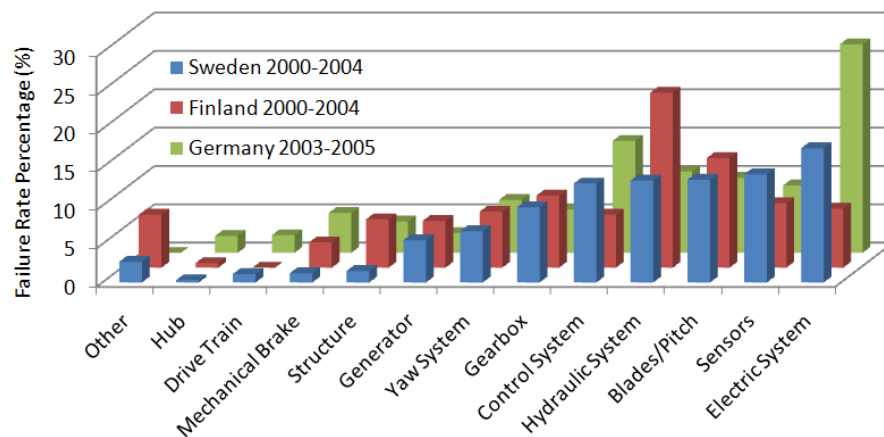


Figure 2.3 Data from a survey of failure in wind power systems [13]

Failure Rate and Downtime from 3 Large Surveys of European Onshore Wind Turbines over 13 years

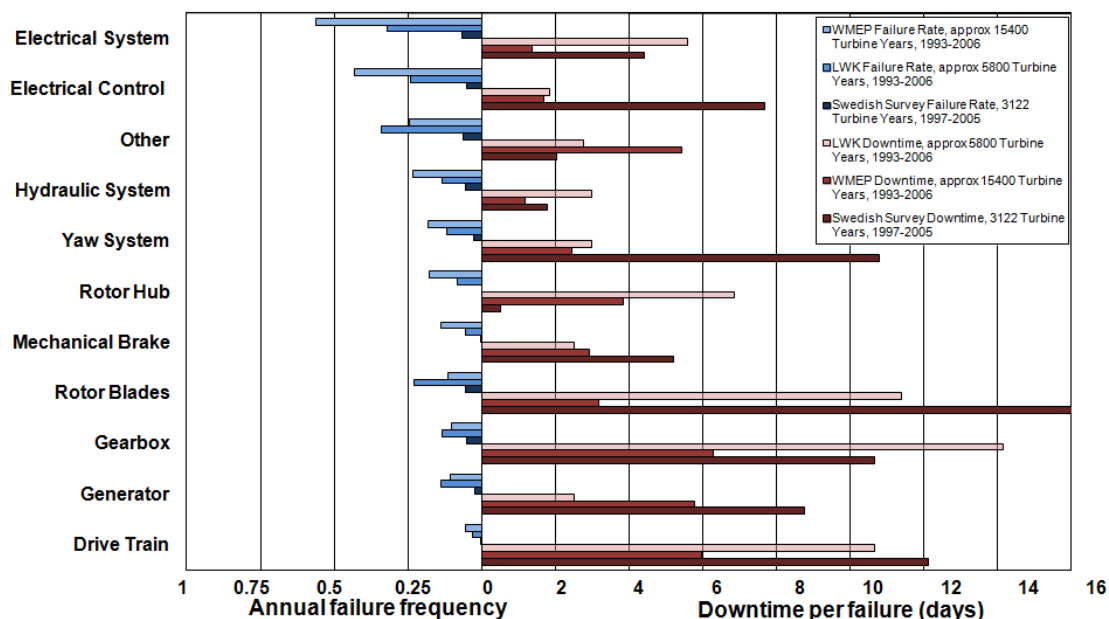


Figure 2.4 Statistics of failure rates and downtimes per failure comparison for critical subsystem of wind turbines [15]

(2) Analytical modelling in conjunction with reliability theory can be conducted. Some reliability theories such as the Bathtub curve [4], [15] *etc.* are good tools to use in modelling the lifetimes and predicting the failure in failure models. The Bathtub curve, as shown in Figure 2.5, is a probability-based model for understanding the reliability of any component or system. It depicts the relative failure rate of products over time, showing with three zones: an infant mortality period with a decreasing failure rate, followed by a normal life period (also known as "useful life") with a low, relatively constant failure rate, and concluding with a wear-out period that exhibits an increasing failure rate. Analytical mathematics methods, such as Markov–Monte Carlo simulation [17], are used for modelling operating conditions and other factors. In conjunction with NDE techniques, the Bathtub curve or Markov-Monte Carlo model can provide criteria for condition-based maintenance and prediction. Failures are detected and characterised using NDE techniques, and subsequently the health and reliability of components or systems can be estimated using these analytical models. The limitation of this method is that it requires large volumes of data over long time spans, and the theoretical analysis drawn from physics, mechanics, material and mathematics ignores environment issues and unexpected sudden events. In this thesis, it is concentrated to use NDE approaches

to obtain accurate and quantitative information about defects as input for those analytical models.

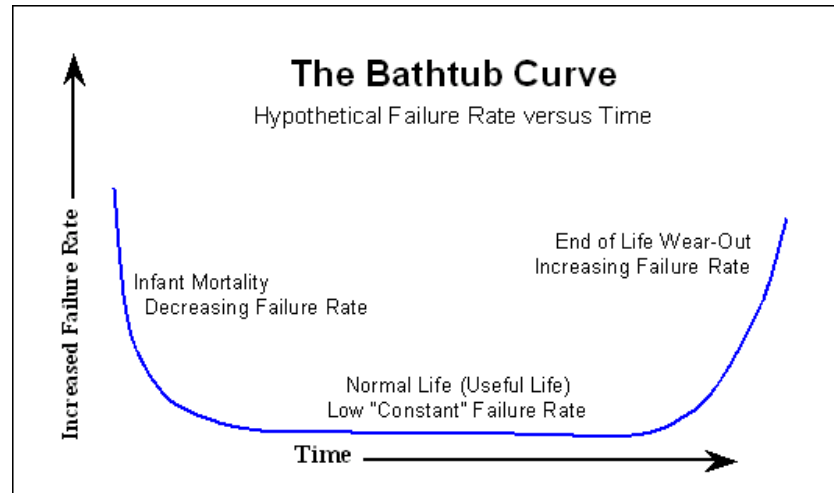


Figure 2.5 The Bathtub curve [15]

(3) Testing and monitoring, such as NDT&E and SHM of components and/or systems, can provide measurements for the characterisation of material and health monitoring. Particularly, types of failure in different components can be detected and identified during testing and monitoring, such as blade test for crack diagnosis [8], gearbox test for fatigue diagnosis [18].

NDT&E includes a wide group of analytical techniques used to test and evaluate the integrity of a material, component or system without causing damage [19]. “SHM is the continuous or regular monitoring of the condition of a structure or system using built-in or autonomous sensory systems, and any resultant intervention to preserve structural integrity” [20]. NDT&E is a well-established ‘manual’ testing and evaluation technique which focuses on the detection and characterisation of defects in materials. It has been extended to wind turbine blades, for example using Acoustic Emission (AE) to locate defects [21]-[24], ultrasonics and radiography to acquire and analyse images for defects [25], [26], and fibre optics for strain monitoring [27]. SHM can provide real-time data concerning the health and operational conditions of components or systems. Compared with NDT&E, SHM emphasises real-time and continuous monitoring of defects or

damage. Smart materials and sensors are used in lifecycle monitoring, such as piezoelectric material for self-diagnosis using a modified impedance model [28], continuous sensors built from piezoelectric transducer (PZT) material for AE monitoring [29], Fibre Bragg Grating (FBG) sensors for bridge monitoring [30] *etc.*

Based on the analysis of failure, reviews of NDT&E and SHM for wind turbine blades are provided in Section 2.2.

Based on the study of failure models for wind turbines, the blade is identified as a critical component with the relatively longest downtime. Therefore, the composite blade is chosen as the target of evaluation in this thesis. In the next sub-section, failures in the composite wind turbine blade are addressed.

### ***2.1.3 Failure in composite wind turbine blades***

In Section 2.1.2, failure models for different components and subsystems of wind turbines have been reviewed along with approaches to build failure models. From the review, it is clear that wind turbine blades are associated with the longest downtimes, despite their relatively low failure rates. In addition, the blade is one of the most expensive components in a wind turbine system to repair. Thus, the monitoring and evaluation of wind turbine blades during manufacturing and operation is critically important in preventing further damages and organising appropriate repair schedules to keep the blades working and to extend their lifetime. In this sub-section, the failure which occurs in wind turbine blades are specifically reviewed so that the challenges involved for NDE and SHM can be identified.

Rather than heavy metallic material, more and more non-metallic composite materials are now used in turbine blades, such as carbon fibre reinforced plastics (CFRP) and glass fibre reinforced plastics (GFRP) [30]. The majority of wind turbine blades are made of glass fibre/epoxy, glass fibre/polyester, wood/epoxy or carbon fibre/epoxy composites [32]. The most significant advantage of composites is that they have high strength but are lighter in weight compared with metals. CFRP exhibits higher-strength behaviour than GFRP and has better capability to reduce weight. However, the cost of CFRP is higher. GFRP is the main material used for small wind turbine blades up to around 35 metres, but CFRP or a combination of CFRP and GFRP is the primary

material used for megawatt-scale wind turbine blades, whose length is usually over 60 metres [33], [34]. The structure of a typical wind turbine blade is shown in Figure 2.6, and includes the main spar, downwind side, upwind side, leading edge, trailing edge, and aerodynamic shell.

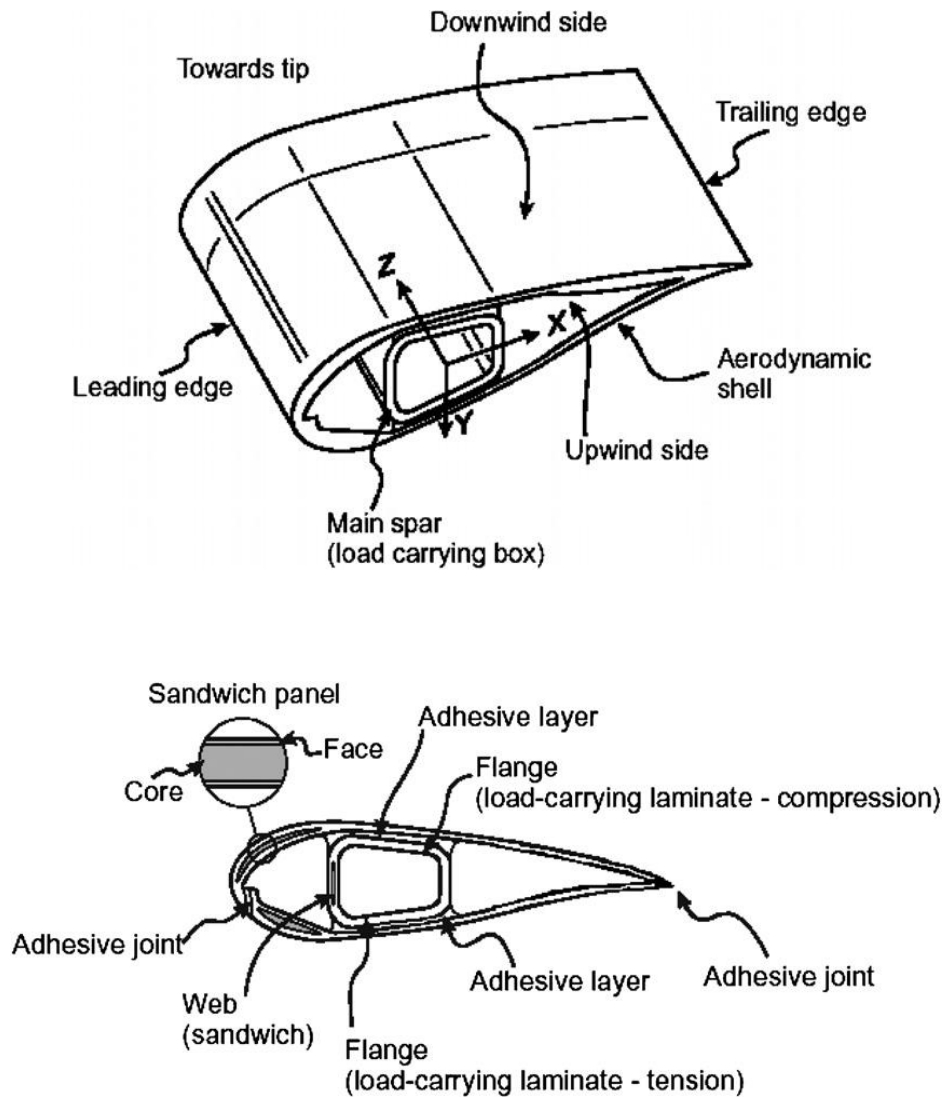


Figure 2.6 The main elements of a wind turbine blade [8]



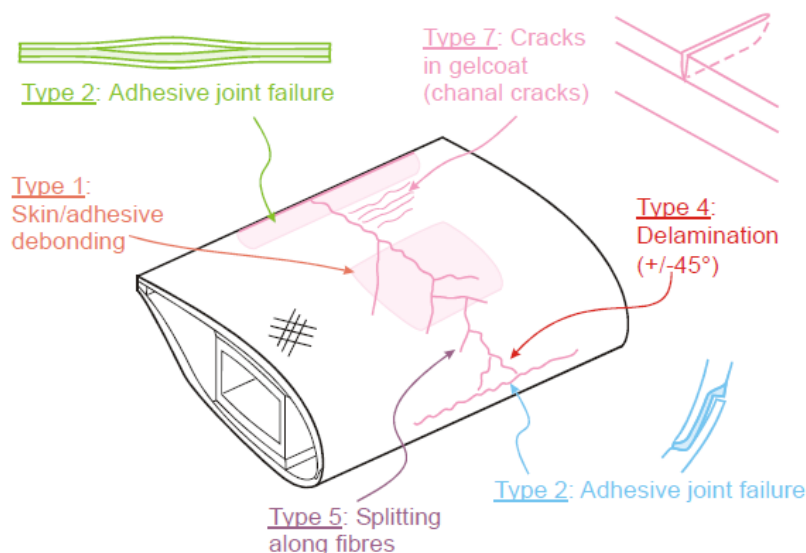


Figure 2.7 A sketch illustrating some of the common types of damage found in a wind turbine blade [8]

Damage to a blade can occur in several ways. Typical damage types in wind turbine blades are summarised in Table 2-I [8], [27], [35]-[37], and a sketch of types of damage is shown in Figure 2.7. Comparing the damages in Table 2-I, many damages have similar behaviour with cracks, delamination and impact damages in terms of discontinuities in the material's property. For example, skin/adhesive debonding and adhesive joint failure are caused by a separation of two layers, which is similar to delamination. These types of damage lead to the discontinuities in the material's property in the depth direction ( $z$  direction). Splitting along fibres or cracks result in discontinuity in the layer planar ( $x$  and  $y$  directions). Impact damage changes the material property in all  $x$ ,  $y$ ,  $z$  directions with a certain percentage of variation. Therefore, crack, delamination and impact damage can be categorised as the three typical types of defects in composites.

To detect and quantify damage to composite blades, NDE and SHM are both powerful tools. In the next section, the state-of-the-art of NDE and SHM techniques for composites are reviewed. The advantages and disadvantages of each method are summarised, followed with challenge identification for evaluation and monitoring of composites.

Table 2-I Typical damage to wind turbine blades [8], [27], [35]-[37]

Type	Description
1	Damage formation and growth in the adhesive layer joining skin and main spar flanges (skin/adhesive debonding and/or main spar/adhesive layer debonding)
2	Damage formation and growth in the adhesive layer joining the up- and downwind skins along leading and/or trailing edges (adhesive joint failure between skins)
3	Damage formation and growth at the interface between face and core in sandwich panels in skins and main spar web (sandwich panel face/core debonding)
4	Internal damage formation and growth in laminates in skin and/or main spar flanges, under a tensile or compression load (delamination driven by a tensional or a buckling load)
5	Splitting and fracture of separate fibres in laminates of the skin and main spar (fibre failure in tension; laminate failure in compression)
6	Buckling of the skin due to damage formation and growth in the bond between skin and main spar under compressive load (skin/adhesive debonding induced by buckling, a specific type 1 case)
7	Formation and growth of cracks in the gel-coat; debonding of the gel-coat from the skin (gel-coat cracking and gel-coat/skin debonding)
8	Low-energy, low-velocity impact damage, also producing extensive sub-surface delaminations, matrix cracks and fibre fractures

## 2.2 State-of-the-art of NDE and SHM methods relevant to composites

The purposes of NDE and SHM of composites include the prediction of damage and lifetimes [38], the investigation and evaluation of environmental impacts [39] and the health status of a given product or system during its lifecycle. However, in contrast to other traditional NDE and SHM applications, the materials used and structural configurations of wind turbine blades make the process more complex since new materials with multiple-layered and complex structures are used in these blades, in particular in large-scaled offshore turbine blades.

To improve the reliability of wind power systems and to understand their failure models, much research and development on inspection and monitoring systems for wind turbine blades has taken place. These include the fatigue test for wind turbine blades [39] at the National Renewable Energy Laboratory (NREL). This fatigue test integrated multiple sensor systems developed by following institutes the Sandia National Laboratory (SNL), and NASA Kennedy Space Centre, the Purdue SHM system, and the Virginia Tech SHM system. Beattie from SNL applied acoustic emission (AE) systems for fatigue tests and the NASA Kennedy Space Centre SHM system applied macro-fibre composite sensors for wave propagation based inspection. Meanwhile, the Purdue SHM system used tri-axial accelerometers to measure tip deflection, and the Virginia Tech SHM system used macro-fibre composite sensors for impedance measurements. Moreover, strain gauges and photoelastic panels are used for load/strain measurements, and two thermography cameras for monitoring the thermal gradients of photoelastic panels were implemented by NREL. Much work still remains to be done to determine which SHM technique is best suited for a particular wind turbine application as there are inherent challenges in the SHM of large structures to detect damage that often occurs first at a small scale, and it is difficult to distribute arrays of sensors widely enough to monitor the entire structure. In general, challenges remain in the optimal selection of sensors and decision making for global and local monitoring of structures and defects in a reliable, cost-effective manner and effective use of information .

Apart of above developed SHM systems, individual methods used for composite materials are reviewed in the following sub-sections. These can be divided into acoustic, optical, EM and thermographic methods, as shown in Figure 2.8.

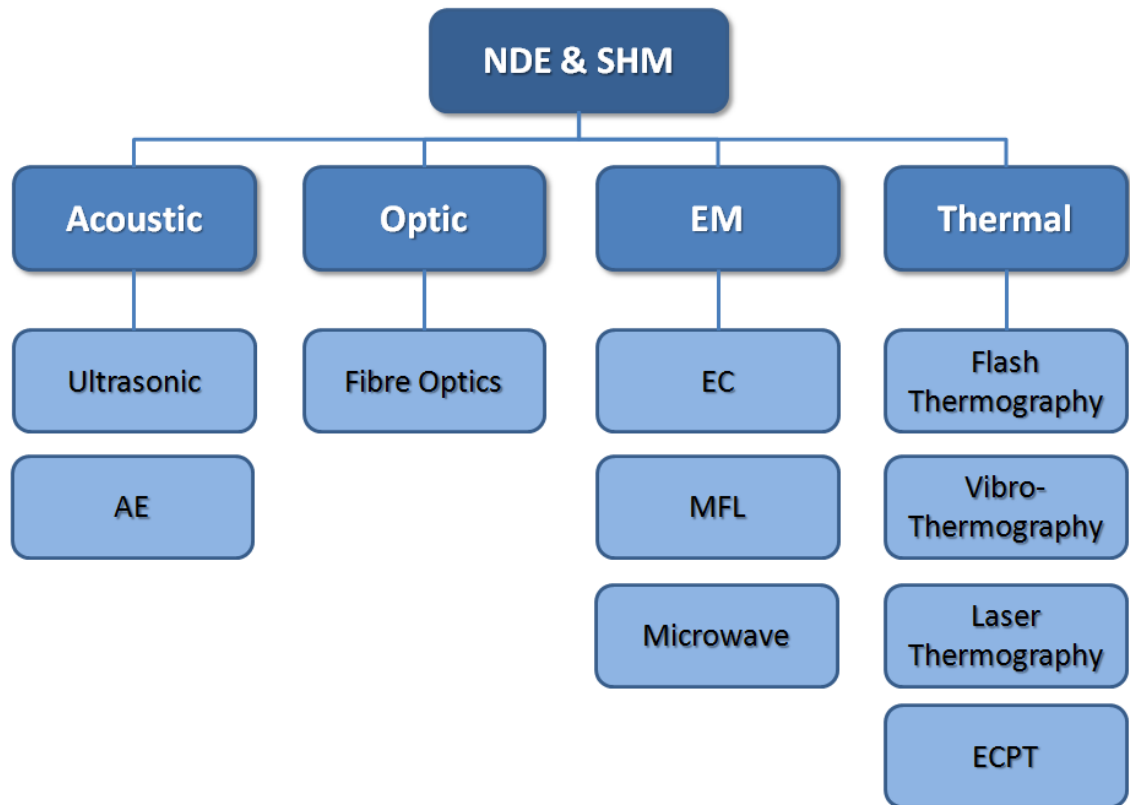


Figure 2.8 Category of NDE techniques reviewed in this thesis.

### 2.2.1 Acoustic methods

#### 2.2.1.1 Ultrasonics

Ultrasonics is a well-established method used to evaluate the inner structure and defects in solid objects. Ultrasonic scanning and phased arrays are useful in inspecting large-scale structures such as wind turbine blades. The main principle of this technique is that an ultrasonic wave passes through the material and is then reflected by a discontinuity of acoustic impedance, such as a defect. A transmitter introduces the ultrasound wave into the material to be inspected through a couplant, which is usually water or oil but may also be air, and the signal propagates through the material and is picked up by a receiver on the opposite surface of the material. Alternatively, the wave may also be applied with a single transducer in a pulse-echo mode or with a pair of transmitter and receiver on the same side of the material to be inspected, as shown in Figure 2.9 [41]. Due to the multiple-layered structure of composites, multiple reflections between layers may reduce the signal-to-noise ratio (SNR) of the received signal because of the

cancelling of received signal from multiple reflections, which is a major problem in the use of ultrasonic method for composite material.

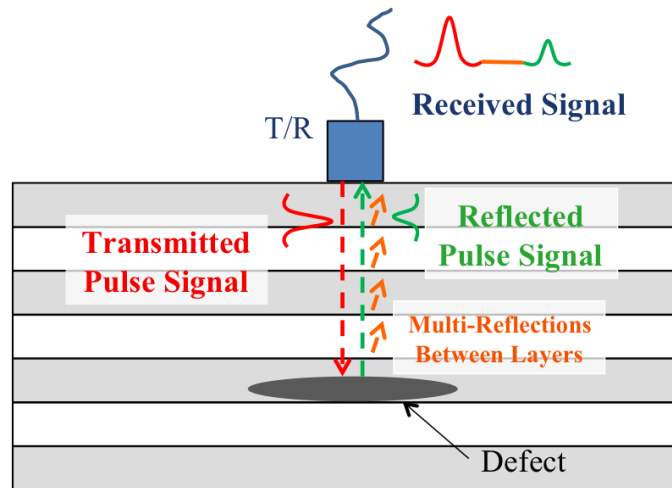


Figure 2.9 Schematic diagram of pulse-echo ultrasonic technique

Ultrasonics is typically applied for defects oriented perpendicularly to the propagation direction of ultrasound wave [42]-[45]. The reflected time, amplitude of the ultrasound are normally monitored as features for localisation and quantification of defects.

Jasiūnienė *et al.* [25], [26] tested a GFRP wind turbine blade using a pulse-echo immersion technique with two types of ultrasonic transducers at focused 2.2 MHz and planar 400 kHz frequencies, respectively. Three man-made internal defects with diameters of 81 mm, 49 mm and 19 mm were detected and imaged. The results showed that the use of a low frequency planar transducer allowed the detection of deeper defects due to less attenuation through the multiple-layered structure.

Rusborg *et al.* [41] conducted the field inspection of GFRP laminates using a pulse-echo method in the frequency range from 0.5 up to 5 MHz. Automated ultrasonic scanning equipment (PS-4 system) developed by FORCE Technology was used to inspect a wind turbine blade made of GFRP. The results showed that the delaminations and cracks with diameters of down to 10 mm could be detected. In addition, multiple cracks were detected with increasing attenuation of the sound wave. Impact damage on GFRP skins leaving a dent on the surface was also found.

Satito *et al.* [45] used ultrasonic C-scan images and cross-sectional photographs to reconstruct impact damages within CFRP laminates. A 3D impact damage model for multi-axial laminate was developed. Through fatigue test, impact damage and the resulting delamination and transverse cracks near the impact point were found and reconstructed.

All of the above studies required the scanning of the sample with a relatively long inspection time. To speed up inspection, long-range ultrasonics has been proposed. Guo and Cawley [46] introduced the  $S_0$  Lamb mode for propagation over distances of the order of one metre in composite laminates. Through the investigation of the interaction of the  $S_0$  lamb mode with delaminations, they found that the amplitude of the reflected  $S_0$  lamb mode from a delamination strongly depends on its depth in the thickness of the sample. In addition, the location of delamination determined the maximum and minimum values of reflectivity, which corresponded to the locations of maximum and minimum shear stress across the interface.

The approaches discussed above require a couplant, normally water, for the ultrasonic probe to introduce ultrasound into the sample, which is more feasible in laboratory studies than in field tests. To overcome this problem, air-coupled ultrasonics [47] and laser ultrasonics [48], [49] have been proposed. The use of air-coupled ultrasonic transducers allows non-contact rather than contact testing, which is more suitable for most inspection conditions. However, an appropriate angle for the introduction of ultrasound into samples to be inspected is strictly required. Another non-contact method uses laser ultrasonics. Here the transducer pair is composed of a laser ultrasonic generator and an interferometric sensor. Using air-coupled or laser ultrasonic transducers, the SNR is significantly reduced, and this remains a challenge for defect detection and quantification.

### 2.2.1.2 Acoustic emission

Acoustic emission methods can give knowledge of defect generation, localisation and the monitoring of its propagation. AE is defined as the transient elastic wave generated when strain energy is released suddenly within or on the surface of a material [50]. AE waves occur because of microstructural changes, such as the extension of a fatigue

crack, fibre breakage in composite materials, dislocations, friction phenomena within cracks, or plastic deformation. These changes lead to elastic waves being generated within a broad frequency range between 20 kHz and 1 MHz. When AE or stress waves reach the material's surface, small displacements produced by them are detected by PZTs and then the stress information is converted into electrical signals.

A typical AE signal produced when a crack occurs is shown in Figure 2.10. Some parameters of AE signals represent the state of the damage, as shown in Table 2-II.

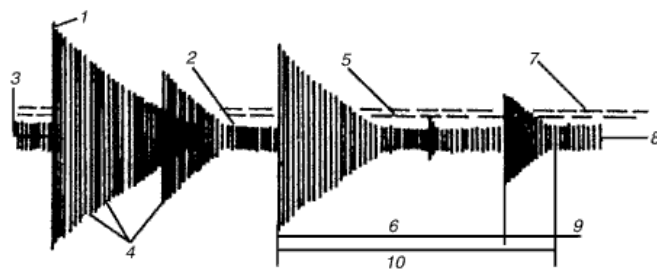


Figure 2.10 Schematic representation of AE signal [51]: 1. Maximal amplitude of pulse, 2. Noise level, 3. Voltage, 4. Single oscillations, 5. Standard deviation of amplitude, 6. Interval between pulses, 7. Discrimination level, 8. Time, 9. Pulse duration, 10. Events.

Table 2-II Parameters of AE and their informative content [51]

Parameters of AE	Informative content
Amplitude	Energy of AE source
Amplitude distribution	Type of present defects; failure mode (ductile failure or brittle fracture)
Frequency spectrum	Nature of AE source
Count rate*	Rate of defect growth
Time distribution of pulses	Type of growing defects

\*Count rate is the number of threshold crossings of AE signals above a pre-set value per unit time

In one study, seven types of crack damage were categorised during a 25-metre test on the type V52 blade manufactured by Vestas Wind Systems A/S, by means of the analysis of data from videos and photos, strain gauges, AE and deflection sensors [8]. The damage types were cracking along adhesive layers, sandwich face/core debonding, composite cracking along fibres, the compression failure of the laminate, and cracks in the gel coat.

Rumsey *et al.* [23] reported on the use of a PAC DiSP system in the AE testing of a 9-metre long, 160.5 kg blade, the TX-100. Another test based on audible cracking sounds from blades was conducted by Joosse *et al.* [21]. A 9-metre carbon fibre wind turbine blade, the CX-100, was tested in [6] with load, deflection, strain, and acoustic emissions monitored. It was also shown that the AE monitoring system detected not only the locations of damage but also incipient global blade failure. Certification tests for both small and large-scale wind turbine blades were developed and demonstrated in [5], [52], [53] using AEGIS and Aegis PR software, which could provide the basis for an online blade condition monitoring system.

Beattie [22] showed that the fatigue condition of large fibre reinforced plastic wind turbine blades could be estimated using AE method. PZT ribbon sensors were made and implemented in [29]. The lead break, which is similar to a fibre failure in the fibreglass plate, was conducted in the test.

To achieve higher accuracy in damage evaluation, the number of sensors must be increased. Schulz *et al.* [54] proposed a structural neural system for the SHM of wind turbine blades. A 10 x 10 array sensor system with four channel outputs was introduced in [29], [54]. Ghoshal *et al.* [55] also suggested using multiple PZTs connected together in a series or array to reduce the output channel number.

The limitations of AE methods include that it is a contact method, requiring sensors to be bonded to the structures to be inspected. The sensors may be damaged during operation. Also AE methods can detect the generation and propagation of defects in online and in-situ monitoring, but it is difficult to obtain quantitative information about the defects. Finally, false alarms may be frequent and inevitable with these methods.



### 2.2.2 Fibre Optics

Fibre optics (FO) has been widely used in communications applications, but can also be implemented as sensors in NDE or SHM. Light is kept in the core of the fibre optics by total internal reflection. The fibre optic material acts as a waveguide, and is made from high-purity, low-loss optical materials, usually silica. The propagation of light through a FO is shown in Figure 2.11. The FO can be attached to a test sample to measure loads. The principle of plastic FO is that the optical power of a light source which goes through the optical fibre will reduce linearly as the strain of the optical fibre increases, but will decrease dramatically when the crack density in the specimen increases. Therefore, FO can be used to detect cracks.

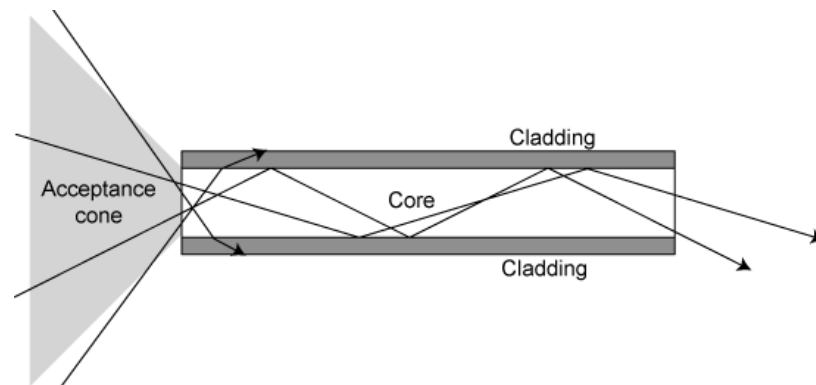


Figure 2.11 The propagation of light through a fibre optic [56].

FO sensors have been widely used in the SHM of bridges and aircraft to detect and monitor fatigue cracks, disbanded joints, erosion, impact and corrosion in both metallic and composite materials [57]-[59]. The advantages of FO for composite blades are that it is sensitive to strain/stress and adaptable for large-scale structures.

Roach *et al.* [59] embedded chirped fibre Bragg grating (FBG) sensors to detect crack growth in metal structures and disbands in composite-to-metal bonded joints. Four gratings were implanted onto a multi-ply boron epoxy doubler, where gratings A and C were fixed parallel to the short axis of the doubler whilst B and D were parallel to the long axis. From the strain distribution from sensors B and D, fatigue crack growth between  $950 \mu\epsilon$  and  $1020 \mu\epsilon$  was monitored during fatigue tests with a maximum

tension load of 34,000 lbs. With the shear strain distribution from sensors A and C along the edge of the test specimens, the taper region for disbands were also monitored.

Grouve *et al.* [60] discussed the influence of delamination on the resonance frequencies of composite material. Six unidirectional carbon-polyetherimide beam specimens were tested using Draw Tower fibre Bragg gratings. The result showed that the resonance frequency shift is very sensitive to delamination parameters, which include location, size, and laminate lay-up.

Schroder *et al.* [61] installed an FBG sensor system for load monitoring in a 53-metre long GFRP wind turbine blade. In order to reduce the impact of temperature, an additional FBG temperature sensor was installed. The test with 50 load cycles per second and strain amplitudes of up to 2000  $\mu\epsilon$  was conducted for 4 weeks to simulate the lifetime of 20 years at a rotation rate of 12 rpm. The accumulated strain data could be used for the determination of fatigue load footprint and lifetime estimations for rotor blades.

Takeda [62] found that theoretical predictions agreed with experimental results for transverse crack density-strain and stress-strain curves. Besides this, plastic optical fibres (POFs) have been used in tensile tests of GFRP material because their thermal expansion coefficient is almost the same as that of the GFRP matrix, and FBG sensors were used to detect the transverse cracks in CFRP composites. The relationships among optical power, crack density and strain from POF and the power spectrum reflected from the FBG sensors were discussed. By observing the loss in optical power and changes in the reflected power spectrum, transverse cracks could be detected both in GFRP and CFRP composites.

Work on the detection of damage in the adhesive layers of wind turbine blades using fibre optic displacement transducers was presented in [27]. Microbend strain transducers were used to measure compression. From the simulation and experiments, it was shown that microbend FO sensors were suitable for the detection of damage in the adhesive layers between larger composite structures. The sensitivity of transducers reached 1.3%  $\mu\text{m}$  whilst 1.6%  $\mu\text{m}$  was expected and a large 50% change in transmittance was obtained for displacements of 40  $\mu\text{m}$ . In addition, the sensitivity was sufficient for the detection of cracks in the adhesive layers with typical sizes of 100-200  $\mu\text{m}$ . However, the signal was strongly influenced by other factors such as temperature.

In addition, the FO sensors are vulnerable, which means the sensors may be damaged before the samples or structures to be monitored.

### 2.2.3 Electromagnetic methods

#### 2.2.3.1 Eddy current

Eddy current techniques originated from Michael Faraday's discovery of electromagnetic induction in 1831. The principle of eddy current can be stated as follows: the electric current  $I$  within a coil generates a primary magnetic field  $H$  surrounding the coil. According to Faraday's law of induction, so-called eddy currents are induced by the primary magnetic field  $H$ . According to Lenz's law, the eddy current then creates a secondary magnetic field  $B$ , which is opposite to the primary magnetic field  $H$ . Eddy currents are induced by the primary magnetic field and Figure 2.12 shows the principle involved. The eddy current response can be affected by the material's conductivity, permeability, frequency, geometry, *etc.* In addition, eddy current distribution is strongly influenced by the non-homogeneity of composite materials, which requires the optimisation of the coil with respect to fibre orientation in order to achieve high SNR.

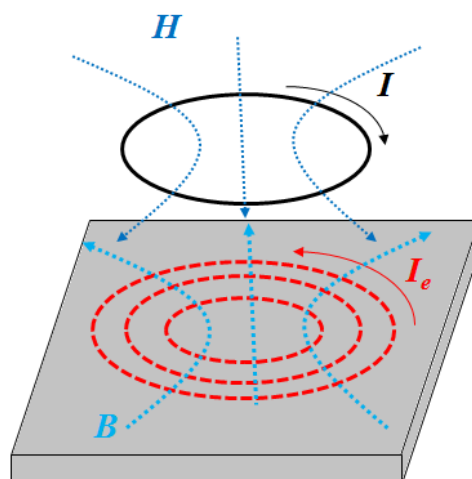


Figure 2.12 The principle of eddy currents

EC techniques have become powerful methods in the for inspection of conductive specimens, and many methods have been proposed based on EC in order to improve inspection efficiency, detection capability, evaluation feasibility and compatibility [63], [64]. Multi-frequency eddy current (MFEC) [65] and pulsed eddy current (PEC) [66]-[68] are considered to be advanced EC techniques in the development of EC and its application to EM NDE. Both MFEC and PEC are specific EC techniques which employs a wide range of frequencies in excitation. MFEC adopts multi-frequency sinusoidal excitation ranging in scale from several hertz to megahertz. Excitation is generated in sequence or simultaneously and lasts for a predefined time. In contrast, transient excitation in the form of a pulsed/step waveform is implemented in PEC, where the frequency band is wider than in sinusoidal excitation at a single frequency.

Gros [69] used the EC technique for the detection of delamination caused by low-energy (0.5-7.0J) impacts in CFRP materials. The results demonstrated that EC provided accurate, efficient and rapid qualitative information on low-energy impacts in these materials because it penetrated the air gaps caused by delamination. He *et al.* [70] proposed automated defect classification using PEC in multi-ply structures with interlayer gaps where lift-offs varied from 0 to 1.4 mm. PCA and a support vector machine were also investigated for automated classification.

Mook *et al.* [71] discussed fibre orientation measurements in CFRP materials using rotary probes. Additionally, local imperfections such as fibre fraction fluctuations based on changes in fibre orientation could be displayed. Furthermore, the EC method could be used to detect fibre debonding from the ageing effects and impact damage, which results in fibre breaking, matrix cracks and delamination.

Yin *et al.* [72] implemented three multi-frequency EC sensors to measure bulk conductivity, characterise the directionality and image the defects in CFRP specimens. The results showed that the EC method could effectively locate damaged areas and performed more accurately than an ultrasonic scan method.

The detection of low velocity impact damage in CFRP using high temperature superconductor (HTS)-SQUID was proposed in [73], [74]. Low velocity impacts are the most frequent causes of delaminations, and using HTS-SQUID magnetometers in an EC experiment, defects in CFRP samples of diameters lower than 1 mm were detected [73]. The main advantage of the SQUID system is its excellent sensitivity down to very low

frequencies. The results for samples with heat and impact damage have also been published [74].

From the literature, it is clear that the eddy current method is sensitive to surface and sub-surface defects, but deeper defects are more difficult to detect due to skin effects. Besides this, the excitation direction used is crucial for composite materials owing to their non-homogeneity. For large-scale structures, scanning is required but this is time-consuming and limited in terms of spatial resolution.

### 2.2.3.2 Magnetic flux leakage

Magnetic flux leakage (MFL) is a magnetisation-based NDE technique used to detect and characterise corrossions, cracks and other damage using a magnet which introduces a magnetic field into inspected specimens [75], [76]. Figure 2.13 demonstrates the principle of MFL. When the probe encounters a defect, such as a crack or corrosion, the magnetic field leaks out of the specimen from the defect, and that leakage field is detected by a magnetic sensor, which may be either a Hall-effect sensor or a pick-up coil. This method is appropriate for the detection and characterisation of defects in ferromagnetic-material.

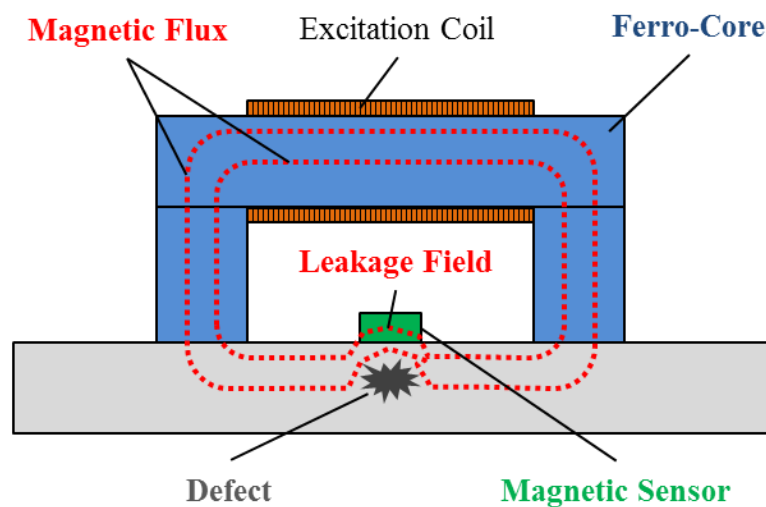


Figure 2.13 The principle of MFL

The MFL technique is popular for the inspection of pipelines [75]-[78] or rail-tracks [79], [80]. To speed up inspection, a dynamic MFL inspection system was firstly developed by Michigan State University College [81], which is applicable to measurement at speeds less than 10 m/s. Li et al [82] have also simulated and examined the MFL response against defect depths up to 30 m/s. However, because they are not ferromagnetic materials, MFL is not suitable for defect evaluation in CFRP or GFRP.

### 2.2.3.3 Microwave NDE

The microwave frequency spectrum ranges from 300 MHz to 300 GHz. An overview of microwave and millimetre wave NDT&E methods [83], [84] discussed many applications, including dielectric material characterisation [85], [86], the detection and sizing of defects, corrosion under paint and microwave imaging for flaw detection. Far field [87], [88] and near field [89]-[92] microwave and millimetre wave NDT&E approaches detect defects through the magnitude and phase variation of the reflection coefficient. Microwave and millimetre wave imaging using rectangular open-ended waveguides or custom-designed transceivers have been reported [93], [94]. Based on the changes in material properties caused by a defect, many published studies using rectangular waveguides have focused on crack detection [95], electromagnetic modelling of the interaction of the EM field with a crack [96], [97] and crack imaging [94].

From the applications, it can be found that microwave is a non-contact method, which does not require any couplant. The high frequency allows relatively high spatial resolution in inspections. In addition, microwave NDE is relatively inexpensive. However, scanning on a large-scale sample is normally time-consuming, and in microwave imaging approaches, the algorithms used for reconstruction from the scattering of microwave signals are relatively complex. To deal with large-scale inspection, Ghasr *et al.* [98] designed a microwave camera system which provided a means for fast inspection and visualisation with high sensitivity and resolution for dielectric materials. However, microwaves cannot efficiently penetrate through conductive materials, which means that surface defects can be sensed but it is difficult to detect deeper defects.

### 2.2.4 Thermographic methods

The major advantage of thermography over other techniques is the potential it offers for the rapid inspection of a large area within a short time, even though so far it has mostly been applied to samples in the laboratory instead of in-situ structures [99]. However, there is likely to be a trade-off between detectable defect size and inspection area. Thermography is also applicable to a wide range of materials, including glass fibre, carbon fibre composites and metallic materials, where specific excitation techniques are suitable for different applications. To inspect defects over a large area and at large stand-off distances, the integration of thermography and other NDE approaches has been investigated, resulting in, for example, the development of flash thermography, sonic thermography, laser thermography, and eddy current pulsed thermography. Those thermographic methods are reviewed below.

#### 2.2.4.1 Flash thermography

Flash thermography uses flash lamps, air guns, or other means to heat the samples to be inspected, resulting in transient thermal interactions at the surfaces which are monitored by an infrared camera. As a high-speed, portable and non-contact inspection technique, it can be used for the detection of a variety of defects in a large range of materials [99]-[103].

Avdelidis *et al.* [99], [100] implemented flash thermography to detect notches in aluminium aircraft skin, delamination between two composite plies, as well as holes and fibre breakout in carbon composites. By quantitatively analysing the contrast among the detected defects, relationships between the diameter of defects and transient time were derived.

Quantitative information about defects can be gained from analysis of heat transfer. Liu *et al.* [101] developed a 3D thermal model based on a finite-difference splitting method in the time domain. Through phase angle contrast measurements, defects with varying diameter and depth were detected and quantified in a SiC coated C/C composite

specimen. The results showed that the diameter of the smallest detectable defect was about 2 mm.

With the use of appropriate algorithms, results gained from flash thermography can be significantly improved. Ibarra-Castanedo *et al.* [102] compared four methods in improving the SNR of flash thermography using differentiated absolute contrast and thermographic signal reconstruction. Through the experimental studies of delaminations in composite material, thermographic signal reconstruction showed the best SNR.

Results can be further improved via a combination of heat scheme. Mulaveesala *et al.* [103] used pulse thermography and modulated lock-in thermography simultaneously to combine their advantages. A specimen was heated in a specific range of frequencies, rather than at a single frequency. The results were validated on a CFRP sample.

#### 2.2.4.2 Thermosonics or Sonic IR

Thermosonics, which is also called Sonic IR or vibro-thermography, uses a powerful ultrasonic source at frequencies of tens of kilohertz with a power from several hundred to several thousand watts producing frictions at defects in order to generate heat, and then an IR camera is used to obtain a temperature profile at the surface of the inspected specimen.

Morbidini *et al.* [104] implemented thermosonics for crack detection in metallic specimens in conjunction with the measurement of local vibration strain. The results showed positive correlations between predicted values and the measurements from small cracks generated in a high-cycle fatigue regime. Han *et al.* [105] reported results using several coupling materials and quantified the effect on the detect ability of a defect. Correlations between levels of ultrasound energy and the resulting thermal energy at cracks in an aluminium sample were discussed.

Thermosonics is also capable of the detection of defects in composites. Han *et al.* [106] discussed the application of thermosonics for detecting disbonds and delaminations in composites through simulation and experiment. Chaotic sound was proposed to provide a uniform background for the imaging of defects. Zhao *et al.* [107] derived depth profiles of delaminations from the time delays of temperature increases at the surface.



The temperature against time and the second derivative of T-t were evaluated to gain the depth information about defects.

#### 2.2.4.3 Laser thermography

In laser thermography, a laser with a power of several watts is used to heat the sample locally, and the resulting surface temperature is recorded by an IR camera. This method can also be used to detect defects in metal or composites. Avdelidis *et al.* [108] proposed 3D laser profilometry and pulsed thermography to obtain surface roughness information. Rashed *et al.* [109] used laser spot imaging thermography to detect and localise fatigue cracks in steel bar, and their results were validated with a 2D numerical model. Schlichting *et al.* [110] quantified the crack angle and depth by analysing the asymmetries caused by cracks in laser thermal footprints. The results were validated through calibrated experiments and FEM simulation.

Kuhn *et al.* [111] compared the ability of thermosonics and laser thermography to detect delamination in composites. It was found that the detection region of laser thermography is larger than that of thermosonics. For samples with large dimensions, laser thermography only requires one measurement, whilst thermosonics needs more. From the point of view of accuracy, thermosonics is better because the heat is more focused at the defect.

#### 2.2.4.4 Eddy current pulsed thermography

Eddy current pulsed thermography combines EC and thermography, and involves the application for a short period of a high current electromagnetic pulse to the conductive material under inspection. Eddy currents are induced in the material, leading it to become heated. The existence of any defects distorts the propagation of the eddy current, leading to a variation in material temperature that can be detected with thermography. The non-homogeneity and anisotropic nature of CFRP in the subsequent cooling phase also affects the diffusion of heat. Therefore, the mixed phenomena of induction heating, which dominates in the heating phase, and the diffusion of this in the cooling phase along with the specific behaviour exhibited, give information useful for the quantitative

non-destructive evaluation of non-homogeneities in a given material. As opposed to flash and laser thermography techniques, ECPT focuses the heat generation at the defects, not only at the surface but also under it. In addition, ECPT is a non-contact method and requires no couplant.

ECPT has been used to inspect metallic parts [112]-[115]. Abidin *et al.* [112] evaluated the angular slots in metal through simulation and experiment. Features such as maximum temperature amplitude and slope inclination, were extracted to quantify the angle of the slot. Oswald-Tranta *et al.* [114] investigated the temperature distribution around a crack with different penetration depths using FEM modelling compared with experimental measurements on metallic materials. The results showed that lower temperatures were exhibited at the surface edge of a crack with higher temperatures found at the bottom of the crack in nonmagnetic materials with a large penetration depth.

Compared to defects in metal, those in composite materials have rarely been investigated. Ramdane *et al.* [116] detected inserted delaminations using induction-heating thermography. Experimental studies were undertaken in transmission mode, with the inductor and infrared camera on the different sides of the sample, which is normally not suitable for in-situ inspection. Moreover, the inspection period was around 80 seconds.

He *et al.* [117] combined transmission and reflection modes for the detection of wall thinning defects and interior defects based on heat diffusion. Through a 1D analytical model, a 3D numerical model and experimental results, a suitable detection mode for these defects was identified, and the location of the defects in terms of thickness was quantified.

In comparing thermographic methods, one difference concerns the way heat is introduced into the inspected sample. Flash and laser thermography mainly introduce heat at the surface, whereas thermosonics and ECPT generate heat not only at the surface but also underneath. Furthermore, thermosonics and ECPT focus the heat on the defect due to friction or eddy current distortion, which increase the temperature contrast between the defective region and defect-free areas. Flash, laser thermography and ECPT are non-contact methods, whilst a couplant is normally required for thermosonics. From point of view of inspection depth, flash thermography is adaptable by changing the lock-in frequency for defects at different depths. From adaptability in terms of fibre

orientation, ECPT can enhance specific excitation direction to optimise the directional evaluation along the fibre orientation or other directions in composite materials. From the point of view of materials to be inspected, ECPT can only be used for conductive composite such as CFRP, whilst other three methods can be applied for both conductive and non-conductive materials.

Through the comparison, ECPT, as a non-contact approach, concentrates heat generation at defects not only surface at but also beneath of inspected specimens. It allows large contrast between defective region and defect-free area in defect detection and characterisation. Therefore, ECPT is chosen as a hybrid and multiple-physical method for the evaluation of CFRP blades.

### **2.3 Overviews of interpretation and characterisation algorithms for ECPT**

Previous sections have identified the major types of defect as crack, delamination and impact damage. NDE and SHM methods to detect and characterise such defects have subsequently been reviewed. Through the literature survey, ECPT is proposed in this thesis because it offers directional excitations for non-homogeneous and anisotropic CFRP. In addition, the inspection using ECPT is rapid and non-contact. Furthermore, heat is concentrated at the defects, not only at surface but also beneath of the samples. In this section, algorithms to interpret and characterise the data gained from ECPT for defect detection and QNDE are presented.

In order to extract features from thermographic image sequence, several approaches were developed, including thermographic signal reconstruction (TSR) [118]-[121]. TSR was proposed by Shepard [118] in an attempt to increase spatial resolution and SNR, also to reduce the blurring of deep features by taking the first and second logarithmic derivatives approximation with respect to time on thermal image sequences. Balageas [119] implemented TSR in a homogenous plate with an accurate measurement of the distribution of thickness and diffusivity. Quek *et al.* [120] used TSR in aluminium, CFRP and GFRP composites, and mild steel samples. The results showed that an improvement of 60% in detection depth for CFRP composites was achieved for defects larger than 4 mm in diameter. Roche *et al.* [121] showed that the TSR technique is useful for the in-situ damage monitoring of woven composites by providing a

qualitative overview of the damages. Although TSR can enhance the detection ability of flash thermography, ECPT involves not only heat diffusion, but also interaction between eddy currents and defects whereas TSR presents transient thermal features at the level of individual pixels to form the enhanced thermal images. To achieve QNDE, characterisation algorithms at higher levels are required.

In the next sub-sections, the use of optical flow for flow pattern analysis at the local area level and PCA/ICA for thermal pattern investigation at the pattern level are reviewed. For surface defects, the transient temperature responses of pixels at hot-spots are easy to obtain and evaluate. However, the hot-spots may be blurred and the appropriate pixel is hard to select. Optical flow aims to track the heat flow at the defective area in order to detect and classify defects. However, when multiple defects occur in one sample or if the fibre texture is complex, the heat flow patterns may overlap. In those cases, it is hard to separate them using optical flow. Thus, PCA/ICA is used for the efficient separation of thermal patterns.

### ***2.3.1 Optical flow for the investigation of local areas***

Optical flow (OF) was first developed by Horn and Schunck [122] and then became widely used for estimating velocity fields and object tracking [123]-[128]. Horn *et al.* [122] proposed a method to find the OF pattern assuming that the apparent velocity of the brightness pattern is smooth almost everywhere in an image. An iterative computation was implemented to provide visual confirmation of the convergence of the solution in the form of needle diagrams, and this was then validated through experimentation.

In a review paper [129], Barron *et al* compared nine different OF techniques. The conclusion was drawn that the phased-based [130] and differential techniques [131] achieved the best results. After achieving the OF matrix, histograms and kernels were used to recognise human actions [132], which can be extended to quantify damage in CFRP samples. In addition, many attempts to use thermal image sequences or videos using OF to track the heat flow have been carried out [133]-[135]. Franco *et al.* [133] obtained estimations of the thermal flows of structures at fluid surfaces using a multi-resolution scheme based on Galerkin-Wavelet Analysis. Svantner *et al.* [134] presented

IR thermography heat flux measurements for fire safety applications, where the dependence of heat flux magnitude on distance and direction from a fire was evaluated. Haussecker [135] proposed a quantitative estimation in motion and extracted physical parameters of the heat transport of water at a target surface. The thermal flows in either fluid or fire were also determined by fluid motion, as shown in the results. Compared with the heat propagation at defects in CFRP using ECPT methods, the thermal pattern in either fluid dynamics or fire is easier to achieve and recognise.

### ***2.3.2 PCA and ICA for pattern investigation***

Principal component analysis (PCA) and independent component analysis (ICA) are used to enhance the contrast between defective regions and defect-free areas in the thermal image sequence.

Marinetti *et al.* [136] compared the efficiency of PCA to thermographic features extraction by considering the initial sequence as either a set of images or a set of temporal profiles. Khan *et al.* [137] identified water leakage in dikes from thermometric data using PCA and ICA. Rajic [138] employed PCA to improve the flaw detection ability of thermography, and characterised the surface flaw depth using characteristic times, estimated from the principle component (PC) vector. Yang *et al.* [139] implemented ICA for defect classification based on PEC signals. Statistical kurtosis was used as the basis for selecting independent components (ICs) for feature extraction, and in addition, the effects of lift-off on defects were classified. Bai *et al.* [140] proposed ICA to highlight the anomalous patterns of ECPT videos for cracks in metallic specimen. Estimated mixing vector using ICA around crack tips were used for the automatic identification of cracks in heating and cooling phases. From the literature survey, most studies try to enhance the contrast between defective and defect-free regions using PCA or ICA, but the ability to discriminate between multiple defects as well as the effects of fibre texture is limited, especially for non-homogeneous composite samples.

## 2.4 Chapter summary

An extensive literature survey has been reported of failure models for wind turbine systems, and composite blades in particular, including the consideration of failure rate, downtime and failure modes in critical components of wind turbine systems is reported, followed a discussion of by NDE techniques using acoustic, optical, electromagnetic and thermal methods for composite materials or blades. In addition, techniques used for defect interpretation and characterisation in eddy current pulsed thermography at different levels are reviewed, which include the use of optical flow for investigation at the local area level, and PCA and ICA for investigation at the pattern level.

From the literature survey, there are several problems of composite wind turbine blades and relevant NDE approaches to characterise the damages in composites needing to be addressed. These are as follows:

- Wind turbine blades are made of composites, mainly GRFP, CFRP or a combination of both. From historical statistical data, wind turbine blades are components with the relatively longest downtimes in spite of their low failure rates. This means that failures of wind turbine blades interrupt electric generation during repair or maintenance. Thus, early awareness of potential damage and its status with the help of NDE techniques for condition-based operation and maintenance is extremely important. The main failure modes in blades are cracks, delaminations and impact damage, which typically lead to the final collapse of the blades. Therefore, evaluation of the generation and propagation of these defects needs to be undertaken. Defect classification, visualisation and quantitative information about defects in non-homogeneous composites are required.
- The reviews of NDE techniques used for composites reveal advantages and disadvantages associated with each technique. Ultrasonics can be used to inspect a relatively large area, however a couplant is normally required which is not always suitable in some applications. Acoustic emission techniques can detect the generation and propagation of defects in online and in-situ monitoring, but it is difficult to obtain quantitative information about the defects. Fibre optics is good for monitoring large-scale blades, but the signal gained may be strongly influenced by other factors, such as strain and temperature *etc.* Eddy current or magnetic flux leakage methods are sensitive to surface and sub-surface defects,

but deeper defects are difficult to detect due to skin effects. Microwave methods provide a means of fast inspection and visualisation with high sensitivity and resolution for dielectric material, but microwaves cannot efficiently penetrate conductive materials. This means that surface defects can be sensed but it is difficult to detect deeper defects. The major advantage of thermography over other techniques is the potential it offers for the rapid inspection of a large area within a short period of time, even though it is mostly applied to samples in the laboratory rather than in-situ structures. Among thermographic techniques, eddy current pulsed thermography is a non-contact approach which concentrates heat generation at defects not only at surface but also under the surface of inspected specimens. It provides large contrast between defective regions and defect-free areas which is useful for defect detection and characterisation.

- Interpretation and characterisation algorithms used in ECPT techniques are mainly based on the features of transient temperature responses which are used for the quantification of defects at the pixel level. Few algorithms have been proposed which take account of the non-homogeneity of composite materials at the local area or pattern level. A comprehensive algorithm is required to deal with various types of defect in different fibre textures in order to allow defect detection, classification and characterisation. This includes defect identification and classification through feature extraction, separation of multiple defects in conjunction with distinguishing the fibre texture and defects.

To summarise the results of this literature survey, three challenges in defect detection and characterisation in CFRP are apparent: (1) the detection and classification of different types of defects at the surface or inside the sample; (2) problems arising from the non-homogeneity and multiple-layered structure of CFRP materials; (3) the QNDE of different type of defects and in different fibre textures.

To address these challenges, an ECPT system is proposed in this study for CFRP composites which provides a non-contact, rapid inspection of large-scale structures, as well as investigation algorithms at the pixel, local area and pattern levels in order to characterise surface defects (crack) and interior defects (delamination and impact damage) in different types of fibre textures. The next chapter introduces research methodology, including the theoretical considerations, numerical modelling and experimental system set-up of ECPT, along with the principles of the interpretation and

characterisation algorithms. In the subsequent chapters, different samples with different defects are used for case studies at the pixel, local area and pattern levels.



## Chapter 3. METHODOLOGY

Based on the challenges identified in the literature review, the methodology of eddy current pulsed thermography is outlined in this chapter. To address the challenges for composites, a research diagram for ECPT is proposed, as shown in Figure 3.1, which includes: an ECPT technique development with theoretical concerns, numerical modelling and the experimental studies, three levels of investigation of data gained from ECPT system in line with the knowledge from failure models, and the detection, classification and characterisation of defects.

By combining analytical and numerical methods for design and development of an ECPT-based experimental system, the transient thermal responses which correspond to the transient features of defects can be obtained. Analytical modelling provides an understanding of the physical phenomena. Numerical modelling helps in the design of the experimental system for non-homogeneous and anisotropic samples and in the validation of the experimental results. The experimental system is then implemented for real samples with defects. To build the ECPT technique, the three approaches are discussed and organised in the order below. The theoretical background of ECPT is introduced in Section 3.1, covering electromagnetic and thermal equations as well as their coupling. Section 3.2 represents the numerical simulation models for ECPT based on theory described in Section 3.1. Experimental system development and sample preparation are reported in Section 3.3.

Based on the ECPT systems and failure models summarised in Chapter 2, the transient thermal responses are investigated. Through numerical simulations and experimental studies, the relationship between extracted features and defects in forward and inverse problems can be established at different levels, according to defect location and fibre textures. As the increase of complexity of fibre texture or defect, the pixel, local area and pattern level are selected alternatively. The relevant processing algorithms based on

transient thermal responses are exhibited in Section 3.4, including optical flow and PCA/ICA. This three-level investigation achieves defect detection, classification and characterisation along with the case studies. Their own strengths and limitations for different defect locations and fibre textures are further discussed in Chapters 4, 5, and 6.

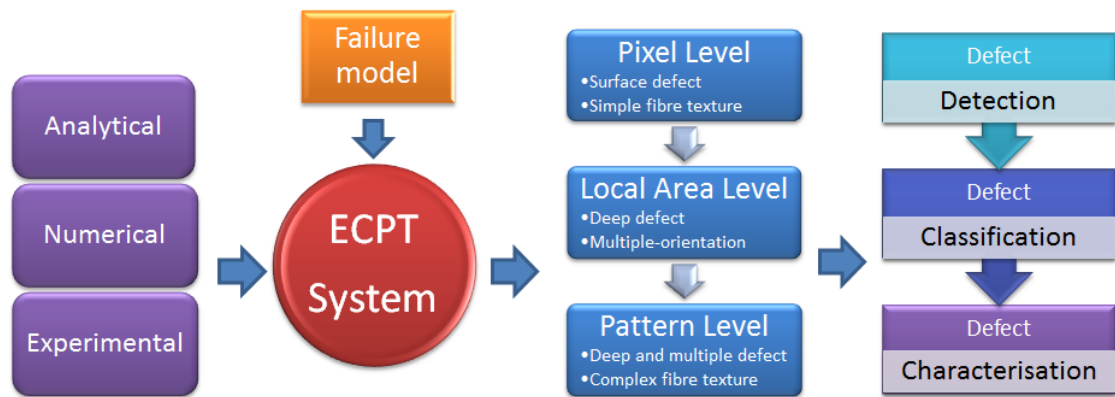


Figure 3.1 Research diagram for ECPT

### 3.1 Theoretical background of ECPT

ECPT is a non-contact approach which concentrates heat generation at defects not only at the surface but also under the surface of inspected specimens. It allows large contrast to be shown between defective regions and defect-free areas which is useful for defect detection and characterisation using directional excitation with non-homogeneous composites. ECPT involves both electromagnetic (EM) and heat diffusion phenomena. Eddy currents are induced into an inspected specimen via an excitation coil. Then, the conductive specimen is heated by Joule heating, which is caused by resistive heating from the eddy currents. The heat generation and diffusion contributes to surface temperature distribution recorded by an IR camera. This section introduces EM and heat diffusion theory.

### 3.1.1 Maxwell's equations

The ECPT technique employs an EM field for excitation, and so it is governed by EM rules, which are a set of physical equations composed of Maxwell-Ampere's Law (see equation (3.1)), Faraday's Law (see equation (3.2)), Gauss' Law in electric (see equation (3.3)) and magnetic (see equation (3.4)) forms. Conceptually, Maxwell's equations describe how electric charges and currents act as excitation sources for the EM field. For the ECPT system, the excitation sources are electric currents. Furthermore, the relationship between the electric and magnetic fields within a system is explained, showing how a time-varying electric field generates a time-varying magnetic field and vice versa.

For general time varying EM fields, Maxwell's equations in differential form are as follows [141]:

$$\nabla \times \vec{H} = \vec{J} + \frac{\partial \vec{D}}{\partial t} \quad (3.1)$$

$$\nabla \times \vec{E} = -\frac{\partial \vec{B}}{\partial t} \quad (3.2)$$

$$\nabla \cdot \vec{D} = \rho_e \quad (3.3)$$

$$\nabla \cdot \vec{B} = 0 \quad (3.4)$$

where,  $\vec{E}$  and  $\vec{H}$  denote electric and magnetic field intensity, respectively;  $\vec{D}$  and  $\vec{B}$  stand for electric and magnetic flux density, respectively;  $\vec{J}$  is the current density;  $\rho_e$  is electric charge density; and  $t$  represents time. In addition, the relationship between  $\vec{J}$  and  $\rho_e$  can be written as in equation (3.5) [141]:

$$\nabla \cdot \vec{J} = -\frac{\partial \rho_e}{\partial t} \quad (3.5)$$

The EM phenomena in a closed system, such as an ECPT system, can be investigated at a macroscopic level when Maxwell's equations are solved in conjunction with the proper boundary conditions and constitutive representation of each material property. These can be shown as in equations (3.6)-(3.8) [141]:

$$\vec{D} = \epsilon_0 \vec{E} + \vec{P} \quad (3.6)$$

$$\vec{B} = \mu_0 (\vec{H} + \vec{M}) \quad (3.7)$$

$$\vec{J} = \sigma \vec{E} \quad (3.8)$$

where  $\vec{P}$  stands for the polarisation field and  $\vec{M}$  denotes the magnetisation field;  $\epsilon_0$  and  $\mu_0$  are the permittivity and permeability of a vacuum, respectively; and  $\sigma$  is electric conductivity. For composite materials,  $\sigma$  can be expressed as  $\sigma = [\sigma_l, \sigma_{trans}, \sigma_{cp}]^T$  due to non-homogeneity, where  $\sigma_l, \sigma_{trans}, \sigma_{cp}$  are the electric conductivities in the longitudinal, transverse and cross-ply directions with respect to the fibre orientation, respectively.

For ECPT as introduced in this thesis, frequency is set at several hundred kHz, and the wavelength of the EM wave is much larger than the dimensions of the system. As a result, the displacement current  $\vec{D}$  can be ignored. Furthermore, there is no electric charge in the ECPT system. Thus, equations (3.1) and (3.5) can be simplified as follows [141]:

$$\nabla \times \vec{H} = \vec{J} \quad (3.9)$$

$$\nabla \cdot \vec{J} = 0 \quad (3.10)$$

Here, a magnetic vector potential  $\vec{A}$  is introduced to replace  $\vec{B}$ , where  $\vec{A}$  satisfies equation (3.11):

$$\vec{B} = \nabla \times \vec{A} \quad (3.11)$$

Then, the electric field intensity  $\vec{E}$  can be expressed as:

$$\vec{E} = -\frac{\partial \vec{A}}{\partial t} - \nabla V \quad (3.12)$$

where  $V$  is scalar, denoting the electric potential.

It should be noticed that  $\vec{A}$  satisfies the Coulomb Gauge:

$$\nabla \cdot \vec{A} = 0 \quad (3.13)$$

Combining equations (3.6) and (3.7) and substituting equation (3.11) into (3.13), the governing equation describing the EM field in the ECPT system can be deduced from Maxwell's equations, for time-varying fields in particular as:

$$\sigma \frac{\partial \vec{A}}{\partial t} + \nabla \times \left( \frac{1}{\mu} \nabla \times \vec{A} \right) - \sigma \vec{v} \times (\nabla \times \vec{A}) = \sigma \frac{V_{loop}}{2\pi r} + \vec{J}_s \quad (3.14)$$

where  $\mu$  and  $\varepsilon$  are the permeability and permittivity of the inspected specimen, respectively;

$\sigma \frac{\partial \vec{A}}{\partial t}$  denotes the eddy current density;  $\vec{J}_s$  is the excitation source current density;  $V_{loop}$  is the loop potential;  $r$  is the loop radius; and  $\vec{v} = \frac{1}{\sqrt{\mu\varepsilon}}$  is the wave velocity in media.

Equation (3.14) is a partial differential equation which can be solved in a numerical simulation. Once  $\vec{A}$  is obtained via equation (3.14), all of the EM variables in the ECPT system can be derived.

### 3.1.2 Heat diffusion equations

Through Maxwell's equations as described in section 3.1.1, the eddy current density  $\bar{J}_s$  or electric field intensity  $\bar{E}$  can be solved. The resistive heat  $Q$  generated is proportional to the square of the eddy current density  $\bar{J}_s$  or electric field intensity  $\bar{E}$ . The relationship between  $Q$ ,  $\bar{J}_s$  and  $\bar{E}$  is governed by the following equation:

$$Q = \frac{1}{\sigma} |\bar{J}_s|^2 = \frac{1}{\sigma} |\sigma \bar{E}|^2 \quad (3.15)$$

In reality,  $\sigma$  is the temperature-dependent electrical conductivity of the inspected specimen, which is given by:

$$\sigma = \frac{\sigma_r}{1 + \alpha_\sigma (T - T_r)} \quad (3.16)$$

where  $\sigma_r$  is the conductivity at the reference temperature  $T_r$ ;  $T$  denotes the temperature distribution; and  $\alpha_\sigma$  is the temperature coefficient of resistivity, showing how the resistivity varies with temperature.

The heat diffusion equation of a specimen caused by a Joule heating source  $Q$  is governed by the following equation:

$$\rho C_p \frac{\partial T}{\partial t} - \nabla \cdot (k \nabla T) = Q \quad (3.17)$$

where  $\rho$ ,  $C_p$  and  $k$  are density, heat capacity and thermal conductivity, respectively.

The derived equations (3.14), (3.15), (3.17) can be used for solving the interaction of EM and thermal numerically, which is further discussed in Section 3.2. With defined excitation current density, the magnetic vector potential  $\bar{A}$  can be derived via equation (3.14). Then the EM variables are calculated from  $\bar{A}$ . The link between ‘induction currents’ and ‘heat transfer’ is the resistive heating  $Q$ , which can be derived from equation (3.15). Finally, the temperature distribution  $T$  can be solved in ‘heat transfer’ module via equation (3.17). In addition, these theoretical concerns also help in understanding the multiple-physic phenomena in experimental studies, as well as extracting transient features for defect detection, classification and characterisation.

### 3.2 Numerical simulation models of ECPT

Numerical simulation can help in the design and development of ECPT techniques and experimental systems for blade defect detection without being too costly. The numerical simulation in this thesis is conducted in order to understand the experimental phenomena, and investigate and validate the relationship between the extracted features and defect dimensions in forward and inverse problems. EM simulation methods can be divided into the time and frequency domains. Moreover, based on solving integral or differential equations, the simulation methods can be further categorised as integral and differential solvers [142].

FEM normally requires the problem structure being tetrahedrally meshed where the  $\bar{E}$  and  $\bar{H}$  fields are unknown to solve [143]. Therefore, the full problem structure is divided into many smaller regions and the field is represented in each sub-region or element by a local linear function. Therefore, FEM is good at solving structures with complex shapes. In addition, another advantage of FEM is that it can solve problems for excitations from several ports simultaneously, which it is suitable for multiple-port system. Moreover, FEM is suitable for the simulation of multiple physics, where EM, thermal and mechanical mechanisms for example are coupled together. However, the memory requirements and time required are quite high, which is a major drawback of FEM compared with finite integral technology (FIT) or finite difference time domain (FDTD) methods, especially when the dimensions of the structure are electrically large.

FIT is a time domain algorithm which discretises the integral rather than the differential form of Maxwell's equations. On a Cartesian grid, FIT is equivalent to FDTD [144], which regards the  $\vec{E}$  and  $\vec{H}$  fields as unknowns and requires square and cube meshes. The excitations of time-domain solvers are typical signals such as a Gaussian pulse containing the frequency bandwidth of interest. In other words, FIT can solve the frequency response with one time-domain signal, unlike the FEM which requires separate calculations for each frequency. As a result, the key advantage of FIT is fast calculation and low memory consumption when working at high frequency. This is because all signals decay to zero in ideal situation at the end of a time domain simulation, and the signal can be prolonged by adding zeros at the end in order to increase signal length  $t_{max}$  [145]. According to the Nyquist-Shannon theorem, the frequency resolution for limited-bandwidth signals is governed by  $\Delta f = 1/(2t_{max})$ . That means that the spectrum with an arbitrarily fine frequency resolution can be calculated without additional computational effort.

From the comparison of FEM and other numerical methods, COMSOL is selected to model ECPT for several reasons. The EM wavelength is much larger than the dimensions of the specimen, and the system works at a single frequency. Thus, the disadvantages of FEM of requiring separate calculations for each frequency and problems of time-consuming can be ignored. In solving the combination of EM and thermal phenomena in ECPT, 'Electro-Thermal' module is used. In this module, the interaction of electric and magnetic fields is calculated via 'induction currents' and the temperature distribution is simulated by a "heat transfer" functionality.

With the defined excitation current density in COMSOL, the magnetic vector potential  $\vec{A}$  can be derived via equation (3.14). Then the EM variables are calculated from  $\vec{A}$ . The link between 'induction currents' and 'heat transfer' is the resistive heating  $Q$ , which can be derived from equation (3.15). Finally, the temperature distribution  $T$  can be solved in 'heat transfer' via equation (3.17). Numerical modelling helps in the design of experimental system for non-homogeneous and anisotropic samples and the validation of the experimental results.



### 3.3 Experimental systems and samples for case studies

The ECPT system diagram is illustrated in Figure 3.2. In the system, a high-frequency and high-power signal generator provides high power currents for induction heating. The infrared (IR) camera and induction heater are controlled by a square pulse signal from the same pulse generator. The IR camera is also used to record the thermal videos and for switching on the induction heater. The thermal videos are transmitted to a PC for visualisation and post-processing, including defect classification and electrical/thermal property evaluation.

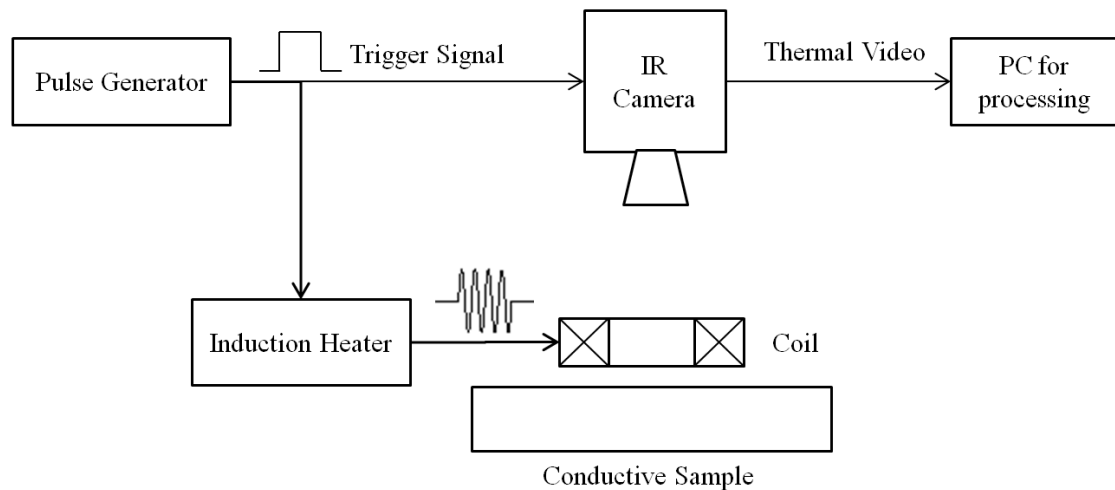


Figure 3.2 ECPT system diagram

As shown in Figure 3.3, an Easyheat 224 from Cheltenham Induction Heating is used for coil excitation at Newcastle University. The Easyheat has a maximum excitation power of 2.4 kW, a maximum current of 400 A<sub>rms</sub> and an automatic resonant excitation frequency range of 150 kHz - 400 kHz, where values of 380A<sub>rms</sub> and 256 kHz are used in the experiments for a rectangular coil. In general, high excitation frequencies will lead to high thermal contrast or high temperature increase. The time domain information will allow the derivation of defect profile information. The system has a quoted rise time from the start of the heating period to full power of 5 ms, which was verified experimentally. Water-cooling of the coil is implemented to counteract the direct heating of the coil. The Flir SC7500 is a Stirling cooled camera with a 320 x 256 array of 1.5 - 5 μm InSb detectors. The camera has a sensitivity of <20 mK and a maximum

full frame rate of 383 Hz. The maximum 383 Hz frame rate provides one frame every 2.6 ms, with options to increase the frame rate with windowing of the image. In these experimental studies, a high-speed thermal camera is used for the investigation including feature optimisation for QNDE. However, in real applications, it may be unnecessary to use such a high-end camera. A rectangular coil, as shown in Figure 3.4a, is constructed from 6.35 mm high-conductivity hollow copper tube. The coil is selected to introduce parallel eddy currents in the direction of maximum conductivity in the sample.

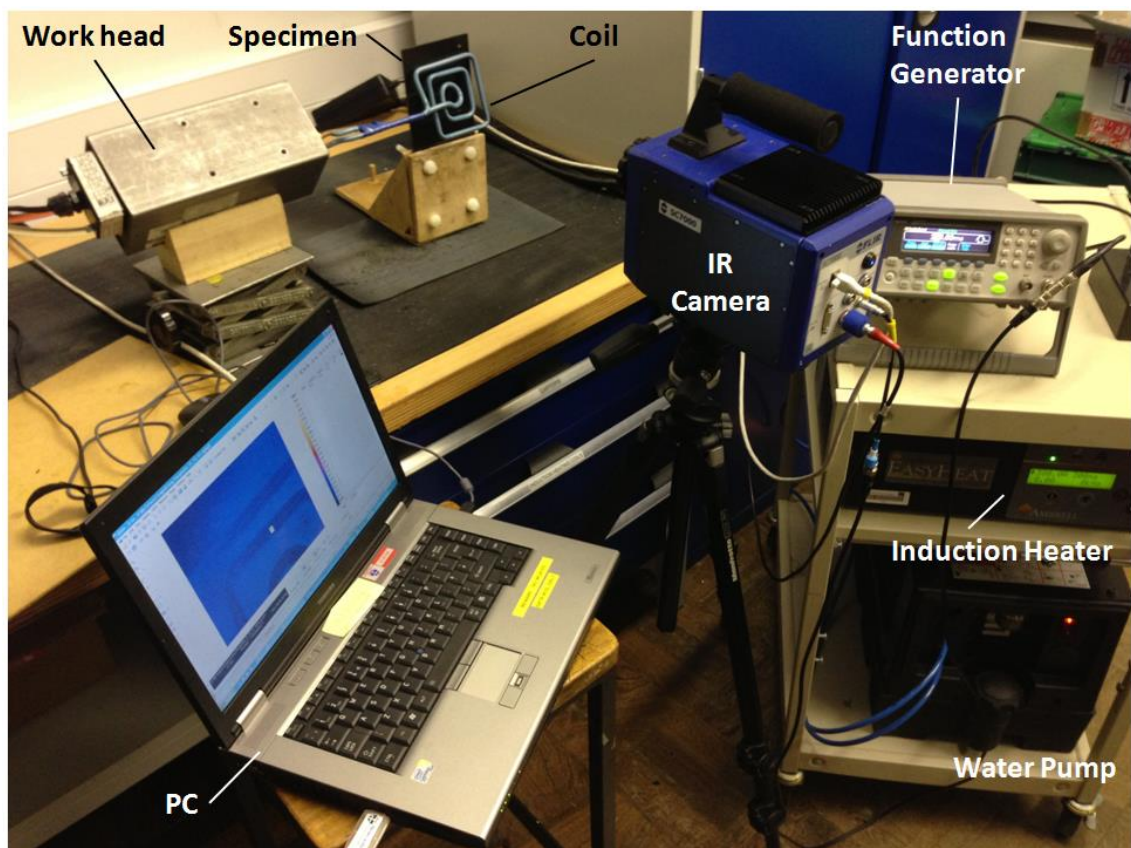


Figure 3.3 Experimental setting-up at Newcastle University

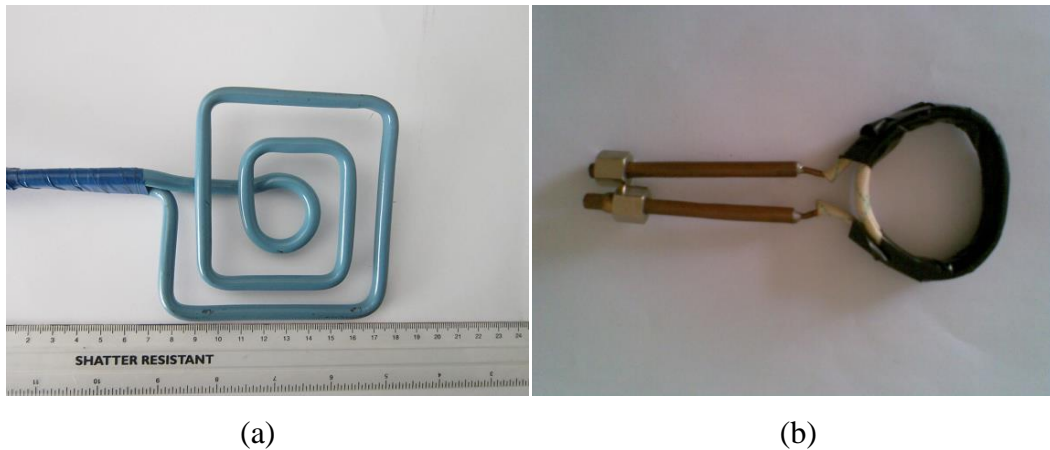


Figure 3.4. (a) Rectangular coil used in Newcastle and (b) circular coil used in NUAA

Samples with delaminations are tested at the Nanjing University of Aeronautics and Astronautics (NUAA), China through the exchange via HEMOW project. A HB-X5K high frequency heater with a work head linked to a coil from Wuxi Gaopin Technology Co., Ltd is used for eddy current excitation. The heater provides a maximum output of 2 kW at 320 kHz. The diameter of the copper tube is 2.08 mm and the outer diameter of the circular coil is approximately 50 mm, as shown in Figure 3.4b. A Flir ThermaCAM S65 is used to record thermal images and videos. The IR camera has a maximum full frame rate of 50 Hz; providing one frame every 20 ms. In contrast to the system built at Newcastle University, a lower-end IR camera was employed at NUAA with lower frame rates of 50 Hz in comparison to 383 Hz in the work at Newcastle. This camera was used in conjunction with a battery and thermal video memory card. It is hoped that these different camera systems will be suitable for offshore inspection. Therefore, without a water-cooling system for the coil, the recording period for only one inspection is investigated in order to avoid overheating of the coil. In order to make experimental repeatable and reliable, the stand-off distance between the coil and sample is kept within a range from 0.5mm to 1mm.

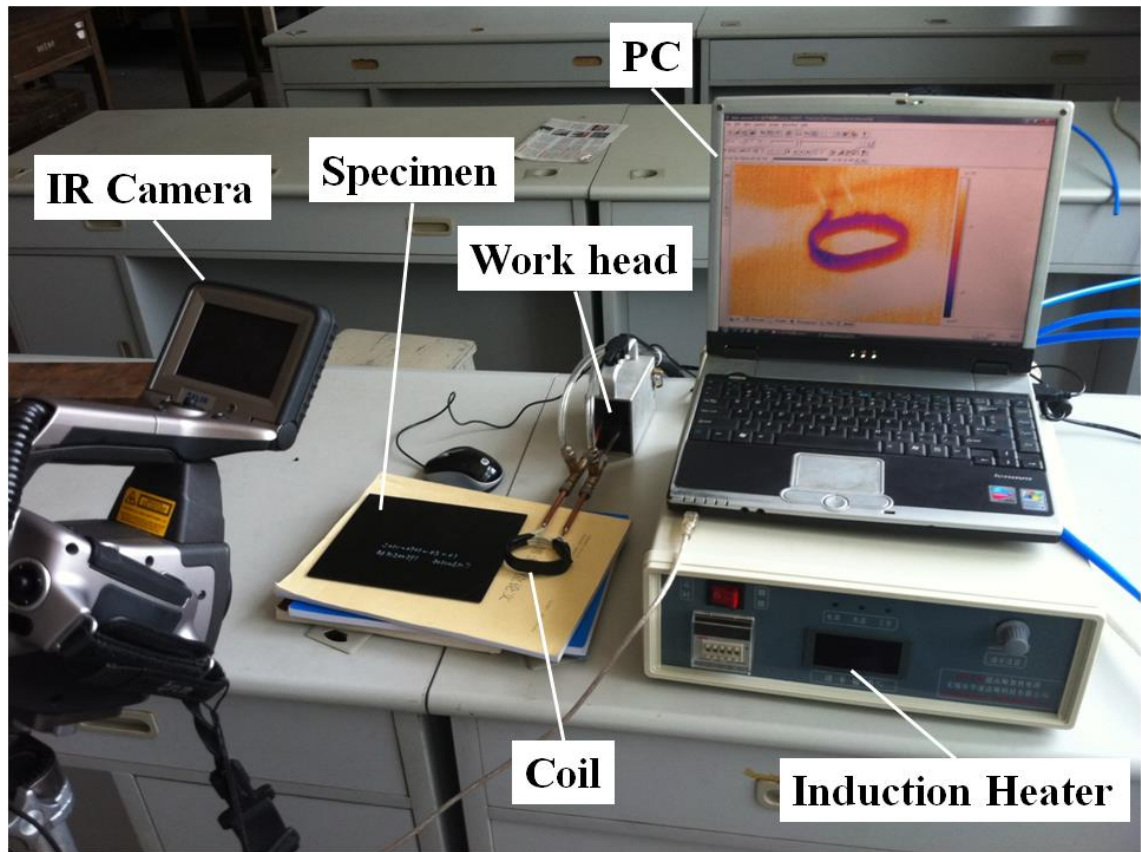


Figure 3.5 Experimental set-up at NUAA

Normally, two modes are used in experimental studies, the transmission mode and reflection mode, as shown in Figure 3.6. Transmission mode means that the coil and thermal camera are placed at different sides of the sample, whereas in reflection mode the coil and thermal camera are placed at the same side of the sample. The use of reflection mode can maximise the heating on the surface to be inspected, but the coil hides a part of sample in the experiment. Transmission mode can avoid the area of the sample hidden by the coil, but the heat is attenuated when it propagates towards the inspected surface. Thus, a trade-off of mode selection needs to be found in different situations. Although transmission mode is not always available in real applications, the results from this mode can help in understanding the phenomena involved and allowing comparison with these results from the reflection mode.

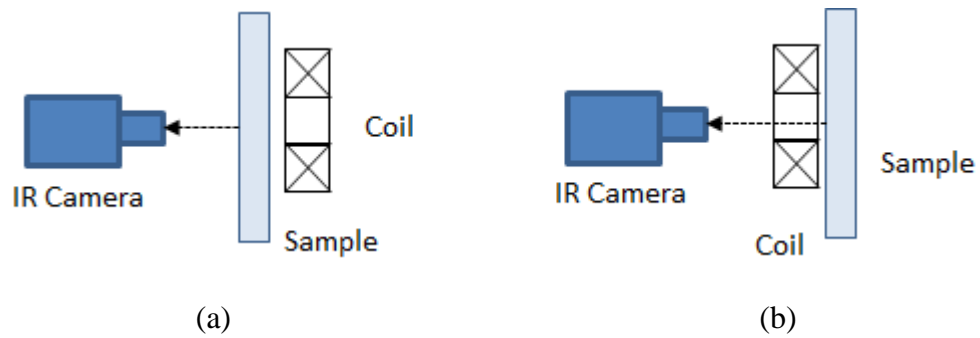


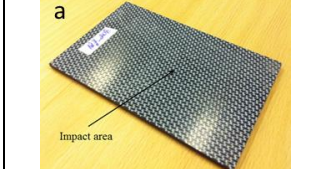



Figure 3.6 Illustration of (a) transmission mode and (b) reflection mode

To investigate the transient thermal behaviours of ECPT for different types of defects, four sets of samples with crack, delamination or impact damage are prepared for case study. Information about the sample and defects is listed in TABLE 3-I. Detailed information about each set of samples is given in the individual case studies in the following chapters. Samples with cracks or impact damage are investigated at Newcastle University and samples with delaminations are tested at NUAA.

Table 3-I Defect descriptions and sample selections

	Dimensions (mm)	Defect Information	Picture
Crack sample Set 1	350 × 38 × 6	Depth (0.5 mm, 1 mm or 2 mm) notches are manufactured	
Impact damage sample Set 2	150 × 100 × 4	Damaged by low velocity impact of unknown dimension and impact energy	
Impact damage sample Set 3	150 × 100 × 3.8	Dropping weight impact from 4J to 12J	
Delamination sample Set 4	20-layered, 180 × 140 × 3.1	Polytetrafluoroethylene film simulating delamination inserted at different layers; thickness 0.2mm; diameters: 6mm, 10mm and 15mm	

### 3.4 Interpretation and characterisation algorithms

Raw thermal video only provides temperature distribution on the surface of the sample. A further processing is required on the thermal videos or saying thermal image sequences obtained from ECPT system, in order to gain quantitative information about the defects under inspection. In this thesis, three different levels at pixel, local area and pattern are proposed. For the investigation at the pixel level, the transient temperature response  $T(t)$  and the first derivative of it  $dT/dt$  at selected hot-spots are evaluated. Surface defects result in clear hot-spots, which is easy for pixel selection. But hot-spots are blurred when the defect is inside the sample. For those cases, investigation at local area or pattern level is required. For the investigation at local area and pattern level, OF and PCA/ICA respectively are implemented to avoid problems in pixel selection.

OF is proposed to extract flow distribution at the surface, in order to track the heat propagation and interaction at the defective regions. From the extracted flow patterns, three types of defects can be classified.

An integration of PCA and ICA on the transient thermal videos is proposed. This method enables spatial and temporal patterns to be extracted according to the transient response behaviour without any training knowledge. In the first step, the data is transformed to orthogonal principal component (PC) subspace and the dimension is reduced using PCA. Multichannel Morphological Component Analysis (MMCA), as an ICA method, is then implemented to deal with the sparse and independence property for detecting and separating the influences of different layers, defects and their combination information in CFRP.

In this section, the algorithms of OF and integration of PCA and ICA are presented, respectively.

#### *3.4.1 Optical Flow for NDE at the local area level*

Optical flow is firstly calculated to trace the motion between two thermal images at times  $t$  and  $t+\Delta t$ . It is based on local Taylor series approximations of the image signal, which means that partial derivatives with respect to the spatial and temporal coordinates are used. In this case, the thermal image sequence is seen as a three-dimensional matrix

with respect to location  $x$  and  $y$  and time  $t$ . A voxel at location  $(x, y, t)$  with intensity which corresponds to temperature in this thesis  $I(x, y, t_i)$  will have moved by  $\Delta x$ ,  $\Delta y$  and  $\Delta t = t_j - t_i$  between the two images, which can be given as:

$$I(x, y, t_i) = I(x + u, y + v, t_j) \quad (3.18)$$

In this thesis, the displacement between two images stands for the variation in temperature, which reflects the heat propagation. Assuming that the displacement is small, the image constraint at  $I(x, y, t)$  with the Taylor series can be developed to give:

$$I(x + \Delta x, y + \Delta y, t + \Delta t) = I(x, y, t) + \frac{\partial I}{\partial x} \Delta x + \frac{\partial I}{\partial y} \Delta y + \frac{\partial I}{\partial t} \Delta t + O(\Delta x^2, \Delta y^2, \Delta t^2) \quad (3.19)$$

From these equations it follows that:

$$\frac{\partial I}{\partial x} \Delta x + \frac{\partial I}{\partial y} \Delta y + \frac{\partial I}{\partial t} \Delta t = 0 \quad (3.20)$$

or

$$\frac{\partial I}{\partial x} \frac{\Delta x}{\Delta t} + \frac{\partial I}{\partial y} \frac{\Delta y}{\Delta t} + \frac{\partial I}{\partial t} \frac{\Delta t}{\Delta t} = 0 \quad (3.21)$$

which results in:

$$\frac{\partial I}{\partial x}V_x + \frac{\partial I}{\partial y}V_y + \frac{\partial I}{\partial t}V_t = 0 \quad (3.22)$$

where  $V_x$  and  $V_y$  are the  $x$  and  $y$  components of the velocity or optical flow of  $I(x, y, t)$  and  $\partial I/\partial x$ ,  $\partial I/\partial y$  and  $\partial I/\partial t$  are the derivatives of the image at  $(x, y, t)$  in the corresponding directions.  $I_x$ ,  $I_y$  and  $I_t$  can be written to stand for the derivatives in the following.

Thus:

$$I_x V_x + I_y V_y = -I_t \text{ or } \nabla I^T \cdot \vec{F} = -I_t \quad (3.23)$$

This is an equation in which there are two unknowns and therefore it cannot be solved as it stands. This is known as the aperture problem with optical flow algorithms. To find the optical flow, another set of equations is needed, by incorporating some additional constraint. In this thesis, the Horn-Schunck method is used for implementation, where the flow is formulated as a global energy function which is solved through minimisation.  $\vec{F} = [V_x, V_y]^T$  is the optical flow vector.

$$E = \iint [(I_x V_x + I_y V_y + I_t)^2 + \alpha^2 (\|\nabla V_x\|^2 + \|\nabla V_y\|^2)] dx dy \quad (3.24)$$

where  $\alpha$  is regularisation constant. The larger  $\alpha$  leads to the smoother flow estimation.



### *3.4.2 PCA/ICA for NDE at the pattern level*

From all samples listed in TABLE 3-I, it can be seen that the area of the defect in the sample is much less than those of the surrounding, which indicates the sparse property of inspected samples. Here, ‘sparseness’ refers to a representational scheme where only a few units out of a large population are effectively used to represent typical data vectors [146].

The deviation of material property at defects refers to the decrease of electric conductivity and increase of thermal conductivity at impact damage [C2]. This directly results in the transient thermal responses in the defective region, independent to those in the defect-free area.

Figure 3.7 illustrates the procedure of defect identification and separation by using the ECPT video sequences. Firstly, the data is transformed into orthogonal PC subspace and the dimension of the data is reduced by using PCA. Multichannel morphological component analysis (MMCA) is then applied to deal with the properties of sparseness and independence in order to detect defects in CFRP. By using MMCA, the different characteristics of transient responses related to the defect and area without defects can be separated. Subsequently, the cross-correlation of the estimated mixing vectors derived from MMCA for both the thermal transient video with defect and the one without any defect are calculated. The maximum/minimum of correlation values of can be used to identify the influence of the different types of defects and non-defect factors. Figure 3.7 shows the flow diagram for the proposed method. In the figure, the ‘defect’ and ‘non-defect’ thermal videos are recorded by using the same sample at the defective area and non-defective area, respectively. The record area and the relevant coil position in details are presented in Chapter 6.

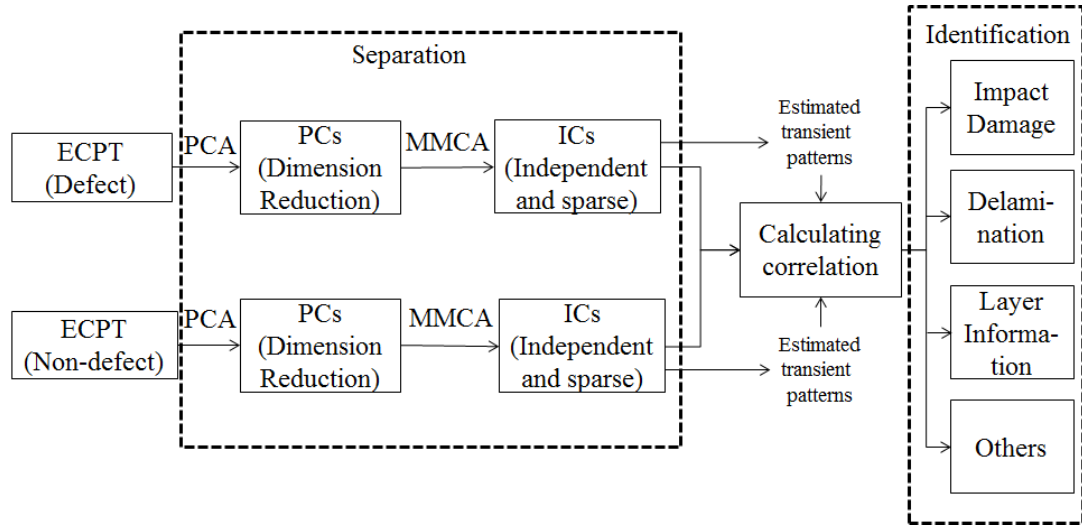


Figure 3.7 Procedure for defect identification and separation

In the following sub-sections, the individual algorithms for PCA and MMCA are explained.

#### 3.4.2.1 PCA for NDE at the pattern level

PCA is a multivariate analysis technique which transforms the original measured data into new uncorrelated variables termed principal components (PC). The original measured data are treated as independent variables, and each PC is a linear combination of the original variables. These PCs form the basis of the respective vector space and they are arranged in order of decreasing variance. Thus, the first PC carries most of the information regarding the original data and so on. The use of PCA methods in PEC testing can be found in previous work [147]-[148], and in this thesis, they are used for defect detection and classification of ECPT videos.

In this thesis, each thermal image (also called a frame) from a thermal video is converted into a  $k$ -element vector as a mixing observation on the defect, the defect-free area, the fibre texture *etc.* Then  $N$  recorded frames form an input matrix  $\mathbf{I}_M$ , where the measurement  $\mathbf{I}_M$  with a size of  $N \times k$  is used for PCA calculation. For example,  $N=383$ ,  $k=320 \times 256=81920$  pixels in the thermal image when the thermal video is recorded at a frame rate of 383 Hz for one second. As a result, these  $N$  output PCs with  $k$  elements are

obtained with different weights (eigenvalues). The first  $m$  PCs ( $P=8$ ) with a decent weight are selected. The corresponding output vector for each PC is converted into an image shown as the PCA result. The PCA calculation procedure is shown in Figure 3.8.

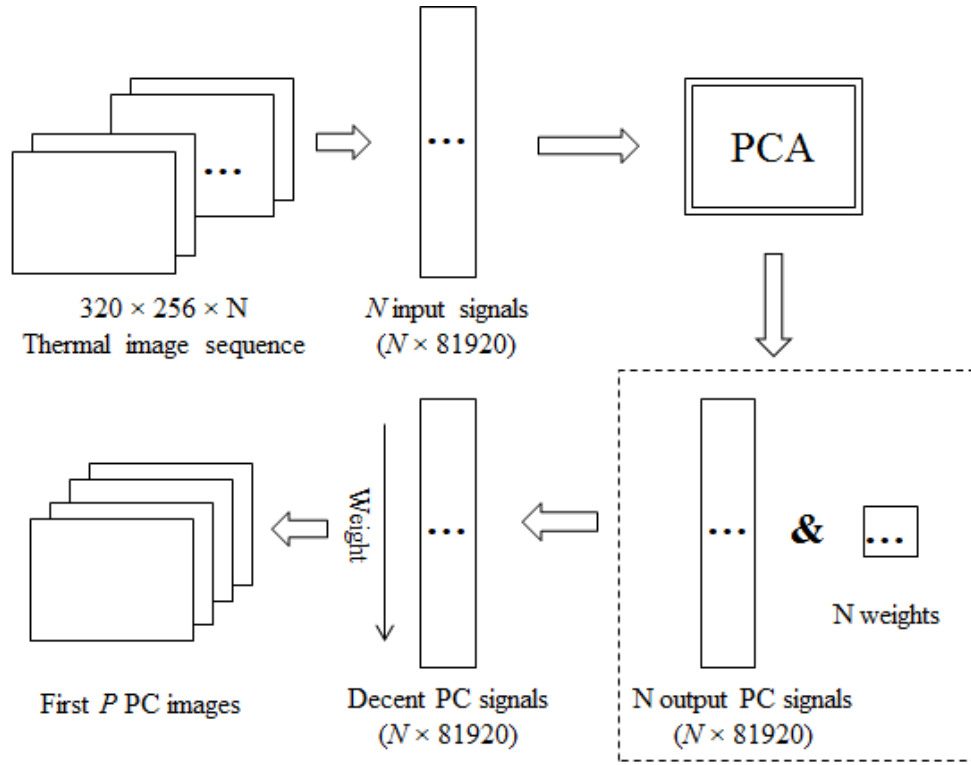


Figure 3.8 PCA procedure with thermal videos

To conduct PCA on the  $N$  input signals, eigenvalue decomposition of the covariance of the input 2D matrix  $\mathbf{I}_M$  is used. By using eigenvalue decomposition,  $\mathbf{I}_M$  can be transformed into uncorrelated sources by means of a whitening matrix. The covariance of  $\mathbf{I}_M$  can be expressed as  $E\{\mathbf{I}_M \mathbf{I}_M^T\} = \mathbf{E} \mathbf{D} \mathbf{E}^T$ , where  $\mathbf{E}$  is the orthogonal matrix of eigenvectors and  $\mathbf{D} = \text{diag}(\lambda_1, \dots, \lambda_N)$ .  $\lambda_1 \geq \dots \geq \lambda_N$  are the decent eigenvalues. Thus, the covariance of  $\mathbf{I}_M$  is an  $N \times k$  matrix where  $k$  is the product of the row and column of the image (e.g.  $320 \times 256 = 81920$ ) where this can be rewritten as:

$$\begin{aligned} E\{\mathbf{I}_M \mathbf{I}_M^T\} &= \mathbf{E} \mathbf{D} \mathbf{E}^T = \mathbf{E} \mathbf{D}^{1/2} \mathbf{D}^{1/2} \mathbf{E}^T = E\{\mathbf{W}_{PCA}^{-1} \mathbf{X}_{PCA} \mathbf{X}_{PCA}^T \mathbf{W}_{PCA}^{-1 T}\} \\ &= \mathbf{W}_{PCA}^{-1} E\{\mathbf{X}_{PCA} \mathbf{X}_{PCA}^T\} \mathbf{W}_{PCA}^{-1 T} = \mathbf{W}_{PCA}^{-1} \mathbf{W}_{PCA}^{-1 T} \end{aligned} \quad (3.25)$$

In Equation (3.25),  $E\{\mathbf{X}_{PCA} \mathbf{X}_{PCA}^T\} = \mathbf{I}$  where  $\mathbf{I}$  is the identity matrix. Therefore,  $\mathbf{W}_{PCA} = (\mathbf{E}\mathbf{D}^{1/2})^{-1} = \mathbf{D}^{1/2}\mathbf{E}^T$ , and whitening can be written as:

$$\mathbf{X}_{PCA} = \mathbf{W}_{PCA}\mathbf{I}_M \quad (3.26)$$

where  $\mathbf{W}_{PCA}$  is the estimated de-correlation matrix and  $\mathbf{X}_{PCA}$  is the uncorrelated sources by using PCA. The mixing matrices  $\mathbf{M}_{PCA} = \mathbf{W}_{PCA}^{-1} = [\mathbf{m}_{P1}, \mathbf{m}_{P2}, \dots, \mathbf{m}_{PN}]$  and  $\mathbf{m}_{P1}, \mathbf{m}_{P2}, \dots, \mathbf{m}_{PN}$  are the mixing vectors of PCA.

By using PCA,  $N$  orthogonal signals can be derived to form PC images, where any two of the  $N$  images are uncorrelated to each other. For the thermal sequence, the aim of using PCA is to maximise the contrast between defective and defect-free regions. In addition, the dimension of data is reduced to  $P$ , rather than  $N=383$ . Because PCA cannot guarantee the statistical independence of the above regions, therefore the defective region and defect-free area cannot be completely separated. This means that PCA is not ideal for enhancing defects and separating different defects in one operation. Thus, the use of ICA is subsequently proposed to overcome these problems, since this technique aims to find the maximum independent signals rather than orthogonal ones for the separation.

#### 3.4.2.2 ICA and MMCA for NDE at the pattern level

The ICA learning algorithm searches for linear transformation which makes the components as statistically independent as possible, as well as maximises the marginal densities of the transformed coordinates for the given training data. Multichannel morphological component analysis (MMCA) is used as one of the ICA separation algorithms. MMCA takes advantage of the sparse representation of multichannel data in large over-complete dictionaries to separate features in the data based on their morphology, even with the presence of noise [149]. A defect in CFRP as described in TABLE 3-I meets the sparse feature criterion, since the pixel number of informational data at a defective region is much smaller than that of the overall image. Thus, MMCA is chosen in this thesis.

After the reduction of the data dimension using PCA, the measurement  $\mathbf{I}_M$  is re-sized as  $\mathbf{I}'_M$  with dimensions  $P \times k$ , which can be written as a multiplication of the estimated de-correlation matrix  $\mathbf{X}_{ICA}$  and mixing matrix  $\mathbf{M}_{ICA}$  plus noise:

$$\mathbf{I}'_M = \mathbf{M}_{ICA} \mathbf{X}_{ICA} + \mathbf{N}_{noise} \quad (3.27)$$

where  $\mathbf{I}'_M$  is the reduced dimension matrix of  $\mathbf{I}_M$  with the size of  $P \times k$ . The rows of  $\mathbf{I}'_M$ ,  $\mathbf{X}_{ICA}$  and  $\mathbf{M}_{ICA}$  are  $\mathbf{i}_m$ ,  $\mathbf{x}_{im}$  and  $\mathbf{m}_{im}$  ( $m=1, 2, \dots, P$ ), respectively. Each  $\mathbf{x}_{im}$  ( $m=1, 2, \dots, P$ ) can be described as  $\mathbf{x}_{im}^T = \Phi_m \alpha_m$  with an over-complete dictionary  $\Phi_m$  and a sparse representation  $\alpha_m$ .

The estimation of  $\mathbf{X}_{ICA}$  and  $\mathbf{M}_{ICA}$  is governed by the following equation [149]:

$$\{\hat{\mathbf{M}}_{ICA}, \hat{\mathbf{X}}_{ICA}\} = \arg \min_{\mathbf{M}_{ICA}, \mathbf{X}_{ICA}} \|\mathbf{I}'_M - \mathbf{M}_{ICA} \mathbf{X}_{ICA}\|_F^2 + \sum_m \lambda_m \|\mathbf{x}_{im} \Phi_m^+\|_1 \quad (3.28)$$

where  $\|\mathbf{M}\|_F^2 = \text{trace}(\mathbf{M}^T \mathbf{M})$ , here 'F' denotes the Frobenius norm, and  $\Phi_m^+$  is the updated  $\Phi_m$  in the next iteration;  $\lambda_m$  denotes the sparse parameters and  $\|\mathbf{x}_{im} \Phi_m^+\|_1$  forms the  $L_1$ -norm regularisation. From equation (3.28), by minimising the objective function with respect to  $\mathbf{x}_{im}$  when  $\mathbf{m}_{im}$  is fixed, it can be derived using equation (3.29) [149]:

$$\mathbf{x}_{im} = \frac{1}{\|\mathbf{m}_{im}\|_2^2} [\mathbf{m}_{im}^T \mathbf{I}_m - \frac{\lambda_m}{2} \text{sign}(\mathbf{x}_{im} \Phi_m^+) \Phi_m^{+T}] \quad (3.28)$$

where  $\mathbf{I}_m = \mathbf{I}'_M - \sum_{m' \neq m} \mathbf{m}_{m'} \mathbf{x}_{im'}$ . The MMCA algorithm is presented as follow with a algorithm flow [149]:

By using MMCA, the different characteristics of transient responses related to the defect and area without defects can be separated into mixing vectors. Subsequently, the cross-correlation of the estimated mixing vectors derived from MMCA for both the thermal transient video with defect and the one without any defect are calculated. The maximum/minimum of correlation values of can be used to identify the influence of the different types of defects and non-defect factors.

1. Set number of iterations  $L_{\max}$  & threshold  
 $\forall m, \delta_m = L_{\max} \lambda_m / 2$
  2. While  $\delta_m > \lambda_m / 2$ ,  
 For  $m=1, 2, \dots, P$ 
    - Re-normalise  $\mathbf{m}_{im}$  and  $\mathbf{x}_{im}$
    - Update  $\mathbf{x}_{im}$  assuming all  $\mathbf{x}_{i m' \neq m}$  and  $\mathbf{m}_{im'}$  are fixed
      - Compute the residual  $\mathbf{I}_m = \mathbf{I}_M - \sum_{m' \neq m} \mathbf{m}_{m'} \mathbf{x}_{im'}$
      - Project  $\mathbf{I}_m$ :  $\tilde{\mathbf{x}}_{im} = \frac{1}{\|\mathbf{m}_{im}\|_2} \mathbf{m}_{im}^T \mathbf{I}_m$
      - Compute  $\alpha_m = \tilde{\mathbf{x}}_i \Phi_m^+$
      - Soft threshold  $\alpha_m$  with threshold  $\delta_m$ , yielding  $\tilde{\alpha}_m$
      - Reconstruct  $\mathbf{x}_{im}$  by  $\mathbf{x}_{im} = \tilde{\alpha}_m \Phi_m^{+T}$
    - Update  $\mathbf{m}_{im}$  assuming all  $\mathbf{x}_{im}$  and  $\mathbf{m}_{m' \neq m}$  are fixed:
      - $m_m = \frac{1}{\|\mathbf{x}_{im}\|_2} \mathbf{I}_m \mathbf{x}_{im}^T$
- Lower the thresholds:  $\delta_m = \delta_m - \lambda_m / 2$

### 3.5 Chapter summary

In this chapter, the research diagram is outlined, which includes: an ECPT technique development with theoretical concerns, numerical modelling and the experimental studies, three levels of investigation of data gained from EPCT system in line with the knowledge from failure models, and the detection, classification and characterisation of

defects. The theoretical considerations, numerical modelling and experimental system set-up as well as sample preparation are reported.

Analytical modelling provides an understanding of the physical phenomena. Numerical modelling helps in the design of experimental system for non-homogeneous and anisotropic samples and is used to validate the experimental results. Experimental system is implemented for real samples with defects. From the theoretical background of ECPT, Maxwell's equations and their relevant deductions, in conjunction with heat diffusion equations, are introduced. The governing equations (3.14), (3.15) and (3.17) are derived to solve EM and thermal phenomena. The use of FEM numerical simulation in COMSOL to solve multiple-physical problems and the advantages of this compared to other methods are discussed. Following numerical modelling, the set-up of the ECPT experimental system and sample details are presented.

Based on the ECPT systems and failure models summarised in Chapter 2, transient thermal responses are investigated. Through numerical simulations and experimental studies, the relationship between extracted features and defects in forward and inverse problems can be established at different levels, according to defect location and fibre textures. As the complexity of fibre texture or defect increases, pixel, local area and pattern level analysis are selected. The relevant processing algorithms for the analysis extended from transient responses are explained, which includes optical flow for at local area level, and PCA/ICA for the pattern level. Different samples with different defects are used as case studies at the pixel, local area and pattern levels in the following Chapters 4, 5 and 6 respectively.

## **Chapter 4. ECPT INVESTIGATION AT THE PIXEL LEVEL**

In Chapter 3, the theoretical background, numerical modelling and experimental system set-up as well as sample preparation have been reported. In this chapter, numerical modelling and experimental studies are applied to investigate the ECPT phenomena at pixel level, including the transient eddy current distribution and its interaction with defects, and the Joule heating caused by the eddy currents as well as the heating propagation and interaction with defects. Two case studies of crack and impact damage are presented for a comparison of defect location and fibre texture. The case study of cracks concerns surface defect in uni-directional fibres and the impact damage case shows not only surface but also interior defects in woven fibre. Through the analysis of transient responses, defects are characterised via features extracted at the pixel level. In addition, the transient responses of different defects are used to classify defect types using the PCA algorithm.

### **4.1 Transient response extraction at pixel level**

In order to undertake the investigations at the pixel level, the transient thermal response at each pixel is extracted from the thermal video/image sequence, as shown in Figure 4.1. Features at specific pixels in the defective region are extracted to gather quantitative information about and classify the defect.



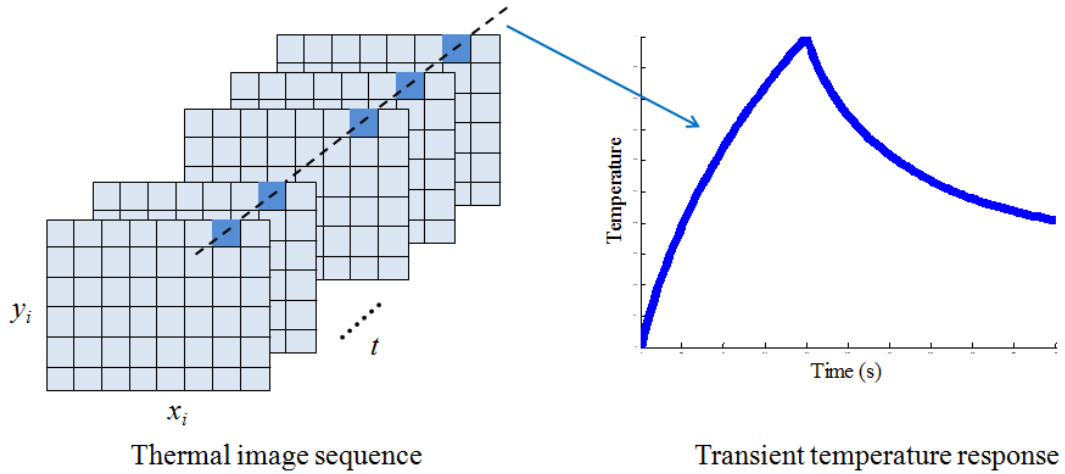


Figure 4.1 Illustration of capture of transient temperature response from a thermal image sequence.

Once a thermal video is captured from the IR camera, the thermal image for each frame can be read and a 2D matrix  $I(x, y)$  can be formed to illustrate the temperature at each pixel in the thermal image using Matlab. Therefore, a 3D matrix  $I(x, y, n)$  can be generated to present the temperature at each pixel at each frame in the whole thermal video, where  $n$  denotes the number of frames.  $I(x, y, n)$  can also be expressed as  $I(x, y, t)$ , where  $t = n/fs$ , and  $fs$  denotes the frame rate of the IR camera. From Figure 4.1, it can be seen that, when a pixel  $(x_i, y_i)$  is selected, the temperature against time  $t$  at that pixel can be derived as a vector  $T_{x_i, y_i}(t) = I(x_i, y_i, t)$ . The temperature at the first frame is assumed to be zero in this thesis, and thus the transient temperature response at that pixel is expressed as  $\Delta T_{x_i, y_i}(t) = I(x_i, y_i, t) - I(x_i, y_i, t_0)$ .

After obtaining the transient temperature response, features such as rate of temperature increase, and delay rate, are extracted from the heating and cooling phases respectively to investigate the dimensions of defect or variations in local physical properties. Two case studies of cracks and impact damages are undertaken in the next two sections. The case study of cracks shows the condition when the fibre texture is simple (uni-directional fibre) and the defect is on the surface of the specimen. The impact damage case study demonstrates the case when the fibre texture is complex and the defect is at the sub-surface of the specimen or at even deeper levels. Also, the transient responses for different defects are used in section 4.4 to classify the type of defect using PCA classification algorithm.

## 4.2 Case study 1: crack detection and characterisation

In this section, cracks in uni-directional fibre samples are studied to show that the directional excitation along the fibre orientation maximises induction heating. Information about the depth and width of cracks can be derived from the transient features at the pixel level via numerical simulation and experimental study.

### 4.2.1 Sample description

A 350 mm × 38 mm × 6 mm CFRP sample provided by Exel Composites UK is named sample “Set 1” in TABLE 3-I. The sample contains three cracks which are 1 mm wide, varying in depth at 0.5 mm, 1mm and 2 mm. The cracks were manufactured in the workshop at Newcastle University. A photograph and diagram showing the fibre texture of the CFRP sample are given in Figure 4.2.

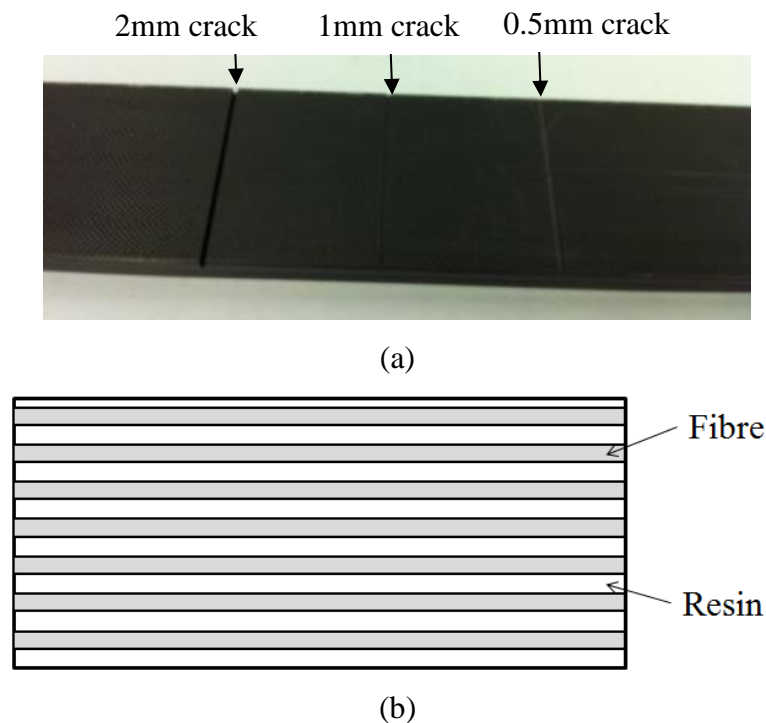


Figure 4.2 Cracked sample (a) photograph ; (b) diagram of the fibre texture in top view.

## 4.2.2 Numerical simulation study

### 4.2.2.1 Numerical model and parameter setup

In the simulation, the thickness and width of the sample are set to be the same as in the sample introduced in Section 4.2.1, while the length of the sample is reduced to allow faster calculation, since there is no need to model over the whole length. A single crack in the sample with varied depth or width is simulated, as shown in Figure 4.3. Cracks with width  $w$  (0.1 mm, 0.5 mm, 1 mm or 2 mm) and depth  $d$  (0.5 mm, 1 mm, 2 mm or 4 mm) are simulated. The excitation frequency and current are set at 256 kHz and 380 A<sub>rms</sub> to match the experimental set-up. A rectangular coil is used in the experiments with the set-up shown in Figure 3.4a. In this case, the eddy currents are induced predominantly by the coil edge that is closest to the sample. Thus, only one edge of the rectangular coil is simulated, and this is drawn as a cylindrical wire in Figure 4.3.

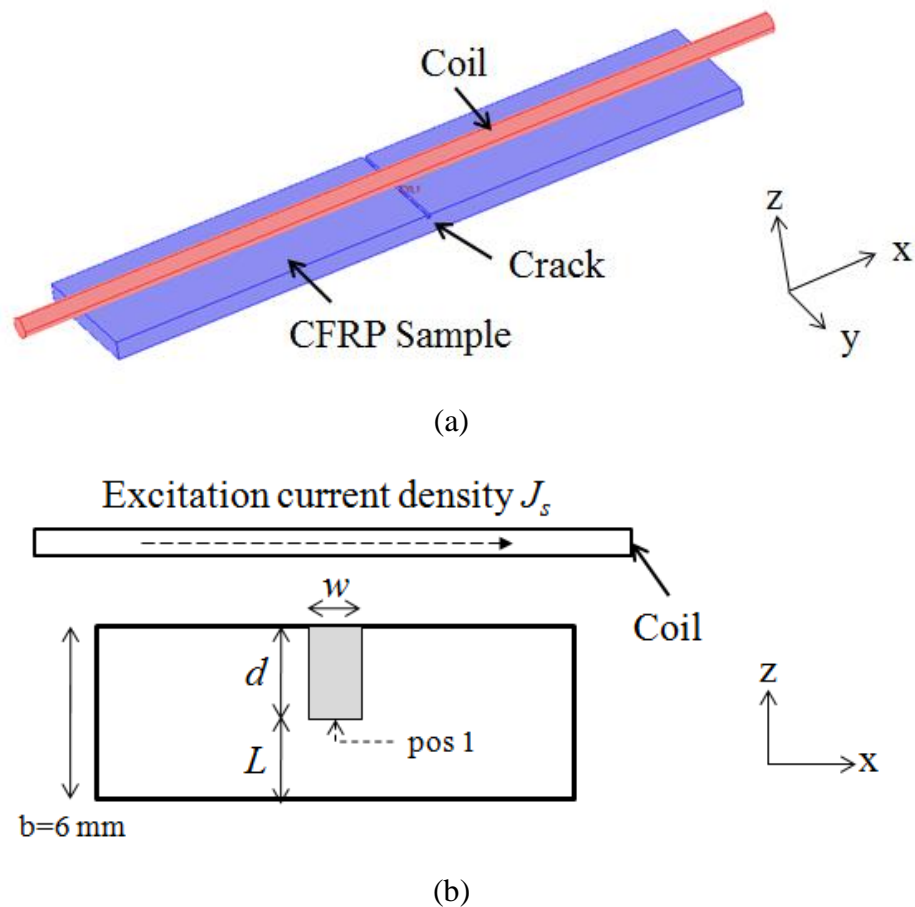


Figure 4.3 (a) 3D geometry setup of numerical model in COMSOL; (b) 2D side view of sample with crack

CFRP is an anisotropic material. And both the carbon fibre and the matrix, which is normally epoxy resin, contribute to its electrical and thermal properties. These vary in different directions due to the fibre orientation. The electrical conductivities in the longitudinal, transversal and cross-ply directions are set at  $10^4$ ,  $10^2$ , and  $10^2$  S/m [150], which can be also written as:

$$\underline{\underline{\sigma}} = \begin{bmatrix} 10^4 & 0 & 0 \\ 0 & 10^2 & 0 \\ 0 & 0 & 10^2 \end{bmatrix} \text{ S/m} \quad (4.1)$$

The thermal diffusivities of the CFRP as measured in the longitudinal, transversal and cross-ply directions are  $1.70\text{e-}6$ ,  $1.05\text{e-}6$ ,  $0.43\text{e-}6$   $\text{m}^2/\text{s}$  respectively at  $20^\circ\text{C}$  [151]. The density of CFRP is set at  $\rho=1540$   $\text{kg}/\text{m}^3$ . The specific heat is set at  $C_p=850$   $\text{J}/\text{kg}\cdot\text{K}$ . Then the thermal conductivity of CFRP in the longitudinal, transversal and cross-ply directions can be calculated, which can be expressed as:

$$\underline{\underline{k}} = \begin{bmatrix} 2.225 & 0 & 0 \\ 0 & 1.374 & 0 \\ 0 & 0 & 0.615 \end{bmatrix} \text{ W/mK} \quad (4.2)$$

#### 4.2.2.2 Numerical simulation results

##### (1) Influence of crack depth

Figure 4.4 shows the temperature distribution in the area around the crack at the maximum heating time of 200 ms. More heating is observed at the bottom of the crack due to the increased eddy current density in that area caused by eddy current diversion

around the bottom of the defect. The interaction between the crack and uniform eddy currents in the sample shows that the eddy currents will always follow the path of least resistance. Hence in a sample without a defect, they will be mainly confined to the surface layer, as defined by the skin depth formula along the sample thickness:

$$\delta = 1/\sqrt{f\sigma \pi} \quad (4.3)$$

where  $f$  is the excitation frequency,  $\sigma$  is the electrical conductivity, and  $\mu$  is the permeability of the material under inspection.

When a discontinuity such as a crack interrupts the path of eddy currents, they will be diverted around the bottom of the crack, which leads to an area of increased eddy current density and a resultant hot spot at the bottom of the crack. Schematic representation of eddy current behaviour around different types of defect has been also discussed in previous work by Newcastle University and the University of Bath [152].

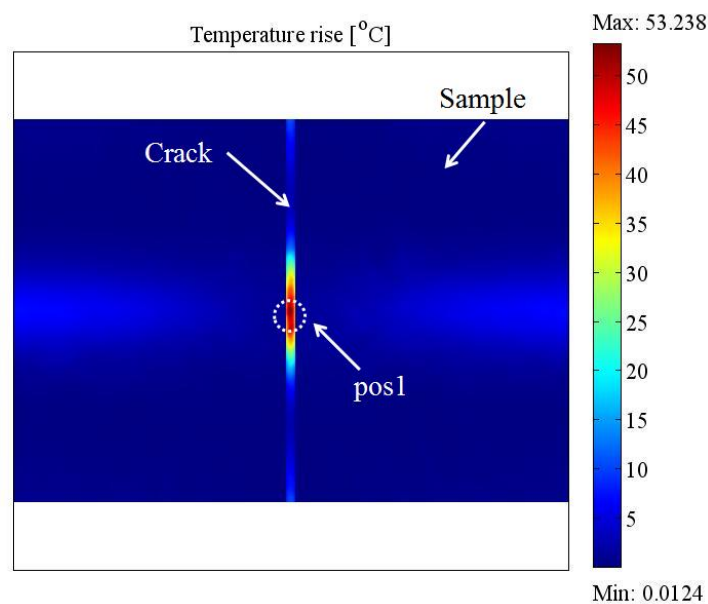
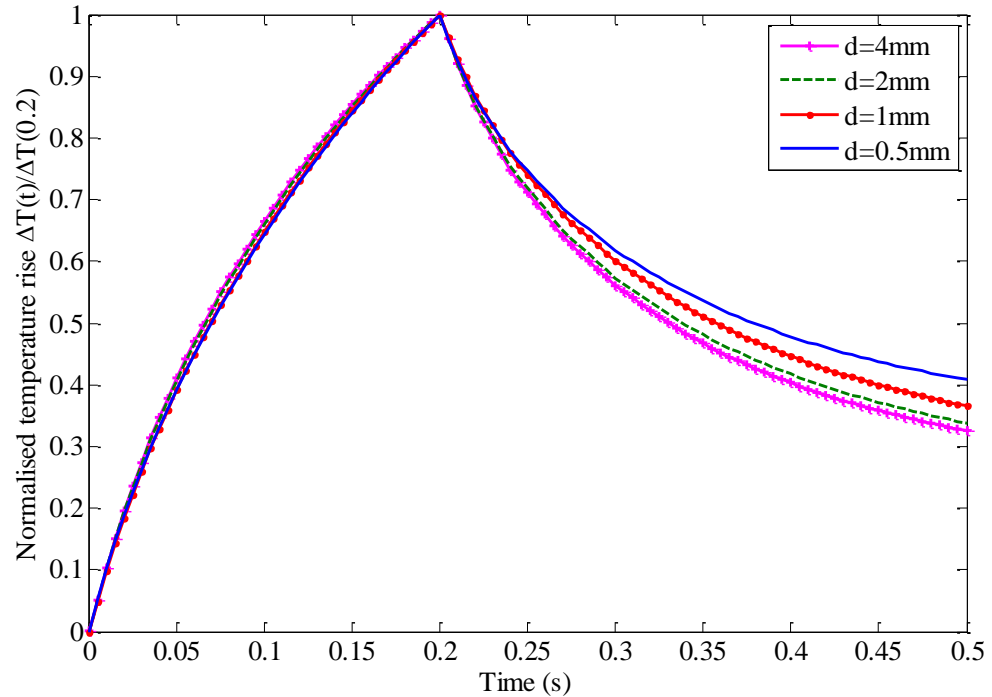


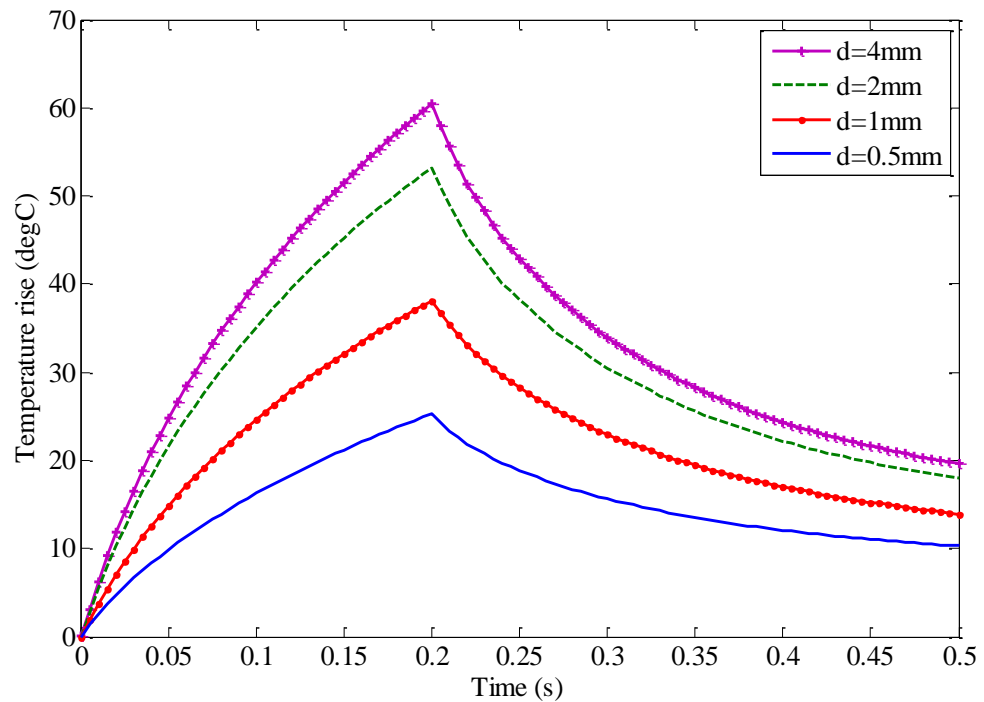
Figure 4.4 Simulation results of thermal images at the maximum heating (200 ms) for a crack with  $w=1$  mm and  $d= 2$  mm.

As the electric and thermal conductivity of CFRP vary in different directions, variations in the applied EM field orientation through changes in the excitation coil direction can be used for the investigation of different layers. Since conductivity is greatest in the fibre direction and fibres are orientated in different directions in different layers, changes in coil orientation will cause increased current flow in different layers. Besides this, the electric conductivity of CFRP is much smaller than that of metal. Therefore, the skin depth  $\delta$  at  $f = 256$  kHz from the governing equation (4.3) around 9.95 mm through the sample thickness is much larger than that of metal which is normally less than 0.1 mm for steel. For metallic materials, the skin depth is normally smaller than the crack depth, and at smaller skin depths the eddy currents tend to be concentrated at the surface but are much denser at the surface edge of the crack. Conversely, for CFRP, the skin depth is normally larger than crack depth. A large skin depth results in the eddy currents at the bottom of the crack being denser than those at the surface edge of the crack, because the crack blocks the surface current flows. Thus, the temperature rise at the bottom of the crack is higher than in the other regions in the CFRP sample, as shown in the simulation studies.

For cases where skin depth  $\delta$  is larger than sample thickness at the excitation frequency used in the simulation and experiments, a deeper crack causes a greater level of eddy current diversion at the bottom of the crack than in the case with a shallower crack. This effect is illustrated in the simulation results shown in Figure 4.5, where the temperature rise for the 4 mm deep crack is larger than that of the shallower crack. The point investigated in Figure 4.5 is marked as “pos1” in Figure 4.3b. These results agree with experimental results discussed in Section 4.2.3.



(a)



(b)

Figure 4.5 Simulation results for transient temperature against time at “pos 1” shown in Figure 4.3 at the crack bottom for varied crack depth at crack width  $w=1\text{mm}$ : (a) normalised responses; (b) non-normalised (raw) responses.

Derived from equations (3.14), (3.15) and (3.17) using Green's function in the solution for a finite body, the estimation of temperature against time for an infinite length and finite thickness of plate can be expressed with the following two equations: equation (4.3) for the heating phase [153]-[154] and equation (4.4) for the cooling phase [155]-[156]:

$$\Delta T(t) \approx \frac{1}{\sigma} |\bar{J}_{ec}|^2 \frac{2}{\rho C_p \sqrt{\pi \alpha_T}} \sqrt{t} = a \sqrt{\frac{t}{t_p}}, \text{ for } t < t_p \quad (4.3)$$

$$\Delta T(t) = \frac{Q}{\rho C_p L} \left\{ 1 + 2 \sum_{n=1}^{\infty} \exp\left[-\frac{n^2 \pi^2}{L^2} \alpha_T (t - t_p)\right] \right\} \approx \frac{1}{\sqrt{\tau(t - t_p)}}, \text{ for } t > t_p \quad (4.4)$$

where  $\alpha_T$  is the thermal diffusivity  $\alpha_T = k / \rho C_p$ ; and  $L$  is the distance from the evaluated point to the rear side of the sample. For a defect-free sample,  $L$  is the thickness of the sample; for a sample with a crack,  $L = b - d$  as shown in Figure 4.3b for the estimation in this study; and  $t_p$  is the duration of the heating pulse.

From equations (4.3) and (4.4), we can use coefficients  $a$  and  $\tau$  can be used to describe the thermal response. Coefficient  $a$  is the amplitude of temperature rise determined by the change in local electric conductivity (in this case, the eddy current density at the bottom of the crack), while  $\tau$  is the normalised temperature decay rate, which is determined by changes in local thermal properties and crack dimensions.

From Figure 4.5b, it can be seen that the deeper crack has a greater temperature rise (coefficient  $a$ ). The relationship between coefficient  $a$  and crack depth  $d$  is illustrated in Figure 4.6. This implies that a deeper crack will interact with and change the course of eddy currents to a greater degree. Therefore, a deeper crack leads to a larger temperature rise in the heating phase. However, after the normalisation of the transient temperature change with time for cracks of the same width and varied depths, a convergence of the transient temperature change is obtained for the heating phase, as shown in Figure 4.5a. This shows that crack depth does not affect normalised transient heating behaviour. As for coefficient  $\tau$ , it is clearer to investigate this after the normalisation of the temperature curve, as shown in Figure 4.5a. The results indicate the deeper crack has a faster



temperature decay in the cooling phase, as larger values of  $d$  (smaller  $L$ , where  $L=b-d$ ) results in larger  $\tau$  value, which matches equation (4.4). In conclusion, when the crack width is fixed, a deeper crack leads to a higher temperature rise in the heating phase at the bottom of the crack (coefficient  $a$ ) and faster temperature decay in the cooling phase (coefficient  $\tau$ ).

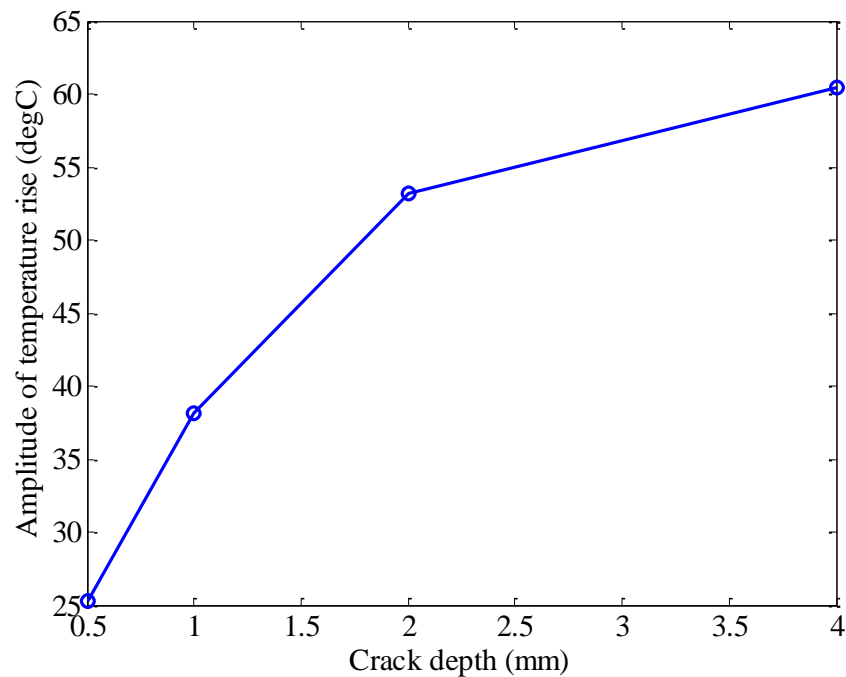
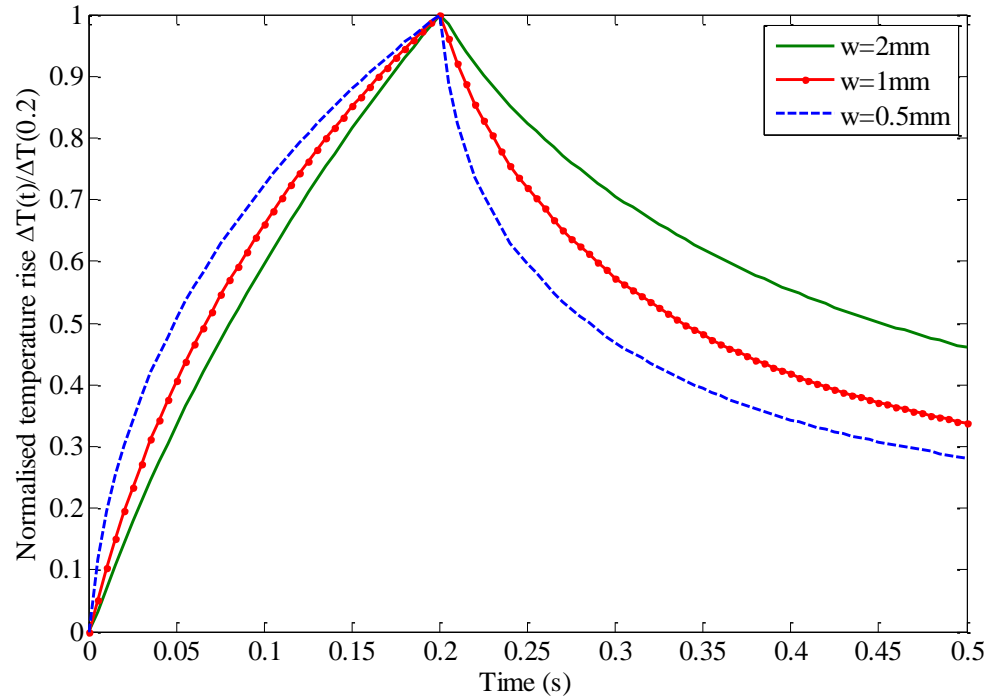


Figure 4.6 The amplitude of temperature rise ( $a$ ) versus crack depth  $d$ .

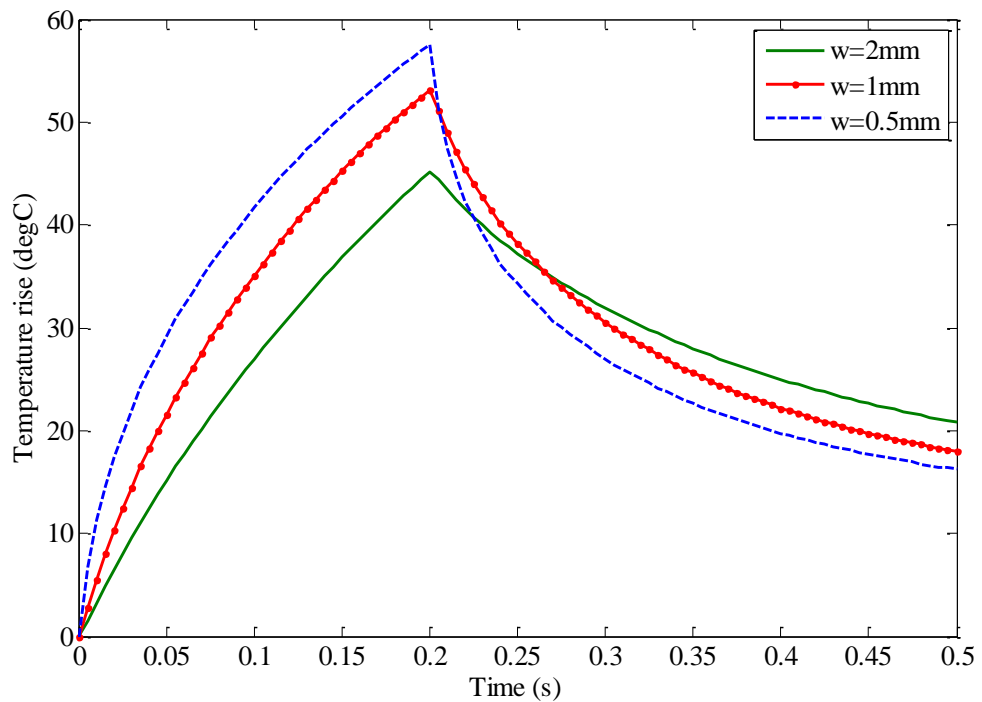
Although depth information can be derived from transient temperature changes with time in both the heating and cooling phases, the coefficients  $a$  and  $\tau$  can also be used for the investigation of crack width.

## (2) Influence of crack width

Since the simulation results presented in the previous section closely agree with the experimental results, therefore it is feasible to use simulation to predict the impact of crack width on thermal responses.



(a)



(b)

Figure 4.7 Simulation results for transient temperature against time at “pos 1” shown in Figure 1 at crack bottom for varied crack width at crack depth  $d = 2\text{ mm}$ : (a) normalised responses; (b) non-normalised (raw) responses.

The transient temperature changes against time for varied crack widths  $w$  are shown in Figure 4.7b, where it can be seen that the maximum amplitude of temperature change  $a$  increases as  $w$  becomes smaller. Unlike with the influence of crack depth, variation in crack width  $w$  not only changes the amplitude of the eddy current density, but also the eddy current distribution at the bottom of the crack due to the change in crack geometry. This implies that in a narrower crack, eddy currents are forced to be diverted around a narrower area at the crack bottom. Thus, a narrower crack leads to a greater temperature rise (as seen in Figure 4.7b), as well as a greater rate of change in temperature in the early stages of the heating phase (as seen in Figure 4.7a). As for the coefficient  $\tau$ , this is more clearly seen after the normalisation of the temperature curve shown in Figure 4.7a. The results also indicate that a narrower crack has a faster temperature decay in the cooling phase, as larger values of  $w$  result in smaller  $\tau$  values.

### ***4.2.3 Experimental study***

In section 4.2.2, numerical simulations investigating the influence of crack depth and width has been carried out. In the experimental study, the influence of crack depth on transient features is evaluated for comparison with and validation against the numerical results. Before the investigation of the influence of crack depth, directional excitation with respect to fibre orientation is firstly tested to maximise the heating of both the sample and the crack.

#### **4.2.3.1 Directional conductivity experiment**

As CFRP exhibits directional electrical and thermal conductivities dependent on the fibre orientation in the composite, coil orientation has a large impact on the experimental results. Thus, before inspecting the sample for defects, conductivity in the horizontal and vertical directions is first ascertained. This allows the optimisation of the direction of the applied field with respect to crack direction in order to achieve the best temperature contrast between regions with and without defects.

Two coil directions with respect to the sample surface, horizontal (Figure 4.8a) and vertical (Figure 4.8b), are investigated. For the horizontal coil orientation, the eddy

currents are induced in a horizontal direction, and hence the conductivity of the sample provided by Exel in the horizontal direction is investigated in this case. For the vertical coil direction, the conductivity of the sample in the vertical direction is investigated.

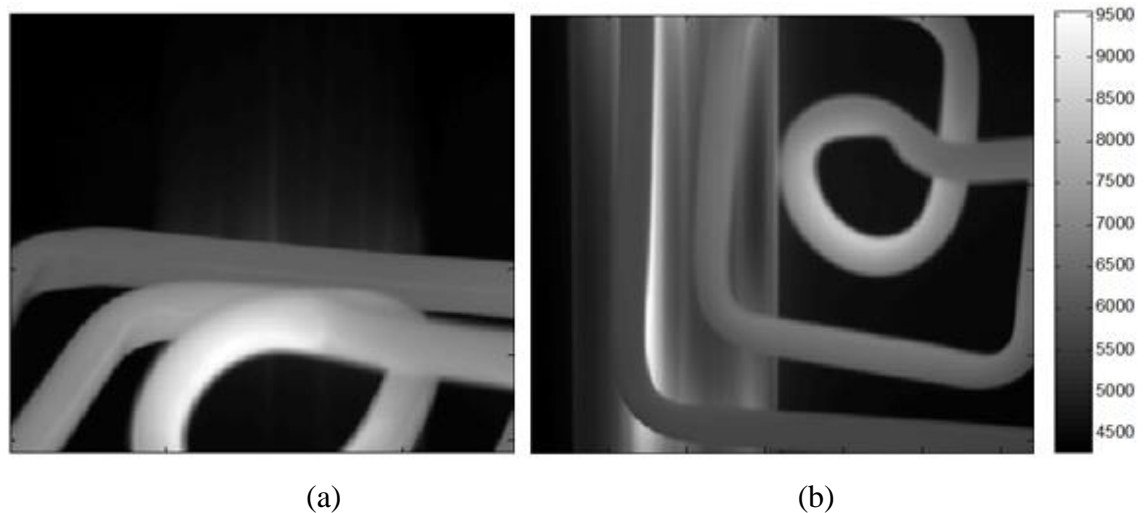


Figure 4.8 Thermal image of sample at maximum heating for: (a) horizontal current excitation; (b) vertical current excitation

Figure 4.8 shows the thermal image in terms of digital level (DL) after 2 seconds of heating using coil in horizontal and vertical directions respectively. As a reference, the temperature changes in the coil in Figure 4.8a and Figure 4.8b are similar. From the comparison of these two excitation directions, it can be seen that the increase in temperature at the sample surface with the coil orientated vertically is much larger than when the coil is orientated horizontally. According to equation (3.15), it can be concluded that the conductivity in the vertical direction is much larger than that in the horizontal direction. Thus, it can be ascertained the fibre orientation is in the vertical direction, as the conductivity is greater along the fibre orientation.

With awareness of the fibre orientation, the heating can be maximised when the coil direction is parallel to the fibre orientation. Therefore, the coil is fixed vertically in the following experiments.

#### 4.2.3.2 Influence of crack depth

The ECPT system used to inspect the sample is shown in Figure 3.3. The 350 mm × 38 mm × 6 mm CFRP sample contains three cracks each with a width of 1 mm, but varying in depth from 0.5 mm to 2 mm. The cracks are manufactured in the workshop at Newcastle University.

The sample was heated for 200 ms using the rectangular coil shown in Figure 3.4a. Images were acquired for a total of 500 ms (200 ms heating followed by 300 ms cooling) at the maximum frame rate of 383 Hz.

Cracks with different depths were inspected while retaining the same positional relationship between crack and coil. As an example, the thermal image at the maximum heating time for a 2 mm deep crack is shown in Figure 4.9.

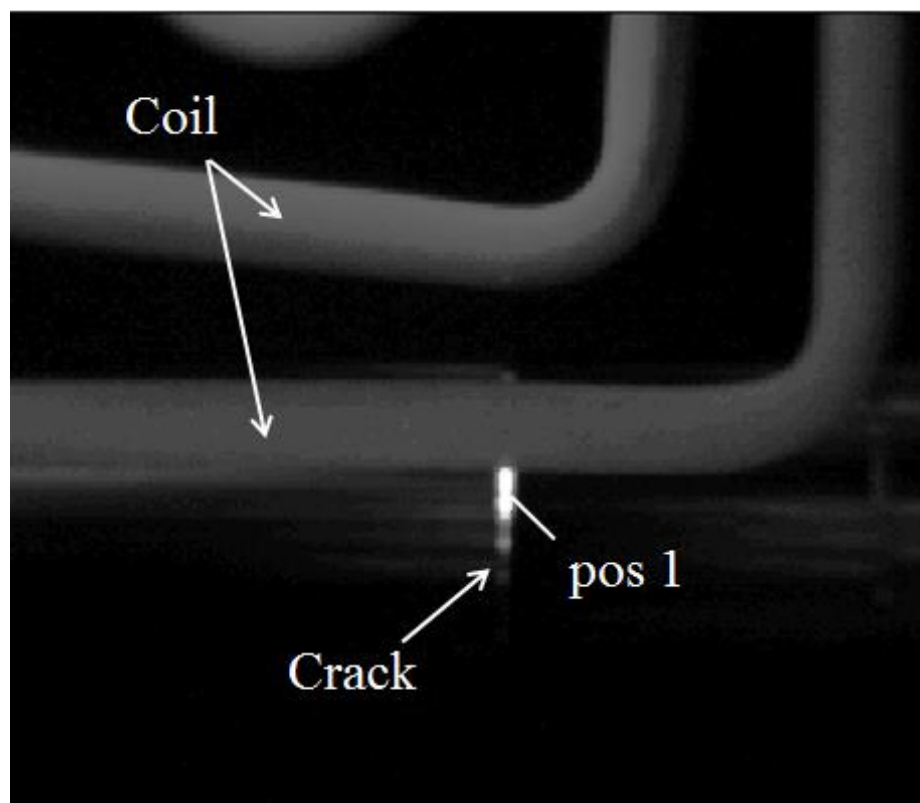
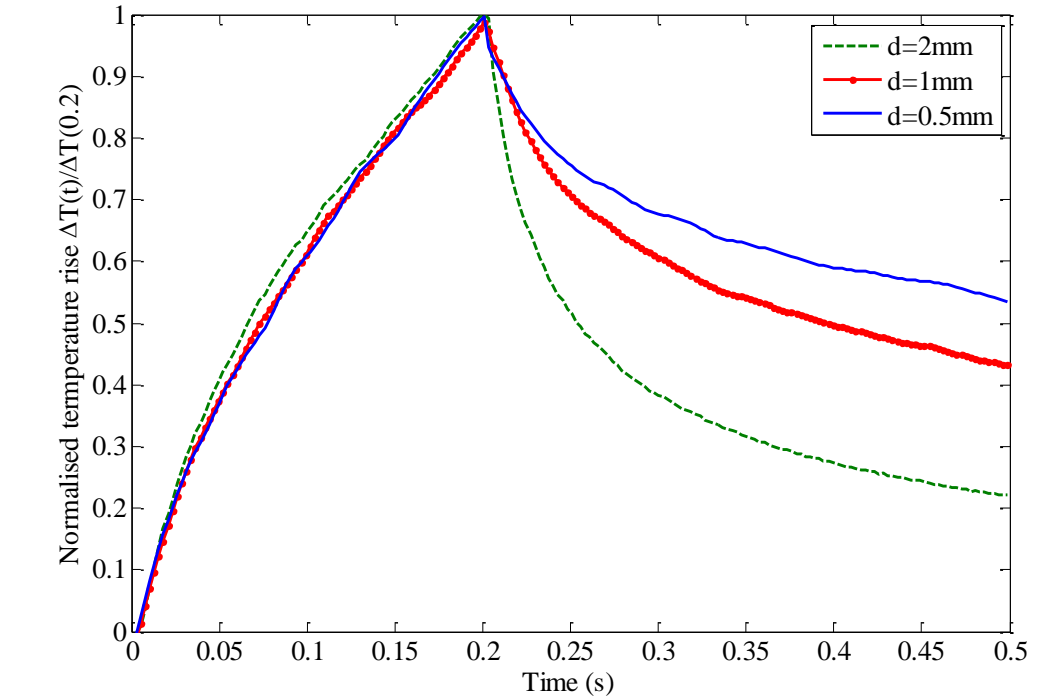
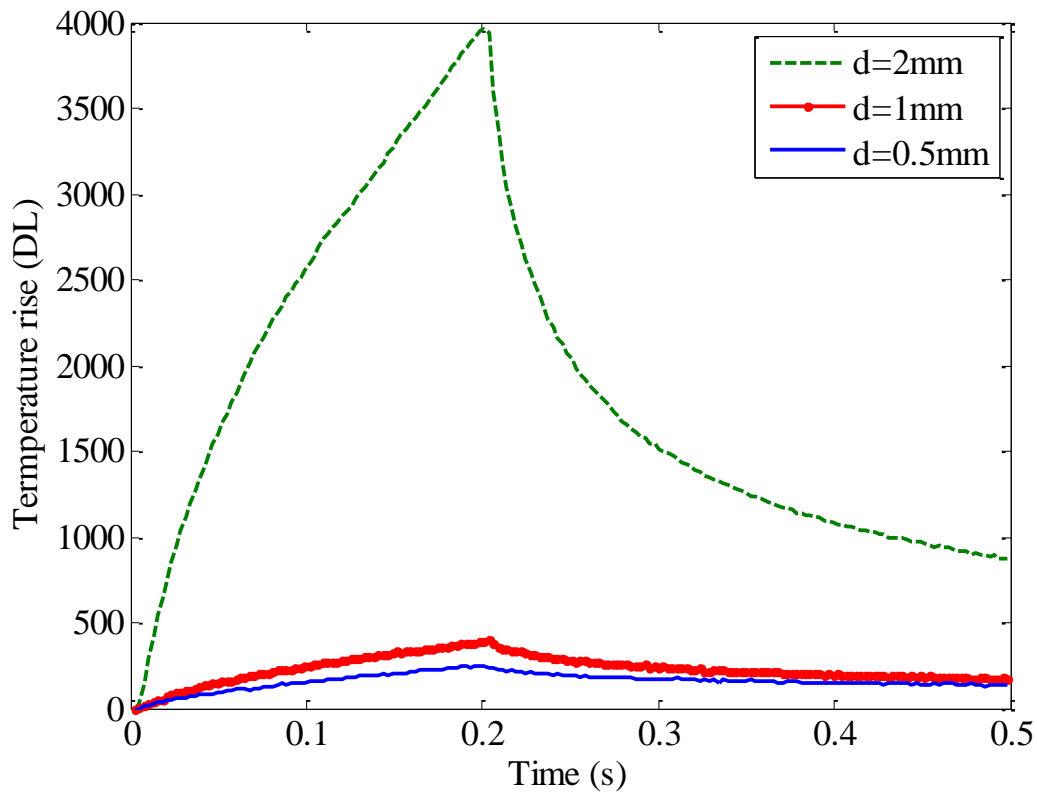


Figure 4.9 Experimental results of thermal image at the maximum heating (200ms) for 2mm deep and 1mm wide crack.

The transient temperature change at the same point at the bottom of the crack and close to the coil, marked as “pos 1” in Figure 4.9, is investigated. The thermal responses for varied crack depths are shown in Figure 4.10. In Figure 4.10, the unit for temperature is called digital level, where the higher value of digital level indicates the higher temperature. From a comparison of the thermal responses at the investigated point for the three cracks shown in Figure 4.10, it can be ascertained that the deeper the crack, the greater the increase in temperature. This is because the eddy currents are concentrated at the bottom of the crack when crack depth is smaller than skin depth. The relationship between crack depth and transient temperature change from the experimental results agrees with those from the simulation illustrated in Figure 4.5a and Figure 4.5b. From Figure 4.10, it can be seen that the amplitude of the temperature rise, coefficient  $a$ , for a 2 mm deep crack is the largest due to the highest eddy current density at the bottom of this crack. From the comparison of  $\tau$  from the normalised transient temperature behaviour shown in Figure 4.10, it is clear that the temperature decay rate for the 2 mm deep crack is the largest. Because  $L$  in equation (4.4) for a 2 mm deep crack is the smallest ( $L=b-d$ ), the  $\tau$  value for this crack is the smallest among the three cracks. Therefore, the coefficients  $a$  and  $\tau$  can be used to discriminate between cracks of different depths.



(a)



(b)

Figure 4.10 Experimental results for transient temperature change against time at “pos 1” as shown in Figure 4.9 at crack bottom for cracks with  $w = 1\text{ mm}$  and varied depths: (a) normalised responses; (b) non-normalised (raw) responses.

#### **4.2.4 Discussion**

Directional electrical and thermal conductivities make the eddy current distribution in CFRP different from that of metallic materials. The surface crack was detected and observed using ECPT through both simulation and experiment. It has been proven that the ECPT technique is feasible for the detection of surface defects in composite materials with low conductivity in the scale of  $10^4$  S/m. Through the simulation and experimental results shown in Figure 4.5 and Figure 4.10 respectively, it can be seen that the heat is mainly generated at the crack.

The influence of crack depth and width are investigated in terms of the amplitude of the temperature rise and transient temperature behaviour in the heating and cooling phases respectively. The following conclusions can be drawn:

- Crack depth: the relationship between crack depth and transient temperature change shows that in a deeper crack, a greater temperature rise occurs at the bottom of the crack. In a deeper crack, the normalised temperature decay rate is faster in the cooling phase, but the normalised transient temperature behaviour in the heating phase is not affected.
- Crack width: The results show that in narrower cracks there is not only a greater temperature rise, but also the faster temperature increase and decay rate at the beginning of the heating phase and in the cooling phase respectively.

Thus, based on the amplitude of the temperature rise, the heating and cooling thermal response, the crack width and depth can be determined by feature extraction and QNDE. In addition, the temperature contrast between defective and defect-free regions is very apparent, which makes pixel selection relatively easy in cases of cracks. In contrast, pixel selection is harder in the next case study. It can also be noticed that QNDE remains rather inaccurate when the pixel is hard to select and the fibre texture is complex.

#### **4.3 Case study 2: impact damage detection and characterisation**

Impact damage is more complex than cracks in terms of the defect and fibre texture. Impact damage changes the material properties and structure not only at the surface but also inside the sample. In addition, woven fibre is used in this case study, which is the



most complex fibre texture of all samples used in this thesis. In this section, the local variation in electric and thermal conductivities caused by an impact is quantified through the analysis of features at pixel level. Then the relationship between variation in conductivities and impact energy is investigated.

### 4.3.1 Sample description

CFRP plates as shown in Figure 4.11a have 12 layers of 5HS carbon fibre woven, as shown in Figure 4.11b, with a quasi-anisotropic global distribution, which are named as sample “Set 3” in TABLE 3-I. The polymer matrix is made of polyphenylene sulphide (PPS). The size of the plate is 100 mm × 150 mm with a  $0.5 \pm 0.03$  volume ratio and  $1460 \text{ kg/m}^3$  density. The plates are produced by TenCate Advanced Composites, Netherlands, and provided by Prof. Raimond Grimberg from the National Institute of Research and Development for Technical Physics, Romania.

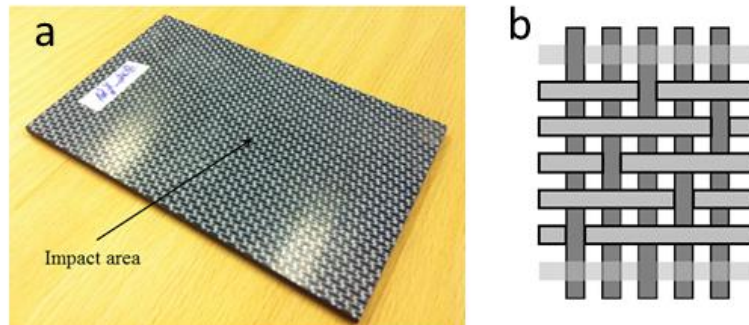


Figure 4.11 (a) a photograph of impacted sample; (b) scheme of 5HS carbon fibre woven.

Table 4-I Description of impacted samples

No	Height (m)	Energy (J)	Thickness (mm)
1	0.2	4	3.785
2	0.3	6	3.784
3	0.4	8	3.741
4	0.5	10	3.745
5	0.6	12	3.782

The impact damage is manufactured in the middle of the sample with different levels of impact energy. The impacts were generated using CEAST FractovisPlus 9350 impaction equipment with a data acquisition system DAS 16000 and analysis software Visual IMPACT. The impactor is hemi-spherical, 22.2 mm in diameter and 2.042 kg in weight. The impacts were realized in the conditions specified by ASTM D7136 at a temperature of  $20 \pm 1$  °C. The thickness of the plate and impact energy are summarised in Table 4-I. Impact damage with amounts of energy results in a concave area on the surface of the specimen, conversely, impacts with large energy lead to a concave and some level of protrusion on the edge of the concavity.

### 4.3.2 Numerical simulation results

#### 4.3.2.1 Numerical models and parameter set-up

In this work, CFRP samples of dimensions 150 mm × 100 mm × 4 mm are used. The excitation frequency and current are 256 kHz and 380 A<sub>rms</sub> respectively to match the experimental set-up. A rectangular coil is used in both numerical simulation and the experiment. However, the eddy currents are induced predominantly by the coil edge that is closest to the sample. Thus, only one edge of the rectangular coil is simulated as a cylindrical wire as shown in Figure 4.12.

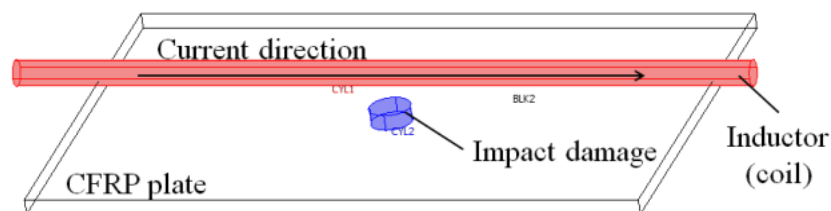


Figure 4.12 Geometry of sample and impact damage, marked in blue.

By simplifying the results published by Wicks [157] and Hou [158], a cylinder marked in blue in Figure 4.12 is used to describe impact areas with variations in electrical and thermal conductivities. The electrical conductivities within the cylinder in the  $x$ ,  $y$ ,  $z$  directions can be expressed as:

$$\sigma_x = \sigma_{x0} \left[ 1 - (1 - a_x) \cos\left(\frac{\pi x}{2\sqrt{r^2 - y^2}}\right) \right] \quad (4.5)$$

$$\sigma_y = \sigma_{y0} \left[ 1 - (1 - a_y) \cos\left(\frac{\pi x}{2\sqrt{r^2 - y^2}}\right) \right] \quad (4.6)$$

$$\sigma_z = a_z \sigma_{z0} \quad (4.7)$$

where  $a_x$ ,  $a_y$ ,  $a_z$  are the maximum variation rates of electrical conductivity in the  $x$ ,  $y$ ,  $z$  directions respectively;  $r$  is the radius of impact damage (blue cylinder);  $\sigma_{x0}$ ,  $\sigma_{y0}$ ,  $\sigma_{z0}$  are the electrical conductivities without impact (outside the blue cylinder); and  $x$  and  $y$  are coordinates assuming that the centre of blue cylinder is  $x=0$ ,  $y=0$ .

The thermal conductivity distribution is defined using the same expressions as those for electrical conductivity but with the coefficients  $b_x$ ,  $b_y$ ,  $b_z$  to replacing  $a_x$ ,  $a_y$ ,  $a_z$  and substituting  $\sigma_{x0}$ ,  $\sigma_{y0}$ ,  $\sigma_{z0}$  with  $k_{x0}$ ,  $k_{y0}$ ,  $k_{z0}$ .

Table 4-II shows the simulated electrical/thermal conductivity variations within the impact damage area (in seven simulations, numbered as S0-S6). It is assumed that electrical and thermal conductivities outside the impact area are not changed.

The electrical and thermal conductivities are defined as the same as those presented in Section 4.2.2.1. The electrical conductivities  $\sigma_{x0}$ ,  $\sigma_{y0}$ ,  $\sigma_{z0}$  are set at  $10^4$ ,  $10^2$ , and  $10^2$  S/m respectively, while the thermal conductivities  $k_{x0}$ ,  $k_{y0}$ ,  $k_{z0}$  are set at 2.225, 1.374, 0.615 W/(mK) respectively at 20°C. Due to limitations of computer performance, the complex fibre texture is simplified so that a uni-directional fibre structure is used for the numerical simulation. When the woven fibre is simulated in COMSOL, the computer runs out of memory (8Gb memory) due to the massive increase in number of element,

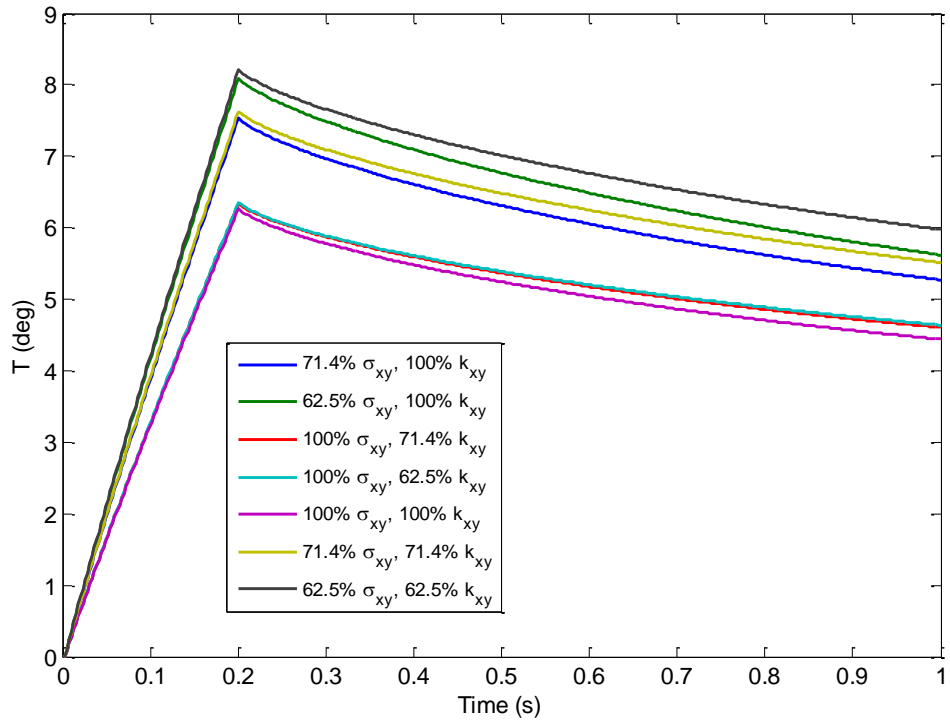
which need to be calculated. In other words, the numerical model becomes inaccurate using a commercial computer when fibre texture is not uni-directional, as shown in Section 4.2. Despite this, the trends shown by features against variations in physical properties can still be investigated through numerical simulation.

Table 4-II Electrical and thermal conductivities settings for simulation

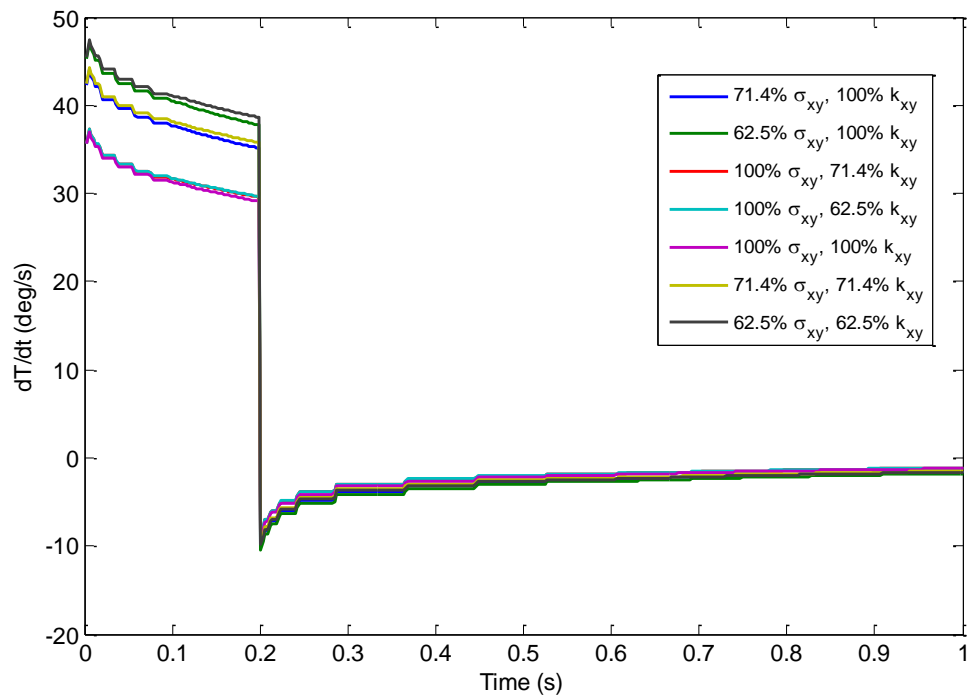
Sim.	$\sigma_x/\sigma_{x0}(\%)$	$\sigma_y/\sigma_{y0}(\%)$	$\sigma_z/\sigma_{z0}(\%)$	$k_x/k_{x0}(\%)$	$k_y/k_{y0}(\%)$	$k_z/k_{z0}(\%)$
S0	100	100	100	100	100	100
S1	71.4	71.4	90.9	100	100	100
S2	62.5	62.5	90.9	100	100	100
S3	100	100	100	71.4	71.4	90.9
S4	100	100	100	62.5	62.5	90.9
S5	71.4	71.4	90.9	71.4	71.4	90.9
S6	62.5	62.5	90.9	62.5	62.5	90.9

#### 4.3.2.2 Numerical simulation results

A 200 ms heating time followed by 800 ms cooling time is simulated. To investigate transient thermal behaviour, the temperature  $T-t$  and the first derivative of temperature against time  $dT/dt-t$  for different  $\sigma-k$  values at the central point in the impact area, are plotted in Figure 4.13.



(a)



(b)

Figure 4.13 (a) Transient temperature and (b) first derivatives at the origin  $(x, y, z) = (0, 0, 0)$ .

From Figure 4.13, it can be seen that in the heating phase the same value of  $\sigma_{xy}$  leads to the same increase in thermal response and different values of  $\sigma_{xy}$  results in different rates of temperature increase, which can be seen clearly in the first derivative of temperature response  $dT/dt$  (100, 71.4 and 62.5 %  $\sigma_{xy}$ ). However, when  $\sigma_{xy}$  stays constant, the variation in  $k_{xy}$  has an insignificant influence on  $dT/dt$ . From equation (3.17), the temperature distribution is even at the beginning of the heating phase on the sample surface. Thus,  $\nabla \cdot (k\nabla T) = 0$  at  $t=0_+$  s and the major contribution to temperature rise is the  $\rho C_p \partial T / \partial t$  part on the left hand side of equation (3.17). Therefore, equation (3.17) can be simplified at the beginning of the heating phase to be:

$$\frac{\partial T}{\partial t} = \frac{1}{\rho C_p} Q, \text{ for } t=0_+ \quad (4.8)$$

As a result, a linear increase in temperature can be observed at the beginning of the heating phase and the rate of temperature rise  $\partial T / \partial t$  mainly depends on  $Q$ , determined by  $\sigma$ . When the electrical conductivity of the impact area decreases, the eddy current density is increased in that area which is caused by the diversion of the eddy currents around the area of low electrical conductivity (*i.e.* impact area). This diversion results in an increase in  $Q$ , so the rate of temperature increase  $\partial T / \partial t$  rises as  $\sigma$  decreases.

In the cooling phase, a larger  $k_{xy}$  leads to a faster rate of decrease, which can be seen in the transient temperature response as illustrated in Figure 4.13a. From equation (3.17),  $Q$  is 0 in the cooling phase. Therefore the equation (3.17) can be rewritten and simplified as:

$$\frac{\partial T}{\partial t} = \nabla \cdot \left( \frac{k}{\rho C_p} \nabla T \right) \quad (4.9)$$

Because the point of the highest temperature is investigated in Figure 4.13,  $\nabla \cdot (k\nabla T)$  is negative. This equation can explain that a larger value of  $k$  results in a smaller  $dT/dt$  value, which also means a faster rate of temperature decrease in the cooling phase.

To conclude, numerical simulations of CFRP materials show that  $\sigma_{xy}$  dominates the temperature response in the heating phase and  $k_{xy}$  dominates the temperature response in the cooling phase, which enables the separation of  $\sigma_{xy}$  and  $k_{xy}$ . In addition, a decrease on  $\sigma_{xy}$  leads to a faster temperature rise in the heating phase, whilst a larger decrease in  $k_{xy}$  leads to a slower temperature decrease in the cooling phase, which can be seen in Figure 4.14.

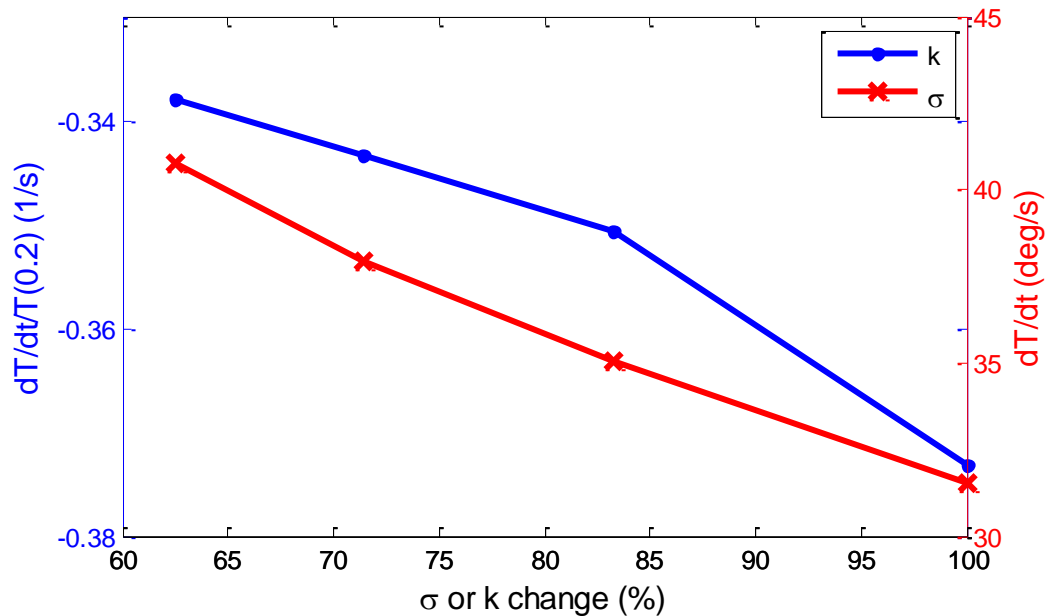


Figure 4.14  $dT/dt$  against variation in electrical conductivity at  $t=0.1$  s (red line with crosses); and  $(dT/dt)/T(0.2)$  averaging from 0.2s to 1s against variation in thermal conductivity (blue line with dots).

### 4.3.3 Experimental results

A 200 ms heating time followed by 800 ms cooling time is applied at the maximum data acquisition frame rate of 383 Hz. Reflection mode is used in this case study. The thermal image at 200 ms for 8J-sample is shown in Figure 4.15 as an example.

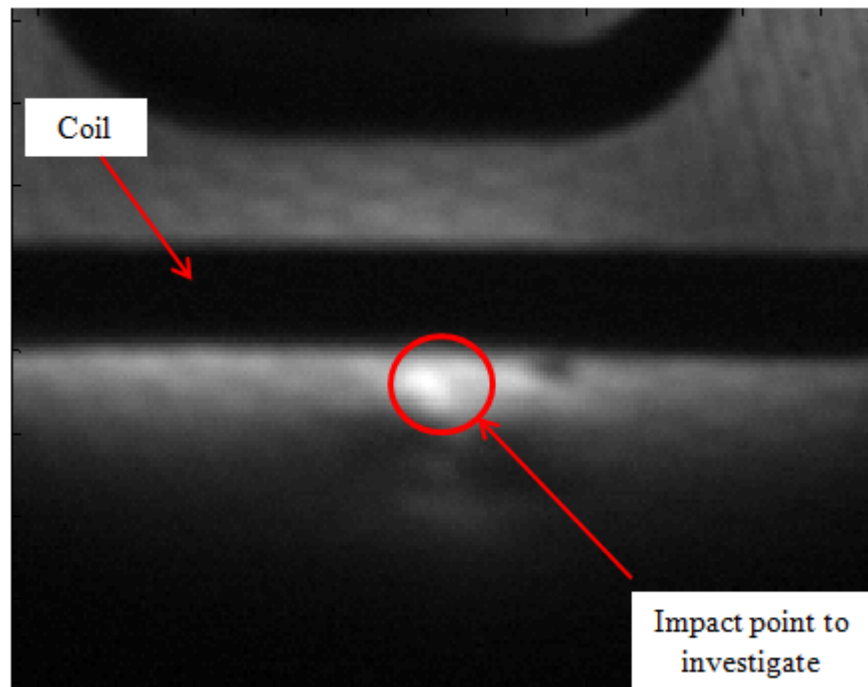
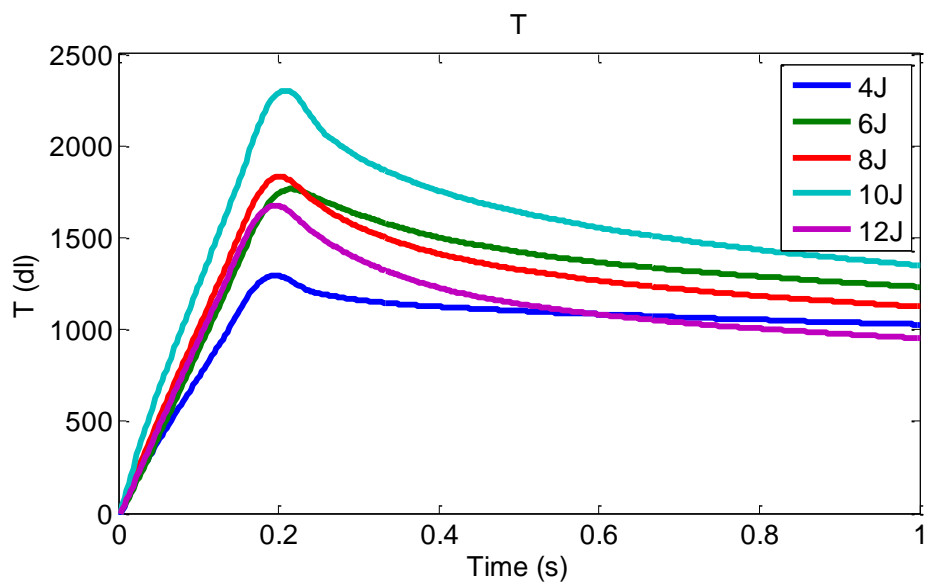


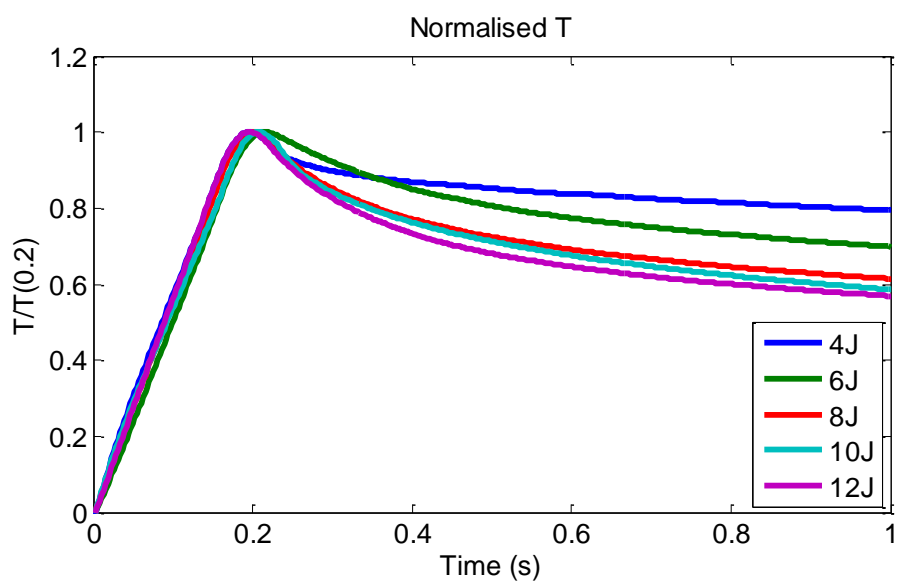
Figure 4.15 Thermal image of the sample with 8J impact at 0.2s showing the point investigated.

From Figure 4.16a and Figure 4.16c, it can be seen that the order of the rate of temperature increase is  $10J > 8J > 6J > 12J > 4J$ , where it is known that the comparative electrical conductivities are  $\sigma_{10J} < \sigma_{8J} < \sigma_{6J} < \sigma_{12J} < \sigma_{4J}$ . From Figure 4.16b, the order of the rate of temperature decrease at different impact energies is  $12J > 10J > 8J > 6J > 4J$ , so that the thermal conductivities are  $k_{12J} > k_{10J} > k_{8J} > k_{6J} > k_{4J}$ . From the experimental results, it can be seen that the electrical conductivity decreases and the thermal conductivity increase when the impact energy becomes larger, except at 12J.

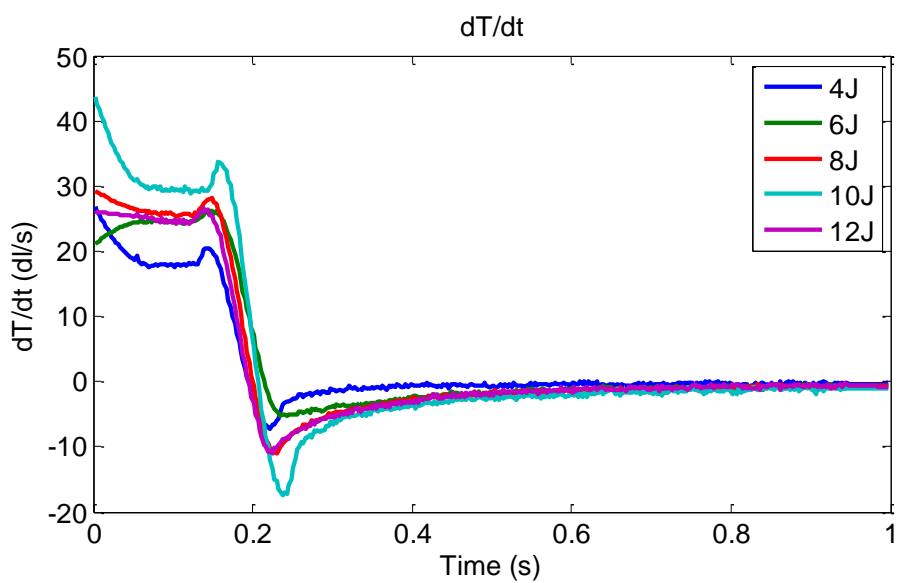




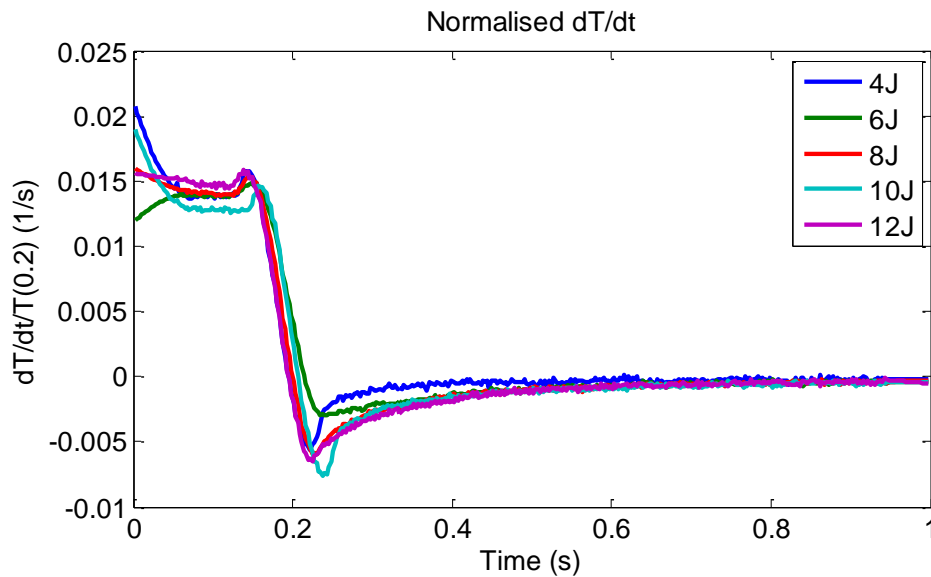
(a)



(b)



(c)



(d)

Figure 4.16 Transient temperature at impact point against time: (a) non-normalised response; (b) normalised response and 1<sup>st</sup> derivatives of temperature; (c) non-normalised response; (d) normalised response.

From the simulation results discussed in Section 4.3.2.2, it is known that the electrical conductivity dominates the  $dT/dt$  in the heating phase while thermal conductivity dominates  $(dT/dt)/T(0.2)$  in the cooling phase. Therefore, the average values of  $dT/dt$  in Figure 4.16c from 0.07s to 0.12s are calculated in order to investigate the relationship between electrical conductivity and impact energy. Also rates of the temperature decrease from Figure 4.16b are calculated to investigate the relationship between thermal conductivity and impact energy. The relationship between impact energy and  $dT/dt$  in the heating and cooling phases is shown in Figure 4.17. According to the simulation results shown in Figure 4.14, it can be found that the electrical conductivity decreases when impact energy increases, except at 12J; whereas thermal conductivity increases as the impact energy increases.

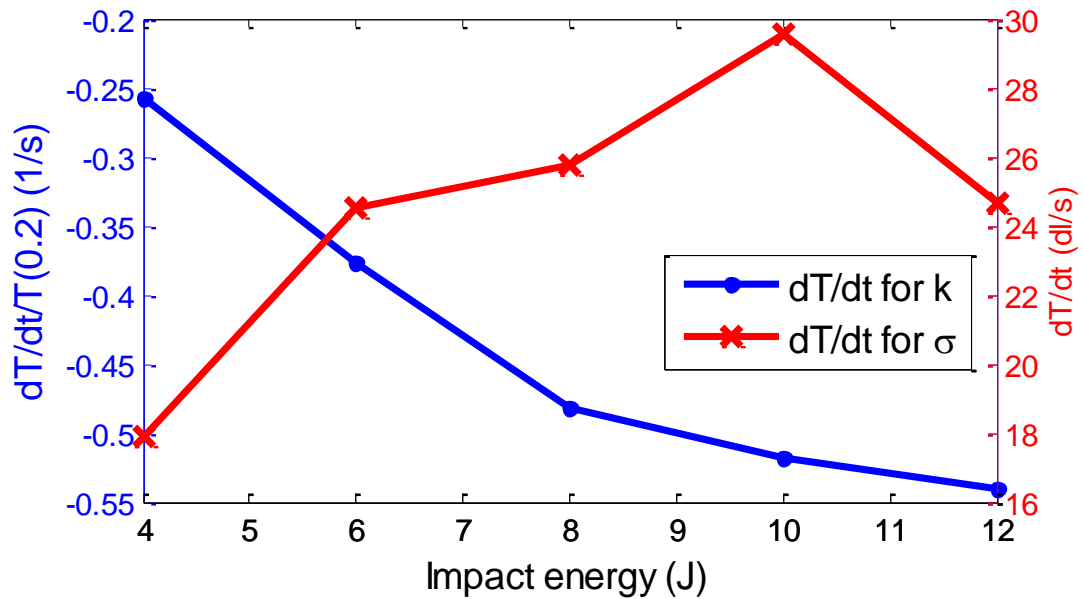


Figure 4.17 Impact energy against average  $dT/dt$ , which stands for variation in electrical conductivity (red line with crosses); and against  $(dT/dt)/T(0.2)$  which stands for variation in thermal conductivity (blue line with dots).

For the 12J-impacted sample, cracks on the front surface are produced as shown in Figure 4.18. For other samples, no surface cracks are produced by the impact. The production of the crack releases the residual stress within 12J-impacted samples, which influences the electrical conductivity distribution. This explains the abnormal response in the heating phase of the 12J-impacted sample compared to other samples. When the level of impact energy is not sufficient to produce a surface crack, the electrical conductivity in the impact area decreases, but thermal conductivity increases.

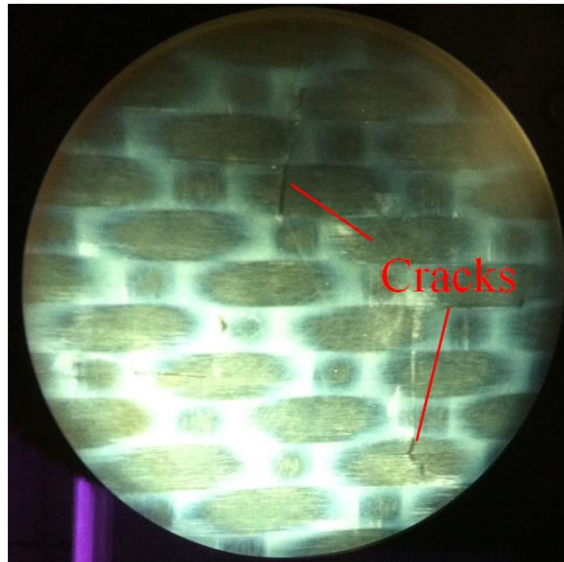


Figure 4.18 Picture under microscope of impact area in 12J sample.

#### 4.3.4 Discussion

From the numerical simulation, it was found that firstly  $\sigma_{xy}$  and  $k_{xy}$  respectively determine the temperature response in heating and cooling phases, which enabled the separation of  $\sigma_{xy}$  and  $k_{xy}$  by using  $dT/dt$  in the heating and cooling phases as two features. Secondly, the larger decrease in  $\sigma_{xy}$  leads to a faster temperature rise in the heating phase while a larger decrease in  $k_{xy}$  leads to a slower temperature decrease in the cooling phase. The simulation results provide a basis for experimental results to evaluate  $\sigma$  and  $k$  variation via features extracted from transient thermal responses at various impact energies. In addition, the fibre texture is simplified and considered to be uni-directional in the numerical modelling in order to ensure that the computer memory is sufficient to perform the simulation. This, however, introduces uncertainty into the simulation results as a trade-off.

In the experimental studies, impacts energies from 4J to 12J were applied to the CFRP samples. From the thermal images, it can be seen that the pixel selection becomes harder compared with cracked samples. The temperature contrast between defective and defect-free regions is not as obvious as in the case for cracks, because the electrical and thermal conductivity at the impact increase or decrease by relatively small percentages rather than dropping to zero as in cases of cracks.

From the analysis of the transient responses  $t-T$  and the first derivative of temperature against time  $t-dT/dt$ , it was found that as the impact energy increases, the electrical conductivity in the impact area decreases but the thermal conductivity increases. But this trend works when the impact is not enough to produce a surface crack. When a surface crack is produced, the combination of the effect of the surface crack and impact damage on the thermal image increases the inaccuracy of the determination of the variations in physical properties. Besides this, the complexity of fibre texture can also affect the thermal image, which also increases the difficulty of pixel selection to show the variation in the physical properties.

Comparison of results of the two case studies in Sections 4.2 and 4.3 shows that the ECPT investigation at pixel level achieves good QNDE results for cracks (surface defects) in simple fibre textures such as uni-directional fibre. However, it is not accurate due to the difficulty of pixel selection, when the fibre texture becomes complex and/or the defect is not on the surface of the sample.

#### **4.4 Defect classification using ECPT investigation at pixel level**

As listed in TABLE 3-I, three types of defects are used in this thesis. Transient temperature responses can be obtained from individual samples. To classify the defects, the PCA on transient temperature responses in local regions, either at specific pixel or averaging over a small area, is implemented in this section.

The frame rates of the thermal videos, the durations of heating and the thermal cameras used in the investigation of the delamination all differ from those used for the other two defects. The transient temperature responses of cracks in sample Set 1, and impact damage on the front side and delamination observed on the rear side of impacted sample Set 2 are used for PCA classification. Each transient response  $T-t$  is seen as a vector variable. In total, 11 vector variables from 11 measurements form the input matrix. After implementing the PCA algorithm on the matrix, the first two weighted PCs are selected to classify the defects.

The thermal images and typical points for transient temperature response (temperature versus time), including those for three measurements for a crack, four for impact damage and two for delamination, are shown on the left in Figure 4.19. The first two

PCs (PC1 and PC2)) are selected and shown on the right hand side. It can be seen that there is no overlap in plot of the first two PCs amongst the three types of defects and four types of pixel selection. Due to the differences in transient responses, cracks can be distinguished from other defects since PC1 and PC2 are all negative, are marked as green dots in the PC plot on the right hand side of Figure 4.19. In addition, PC1 and PC2 values increase as the depth of the cracks increases. Red squares denote the impact damage, which lies in the middle of PC1 axis between those for delamination edge and crack. Delamination, marked as purple squares, has a similar PC1 value compared to delamination edge, which is marked as blue triangles; but served as smaller PC2 values. From this, it can be seen that the crack can be classified using PCA on the transient responses at the pixel level.

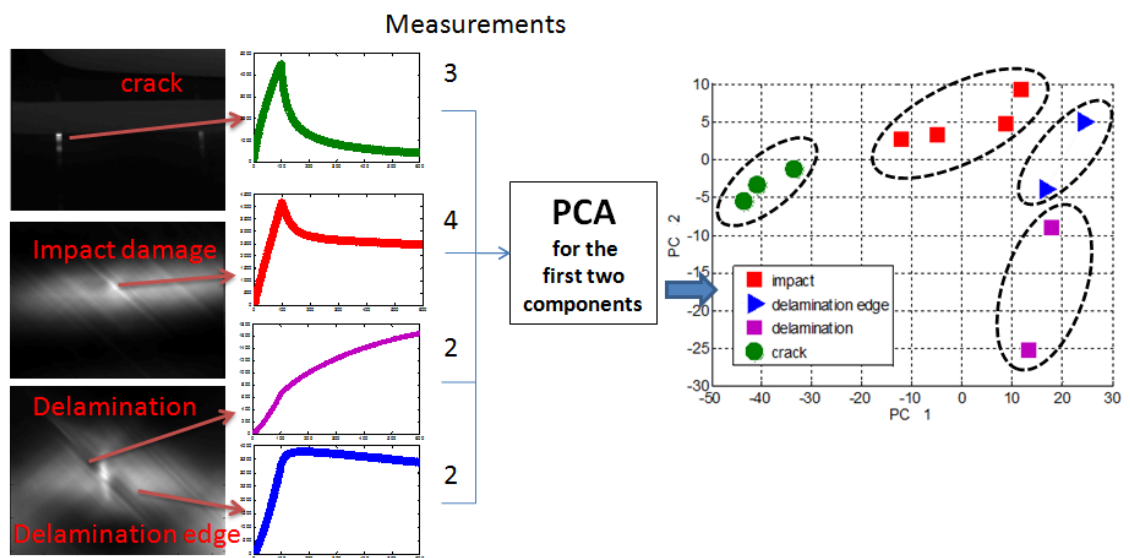


Figure 4.19 PCA classification for cracks, impact damages and delaminations at the pixel level.

However, the pixels are selected specifically for regions with the largest temperature increase, and this may lead to large variations when surrounding pixels are selected or more samples are tested. To overcome this problem, an optical flow algorithm at the local area level was implemented to classify the defect using investigation over a relatively larger area. This is described in the next chapter.

## 4.5 Chapter summary

In this chapter, the ECPT investigation at pixel level has been reported, including the capture of transient thermal responses and the relevant feature extraction from the raw thermal video/image sequences, quantitative information about defect dimensions and variations in physical property in defective regions, and the classification of defects by analysing the transient temperature responses using PCA algorithm.

From the case study of cracks, the relationship between crack depth and transient temperature change was determined. It was shown that a deeper crack leads to a greater temperature rise at the bottom of the crack. A deeper crack also results in a faster normalised temperature decay rate in the cooling phase, whereas the normalised transient temperature behaviour in the heating phase is not affected. The results also show that narrower cracks are associated with not only a greater temperature rise, but also faster temperature rise and decay rates at the beginning of the heating phase and in the cooling phase respectively.

From the case study of impact damages, three conclusions can be drawn. Firstly,  $\sigma_{xy}$  and  $k_{xy}$  determine the temperature response in the heating and cooling phases respectively, which enabled the separation of  $\sigma_{xy}$  and  $k_{xy}$  by using  $dT/dt$  in the heating and cooling phases as two features; Secondly, a larger decrease in  $\sigma_{xy}$  leads to a more rapid temperature increase in the heating phase, whilst a larger decrease in  $k_{xy}$  leads to slower temperature decreases in the cooling phase. Thirdly, as impact energy increases when it is not enough to produce a surface crack, the electrical conductivity in the impact area decreases but thermal conductivity increases.

Through the analysis of data from crack, delamination and impact damage using PCA, the first two weighted PCs of transient temperature responses were calculated. Results showed that the crack can be distinguished from the transient responses at the pixel level.

Comparison of these two case studies shows the advantages and disadvantage of the ECPT investigation at the pixel level. Firstly, it achieves good QNDE results for cracks as surface defects when the fibre texture is simple as in uni-directional fibre and the hot-spots are clear for pixel selection. However, it is not accurate when the fibre texture becomes complex and/or the defect is not on the surface of the sample. This is because

the heat diffuses from inside the sample, leading to difficulties in selecting pixels. To overcome the drawbacks of the ECPT investigation at the pixel level for interior defects even in complex fibre textures, the investigations at the local area and pattern levels are presented in the following two chapters, respectively.



## Chapter 5. ECPT INVESTIGATION AT THE LOCAL AREA LEVEL

As discussed in Chapter 4, the ECPT investigation at pixel level gives good results for defect evaluation and quantification in simple fibre textures and surface defects. However, it is not accurate due to difficulties on pixel selection when the fibre texture becomes more complex and/or if the defect is not on the surface of the sample. To achieve better results for deeper defects, an investigation at local area level using optical flow (OF) is reported in this chapter.

OF is widely used to trace the motion between two images at two different times, and the displacement in temperature intensity between two thermal images at times  $t$  and  $t+\Delta t$  reflects the heat propagation within the time slot  $\Delta t$ . Both the amplitude and direction of this heat propagation can be calculated via OF with the appropriate optimisation as discussed in Section 5.1. Thus, heat propagation and interaction in defective regions can be observed and quantified. Different flow patterns for different types of defects can be used to classify them, which is reported in Section 5.2; Finally, the features extracted from the OF results at the local area level of a defective region can be used for the QNDE of defects, which is presented in Sections 5.3 and 5.4.

### 5.1 Optimisation of Optical Flow for ECPT

Since the parameters chosen vary in different applications, an optimisation should be carried out before processing the captured thermal images, which involves for example critical time selection or threshold selection. This section discusses OF optimisation, particularly for thermography. Feature extraction for defect classification and QNDE are subsequently reported in Sections 5.2, 5.3 and 5.4, respectively.

#### *5.1.1 Time slot selection of OF for defect characterisation*

A 200 ms heating duration followed by 300 ms cooling at a 383 Hz frame rate is selected for inspection, which is long enough to elicit an observable heat pattern around

the impact damage from sample Set 3. To reduce the calculation costs, every 10 frames are treated as one time slot, where  $\Delta t = 10 / 383 = 26$  ms. The pixel number for OF amplitude over a threshold, which is named 'thres' as the percentage of the maximum value, against time in transmission mode is plotted as Figure 5.1. There  $t_1$ ,  $t_2$  and  $t_3$  indicate the time where maximum  $dT/dt$ , maximum  $T$  and minimum  $dT/dt$  occur, respectively. From the curves, it can be found that the peak pixel number is at 75 or 80 frames at the 383 Hz frame rate, where  $t_2$  denotes the maximum heating time as shown in Figure 5.2. At time  $t_2$ , the pixel number of OF for various impact energies achieve the largest value. Therefore, the end of heating is the best time slot to apply OF.

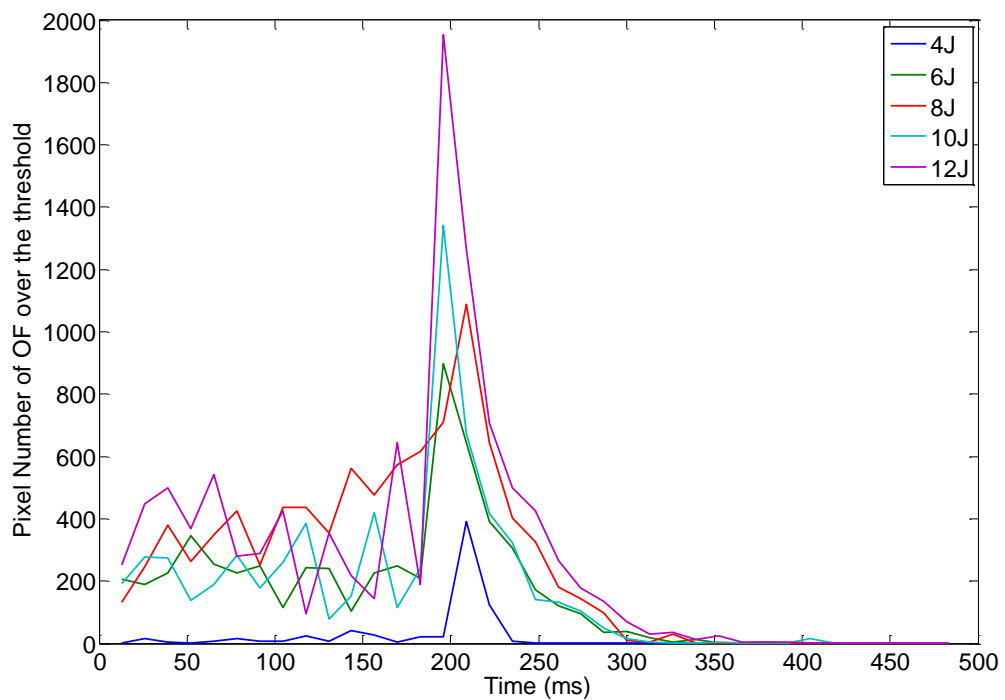


Figure 5.1 Number of pixels with OF amplitudes over the threshold 'thres' =5.5 against time.

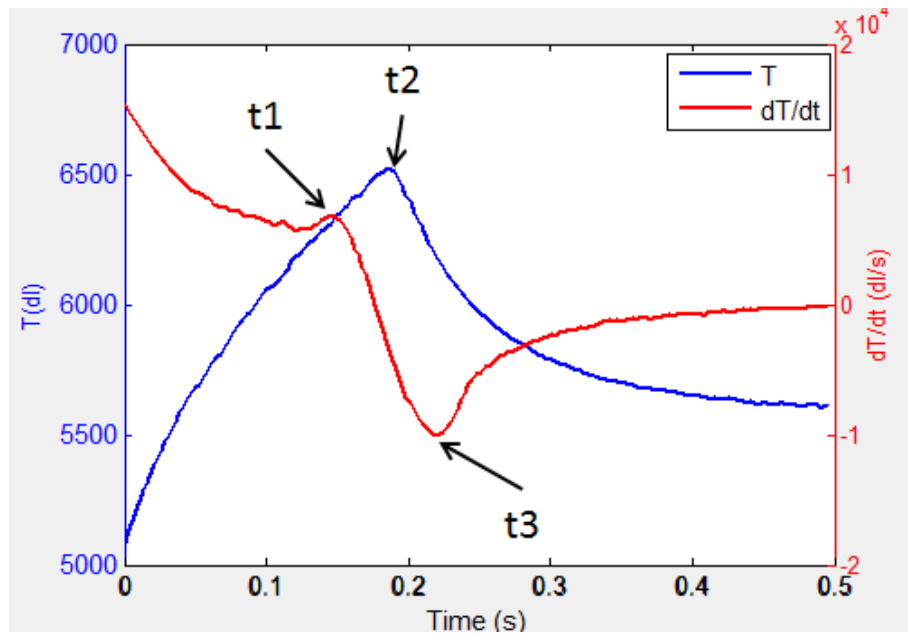


Figure 5.2 Specific time in a typical transient thermal response (temperature response in blue and the first derivative of temperature in red).

### 5.1.2 Threshold selection for optical flow

Taking 12J-impacted sample from sample Set 3 as an example, different thresholds of minimum amplitude of OF are compared. The amplitude map for OF is compared with the thermal image at the maximum heating time to find the best threshold range to describe the defective region.

The thermal image at maximum heating is shown in Figure 5.3. The unit of the temperature is the digital level computed using the 'Alair' software, provided by the thermal camera company Flir. A larger DL means a higher temperature. As shown in Figure 5.3b-d, the OF amplitude map for 12J-impacted sample are presented in grey scale-white for high amplitude and black for low amplitude. From Figure 5.3, it can be seen that the OF amplitude map shows the whole heated area rather damaged area when the threshold is low ("thres" =5 in Figure 5.3b), whereas it shows mainly the damaged area when the threshold reaches 8 (Figure 5.3d). This is because a lower threshold allows the presentation of the small flow in the defect-free region and a higher threshold filters out the small flows and predominately presents the flows around the impact damage. Therefore the threshold 'thres' is chosen to be 8 for the impact damage investigation, whilst 'thres' equals 5.5 as a reference.

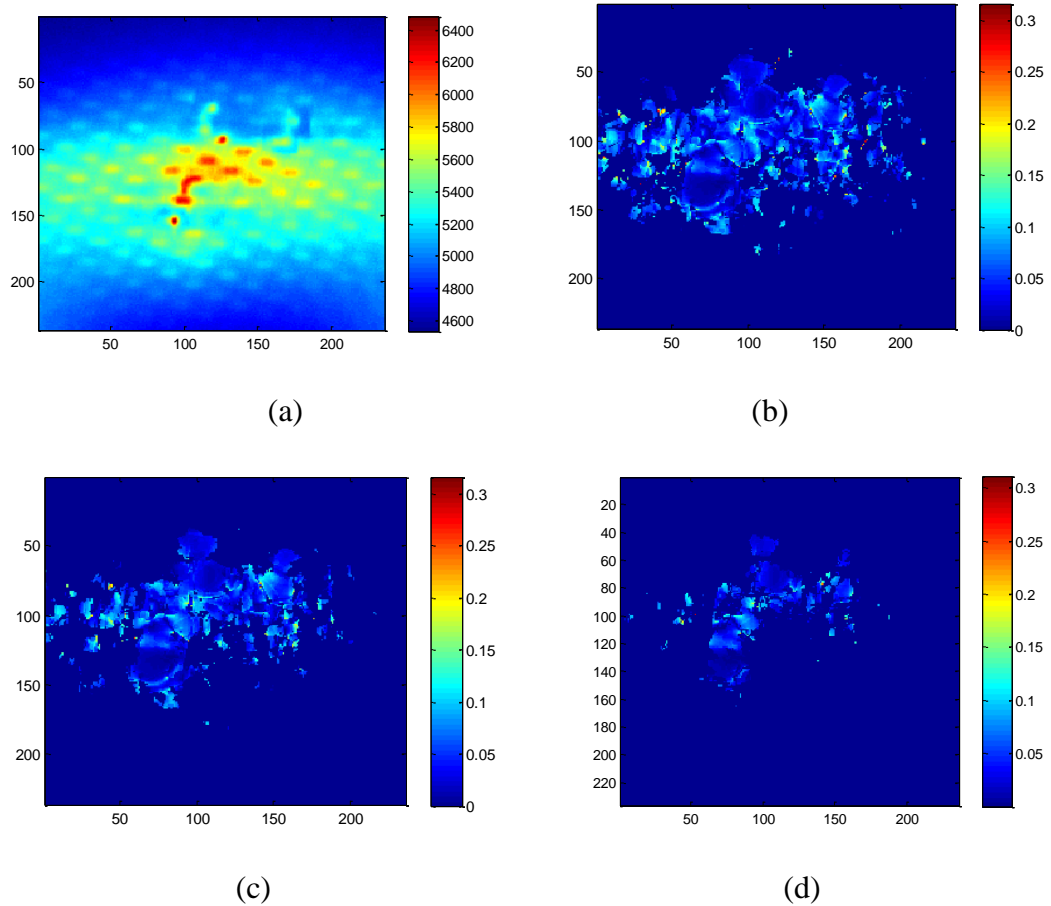


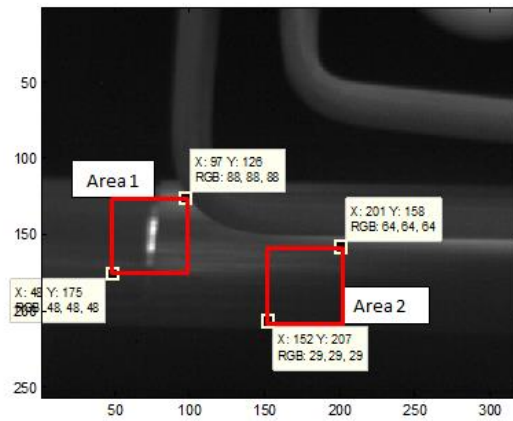
Figure 5.3 (a) Thermal image for 12J-impacted sample from “Set 3” at maximum heating, where the unit is digital level (DL) and OF amplitude maps with varying thresholds: (b) thres =5; (c) thres =5.5; (d) thres =8.

## 5.2 Defect classification at local area level

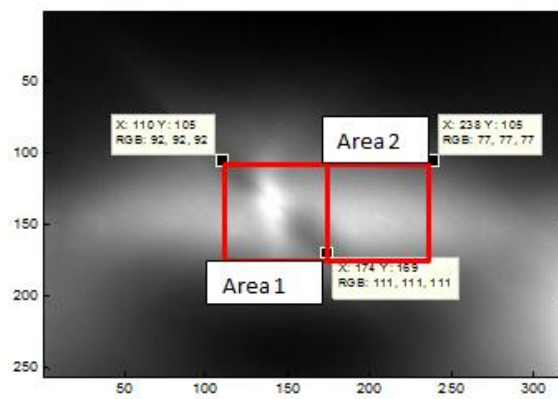
In this section, the defect classification using optical flow is presented. The optimised time-slot and threshold are used based on the results from Section 5.1.

### 5.2.1 Thermal images of three types of defects

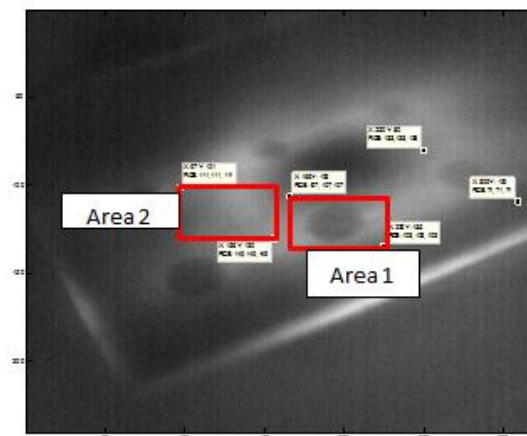
Sample Sets 1, 2, and 4 are used for defect classification at local area level. Figure 5.4 shows the thermal images at maximum heating for cracks (Sample Set 1), impact damage (Sample Set 2) and delamination (Sample Set 4).



(a)



(b)



(c)

Figure 5.4 Thermal images at maximum heating for (a) crack, (b) impact damage, (c) delamination. The marked area 1 in each image shows the defective region and area 2 indicates the defect-free region.

It can be seen that when the eddy currents encounter a discontinuity such as a crack, delamination or impact damage, they are forced to divert, leading to regions of increased or decreased eddy current density. For cracks, the accumulation of heat at the crack bottom can be observed in Figure 5.4a. After the period of eddy current heating, the nature of the crack also affects heat diffusion in the cooling phase by acting as a thermal barrier. With impact damage, the electric conductivity decreases at the impact point, the eddy current density is higher at the impact point than other regions. This leads to a hot-spot at the impact point, as shown in Figure 5.4b. Besides this, two dark regions to the upper left and lower right of the impact point are also observed in Figure 5.4b. This is because two delaminations are generated near the rear side of the sample due to the high impact energy. For the two delaminations in Figure 5.4b and the six in Figure 5.4c, a thermal barrier, the delamination, hinders heat propagation mainly along the fibre orientation, which results in hot-spots on the delamination edge and cool-spots in the delamination region, as shown in Figure 5.4c.

The OF results for these three thermal videos reported in Section 5.2.2 is given an explanation from the angle of heat propagation.

### ***5.2.2 Optical flow results***

The optical flow images in conjunction with the respective thermal images at the end of heating phase of defective areas in samples with impact damage, delamination and crack samples are shown in Figure 5.5. The blue arrows denote the calculated OF direction and amplitude, whilst the red arrows shown the OF patterns summarised from the OF results. To simplify the OF images, only one flow arrow is drawn with a specific interval, shown as x2 (or 3, 4) pixels in Figure 5.5.

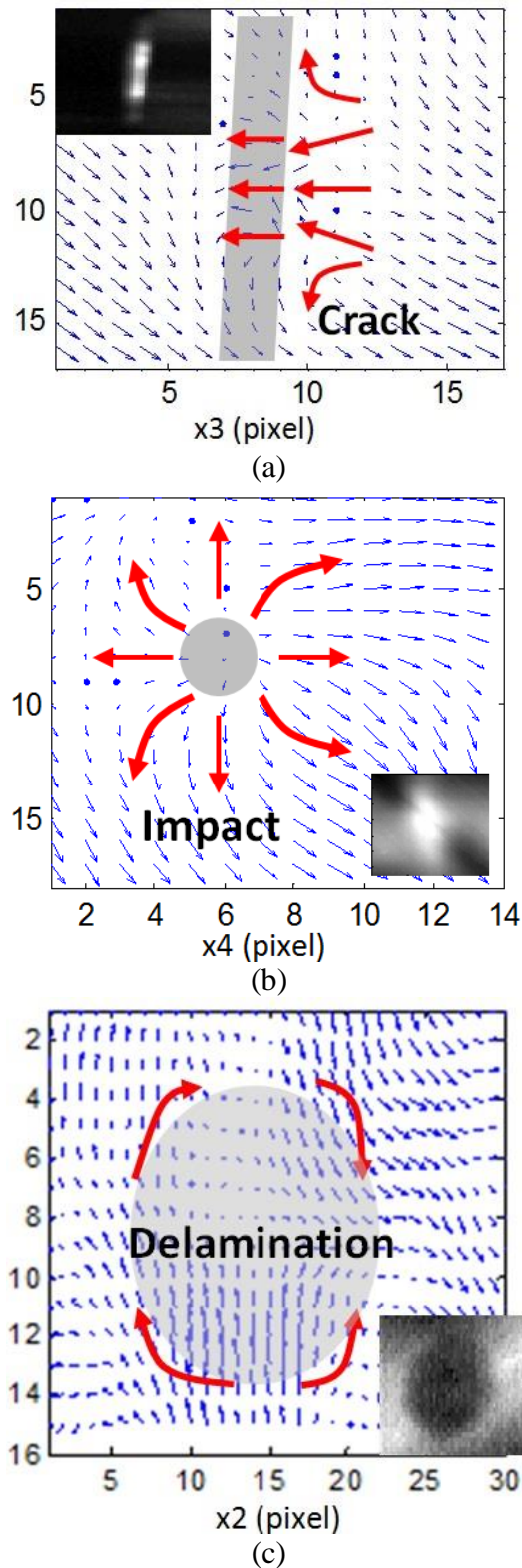


Figure 5.5 Optical flow distribution images at the end of heating compared with thermal images within “Area 1” in Figure 5.4 for: (a) crack, sample Set 1, (b) impact damage, sample Set 2, (c) delamination, sample Set 4 respectively. Transmission mode is used. The time-slot for optical flow is from 175 ms to 200 ms. The length and direction of arrows in figures denote the magnitude and orientation of heat flow.

Figure 5.5a presents the OF pattern in the crack region. In crack defects, the eddy currents cannot penetrate the crack, and must instead be diverted to the bottom of the crack, where, the heat accumulates as a result. The centre of the crack bottom closest to the excitation coil receives the most heating due to the lift-off effect of the eddy current. Figure 5.6a shows a schematic diagram of heat propagation in the crack in both top and cross-section views and Figure 5.6b shows the simulation results of heat flux density for a 2 mm deep crack, using the model described in Section 4.2.2. The heat along the fibre orientation cannot directly propagate through the crack, because of the discontinuity of the fibre at the crack. Therefore, the heat must either propagate around the crack bottom (Figure 5.6a, cross-section view) or along the crack (Figure 5.6a, top view). Since the experimental results only show the top view of temperature distribution, OF cannot be used to investigate heat propagation investigation in the cross-section view. But the simulation results in cross-section view verify the hypothesis of heat propagation inside the specimen, as shown in Figure 5.6b. From Figure 5.6b, it can be seen that the heat flux density at the crack bottom is higher, which means that the heat mainly propagates at the crack bottom via diversion. Combining the above phenomena, the OF results shown in Figure 5.5a prove that the above two phenomena of heat propagation occur in the sample with a crack in the top view. It can be seen that some of the heat flow is diverted upwards or downwards when encountering the crack; some goes through the crack, and this mainly occurs around the bottom of the crack. Because the crack crosses the whole width of the specimen, it is easier for the heat to propagate around the crack bottom than to spread along the crack. That is why we can see the amplitude of OF is larger when crossing the crack bottom.



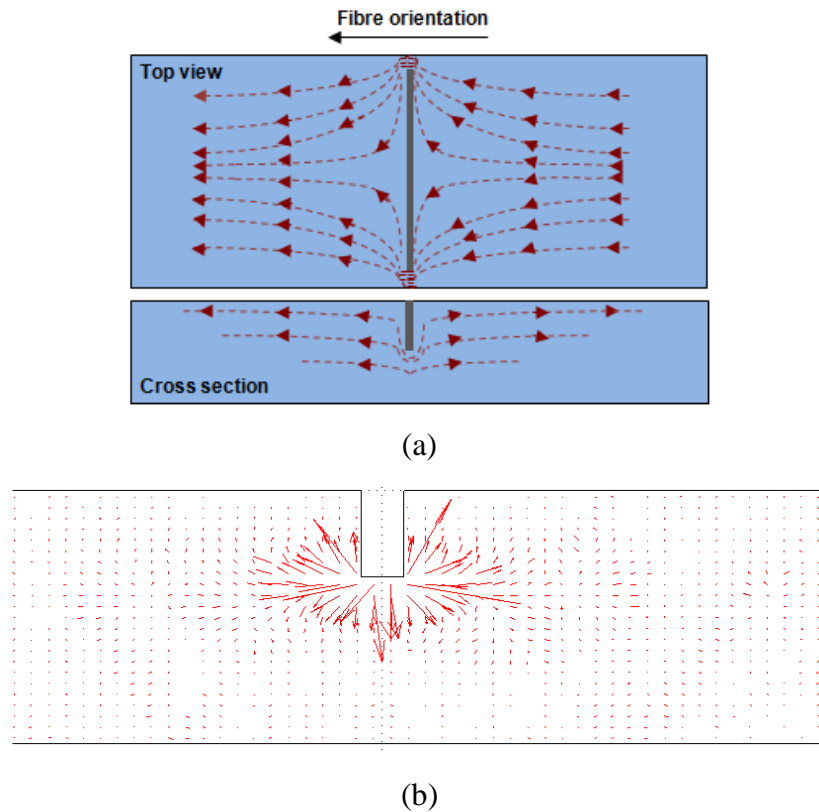


Figure 5.6 (a) Schematic of heat propagation at the crack in top and cross-section views; (b) simulation result of heat flux density for 2 mm deep crack, cross-section view

For impact damage, as shown in Figure 5.5b, the decrease of electric conductivity at the region of impact leads to heat concentration as proven in Section 4.3. Also the thermal conductivity increases at that region, which results in rapid heat propagation. Therefore, the rate of temperature increase at the impact region is higher than in other areas and the heat propagates rapidly from the impact to the surrounding region, which leads to the heat flow spreading around the impact. The experimental results are verified by numerical simulation using the model described in Section 4.3.2. Figure 5.7 shows the heat flux density on the impacted specimen surface in arrow format. From Figure 5.7a in top view, it can be seen that the heat flux spreads from the impact region to all around. In the cross-section view, it can be seen that the heat mainly propagates from the bottom to the top, since the transmission mode is being simulated. In the impact region, heat also propagates from the centre towards the boundary of the impact region, because of the influence shown in Figure 5.7a. Combining the above phenomena, a “spreading” OF pattern is derived for impact damage, as shown in Figure 5.5b.

The plane of delamination is parallel to that of the excitation coil, which means that there is little eddy current diversion at the delamination. However, the heat generated by the eddy current propagates along the fibre orientation because the thermal conductivity is the largest in that direction. As shown in Figure 5.8, delamination works as a thermal barrier. When the heat propagates to the delamination, mainly along the fibre orientation, it is hindered by the delamination. The heat can only go around the delamination edge in the  $x, y$  direction or be diverted in the  $z$  direction (across the thickness). In the top view in Figure 5.8, the heat propagates around the delamination edge when encountering the delamination. Since the specimen under test has multiple fibre orientations in different layers, the direction of heat propagation around the delamination varies. This is why there is a difference between the OF results in Figure 5.5c and the schematic diagram of heat propagation in top view in Figure 5.8. From the cross-section view, the heat also goes around the delamination. As shown in Figure 5.8, the fibre orientations in the first and the second layers are towards the left and the inside respectively. Thus, the heat flow propagates upwards and then downwards in the first layer; and downwards and then upwards in the second layer to be diverted. Combining the above phenomena, it can be seen that the flows go around the delamination marked in red arrows and also some of the flows go into the delamination, which is represented by the diversion of flows in the thickness ( $z$ ) direction in Figure 5.5c.

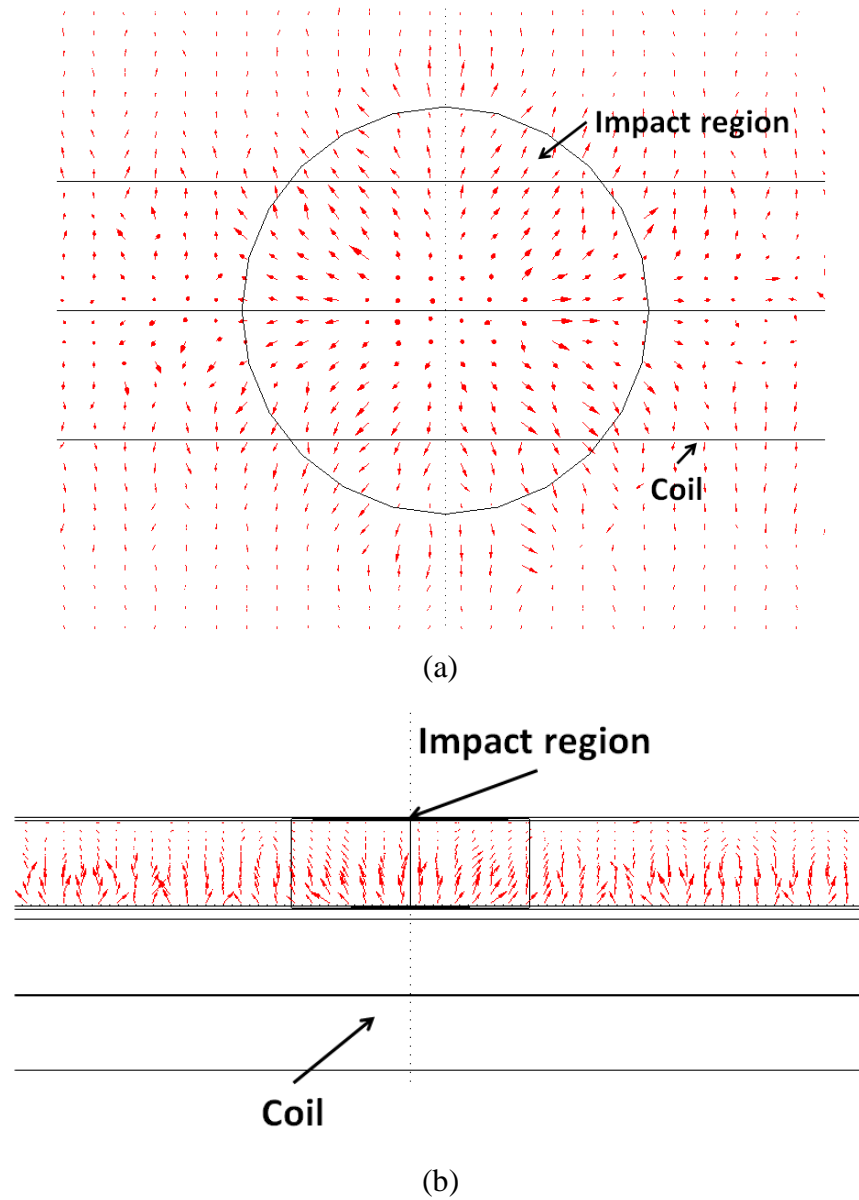


Figure 5.7 Simulation results of heat flux density in (a) top view and (b) cross-section view along the central horizontal line as shown in (a).

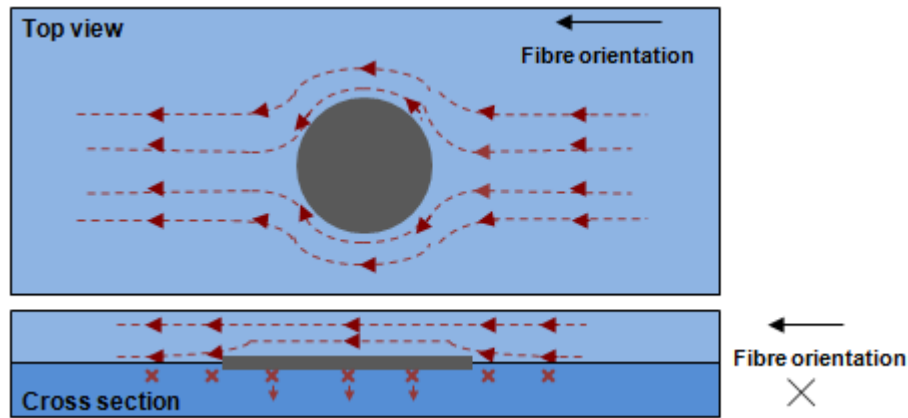


Figure 5.8 Schematic of heat propagation at delamination in top and cross-section views

### 5.2.3 Discussion

Based on the OF results reported in Section 5.2.2, the flow patterns at the local area of defects are different for crack, impact damage and delamination, because the variations in directional electric or thermal conductivity are not the same. This allows defects to be classified by investigating the OF patterns at the local area level. The OF patterns for the three types of defects can be summarised as follows:

- Crack: the flow is mainly diverted from the bottom of the crack; some of the flows go around the crack interface;
- Impact damage: the flow spreads from the impact point in all directions;
- Delamination: flow mainly propagates around the edge of the delamination.

### 5.3 Case study 3: QNDE for impact damage

The ECPT investigation at local area level can be used to classify defects as discussed in Section 5.2, but also to quantify them. In this section, impact damage is taken as an example and the defective area against the impact energy is investigated through OF features.

In this case study, a heating time of 200ms followed by a cooling time of 800ms is applied at the maximum frame data acquisition rate of 383 Hz. Rather than reflection mode used in Section 4.3, the transmission mode is used instead to avoid the

overlapping of coil and thermal images. In this mode, the coil is placed at the opposite side from the thermal camera.

Figure 5.9 shows the optical flow images in conjunction with the thermal images from 175 ms to 200 ms for impact damage sample Set 3 described in TABLE 3-I. As shown from the case study in Section 4.3, the impact leads the electric conductivity to decrease and the thermal conductivity to increase in the impact area. As a result, the heat generated from eddy currents in the impact region is higher than that in the defect-free area; and the speed of heat propagation is faster in the impact region. As the impact energy increases, the variations in electric and thermal conductivities in the impact region also increase. In addition, the defective area is also enlarged with the increase of the impact energy. From the results, the impact region is highlighted and localised in the images. It can be seen that the flow area marked in purple increases as the impact energy increases, except for 12J-impacted sample in which a surface crack is produced and so the flows are concentrated in the crack region, shown in Figure 5.9e. Therefore, the flow is denser in the cracked region for 12J.

To analyse the impact energy information, the pixel number of OF above the threshold ( $PN_{OF}$ ) is used to estimate the area of defects. A monotonous relationship between impact energy and estimated defective area is shown in Figure 5.10, by counting the number of optical flow arrows in the respective optical flow images. From the results, it can be seen that  $PN_{OF}$  increases nearly linearly with increasing impact energy.

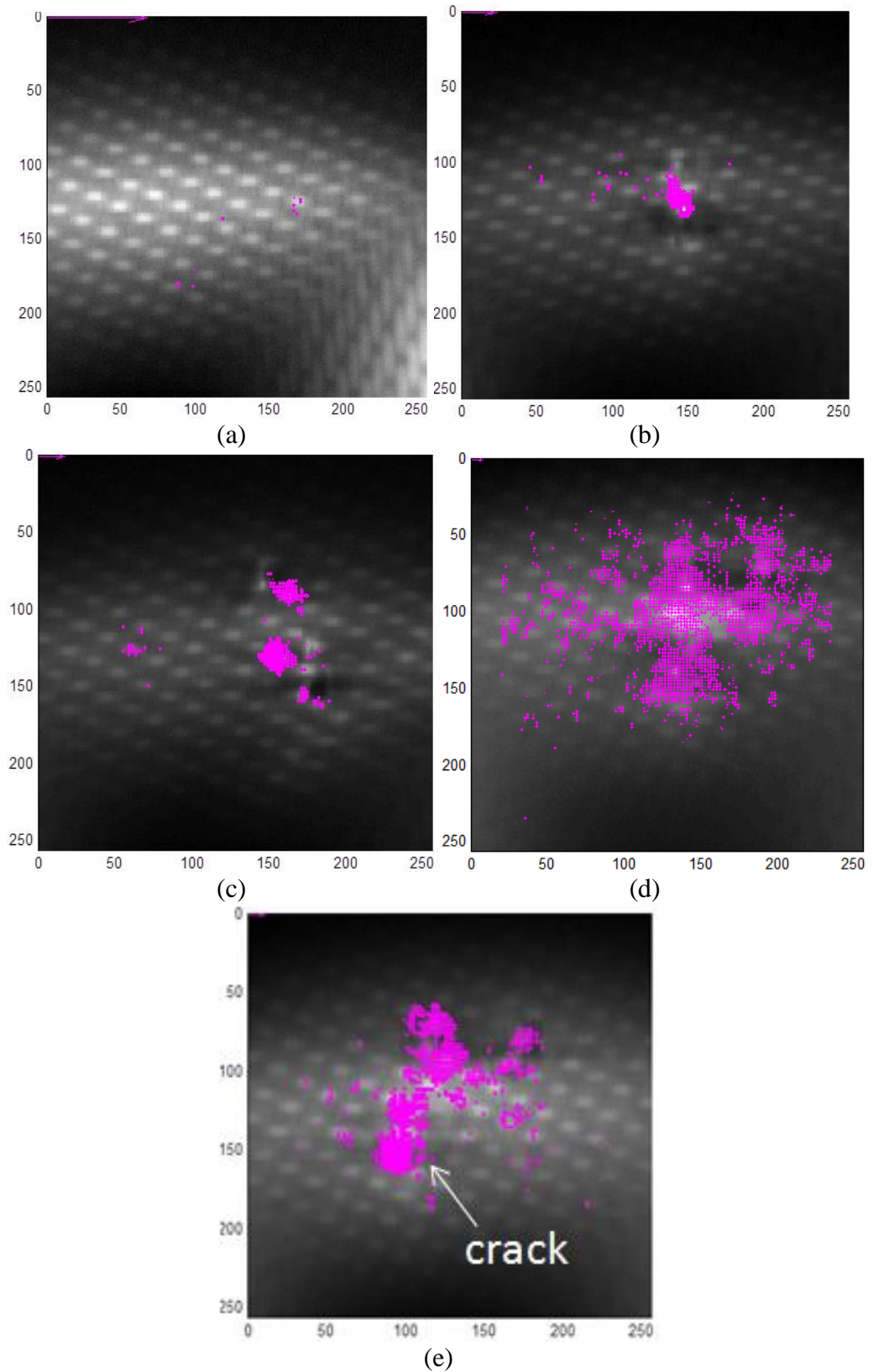


Figure 5.9 Optical flow images at the end of heating compared with thermal images within selected regions for samples with (a) 4J, (b) 6J, (c) 8J, (d) 10J, (e) 12J impact energies. Transmission mode is used. The time-slot for optical flow is from 175 ms to 200 ms. The purple arrows denote the OF with the amplitude above the threshold.

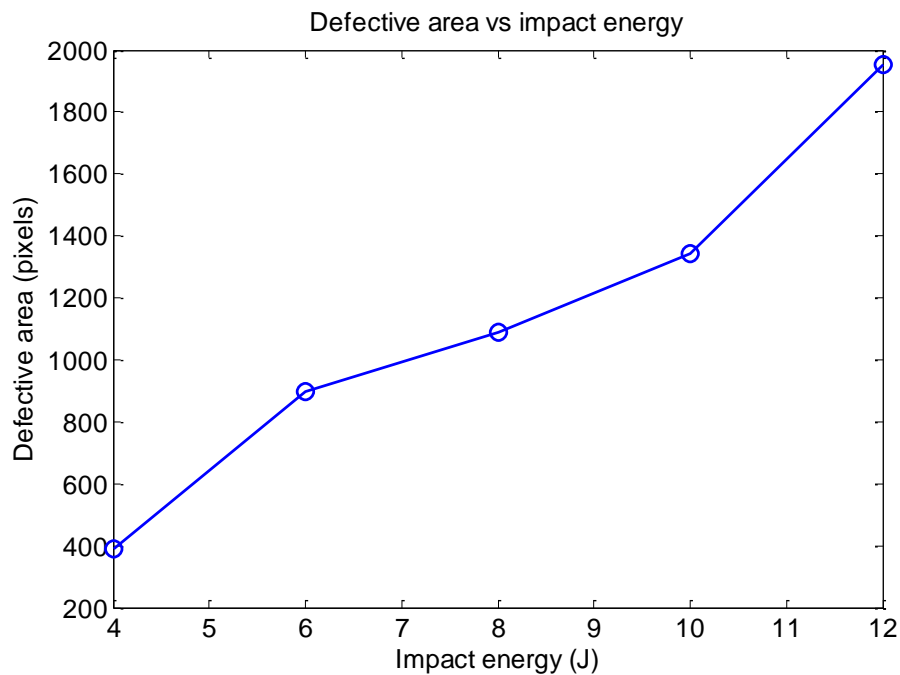


Figure 5.10 Pixel number (area) above OF threshold vs impact energy at maximum heating time.

The fibre texture of sample Set 3 is the most complicated, and its woven fibre texture is shown in Figure 5.11. Due to the overlapping fibres, the optical flow distribution does not accurately describe the heat propagation, especially in the defective region. No relationship between the variation in properties and OF features is found, which demonstrates the limitation of OF for ECPT investigation at local area level. To overcome this problem, an ECPT investigation is conducted at the pattern level using PCA or ICA to distinguish multiple defects and separate the fibre texture and defects is introduced in Chapter 6.

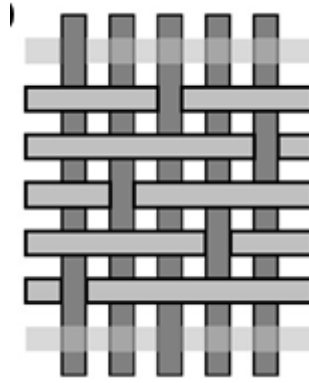


Figure 5.11 Woven structure of sample set 3.

#### 5.4 Case study 4: Uni-directional sample under directional tensile stress

In the situations described in Section 5.3, the fibre texture is complex and the heat propagates in more than one direction. The use of OF for QNDE encounters some problems in such situations. To simplify the influence of fibre texture, a sample with uni-directional fibre is tested in this case study. To make sure that the variation in properties only along the fibre orientation, tensile stress is applied within elastic region of CFRP sample in this direction.

An Instron model 3369 universal test machine with a maximum load capacity of 50 kN is used to generate tensile stress in the sample, as shown in Figure 5.12. The tensile stress is controlled and displayed through Instron Bluehill2 software. In this section, stress from 0N to 4000N with 1000N intervals is applied.

Due to the complex fibre texture of the impact damage samples, the level of OF amplitude in either the horizontal or vertical direction is difficult to measure accurately since the heat propagation is complicated. Therefore, a uni-directional CFRP sample of the same brand as sample Set 1 is used for the extraction of directional information, because here heat propagation mainly occurs along the fibre orientation. Varied levels of tensile stress are applied vertically to produce variation in the material property. Transmission mode is used, where the inductor and thermal camera are placed on opposite sides of the sample. The inductor is fixed horizontally behind the sample. The fibre orientation is vertical as shown in Figure 5.13.





Figure 5.12 Instron model 3369 universal test machine and Flir thermal camera.

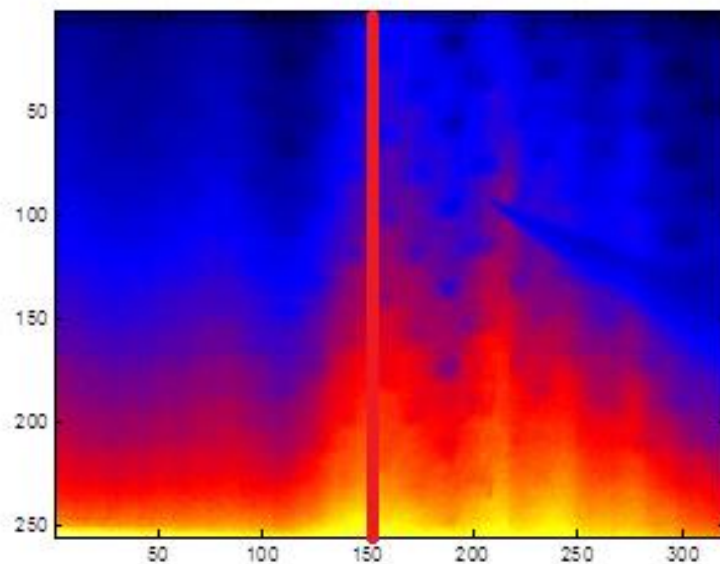


Figure 5.13 Thermal images for the sample under tensile stress at maximum heating (the fixed line with respect to the pin marker is in red; the horizontal and vertical coordinates denote the  $x$  and  $y$  position in the thermal image).

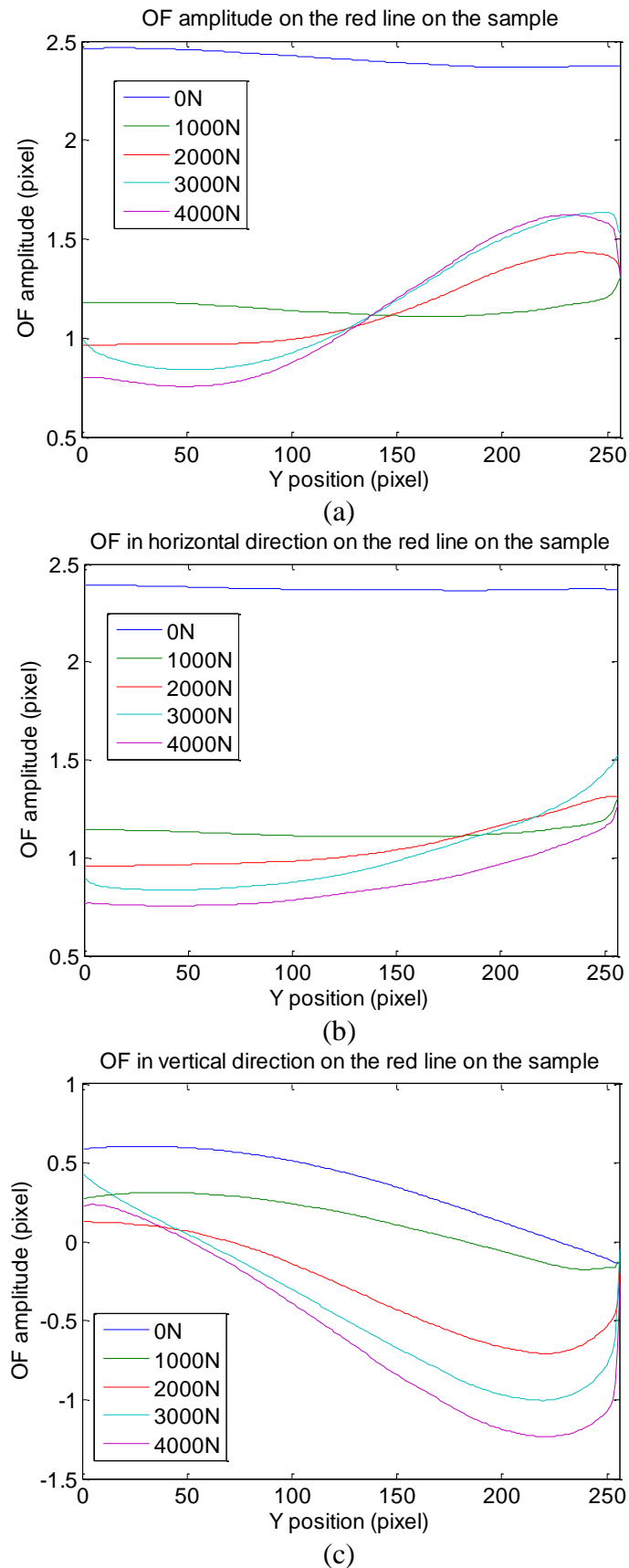


Figure 5.14 Optical flow at end of heating along the red line marked in Figure 5.13: (a) amplitude for overall flow; (b) amplitude in horizontal direction; (c) amplitude in vertical direction. Frame interval is 10. The y position 0 denotes the top of the line and position 256 denotes the bottom of the line.

Figure 5.14a shows the overall OF amplitude at the end of heating along the red line marked in Figure 5.13, whilst Figure 5.14b and Figure 5.14c show the individual horizontal and vertical OF amplitude respectively from  $u$ ,  $v$  vector along the line. The interval between the two images for each calculation is set at 10 frames.

Because the coil is placed horizontally, the flow in the horizontal direction is larger than that in the vertical direction, which can be seen from Figure 5.14b and Figure 5.14c, irrespective of whether or not the tensile stress is applied. When the tensile stress is applied vertically, the electric conductivity in the vertical direction increases [159], whilst the change in the horizontal direction is not dependent on the tensile stress. Therefore, it can be concluded that the OF amplitudes in the horizontal direction do not have a monotonous relationship with tensile stress, but that the OF amplitude in the vertical direction decreases as tensile stress increases. The absolute value of vertical OF amplitude shows the displacement between the two thermal images at the end of heating with an interval of 10 frames. A positive value of vertical OF amplitude means that the heat propagates downwards, and a negative value means that the heat propagates upwards in Figure 5.13. Thus, as the tensile stress increases, the heat propagation upwards becomes faster. The region at the bottom of the marked line in the  $y$  position from 235-256, is the location where the coil is placed. The OF amplitude in the vertical direction is near to zero, because heat is continuously generated at that region. It can be noted that the OF amplitude in vertical direction is large where it is close to the heating source, along the marked line. In terms of heat diffusion, the region near to the heat source has a large convergence in temperature, which results in a large OF or, we can say, more heat propagation. In this case, OF amplitude in each direction reflects the directional variation in material properties and heat propagation.

## 5.5 Chapter summary

In this chapter, the ECPT investigation at local area level using OF has been reported, including the selection of the time slot and threshold for the optimisation of OF. An optimisation has been carried out to choose an appropriate investigation time-slot (maximum heating time) and threshold ('thres' = 8) for the ECPT investigation at local area level.

From the case study of defect classification, it is concluded that the flow patterns at the local area of a defect are different for crack, impact damage and delamination, because the variations in directional electric or thermal conductivity with different types of defects are not the same. This allows us to classify defects through investigation at the local area level using OF patterns. OF patterns for the three types of defects can be summarised as follows:

- Crack: the flow is mainly diverted from the bottom of the crack; some of the flows go around the crack interface;
- Impact damage: the flow spreads from the impact point in all directions;
- Delamination: flow mainly propagates around the edge of the delamination.

From the case study of QNDE to quantify impact damages, in terms of impact energy and area of defects, the pixel number of OF above the selected threshold ( $PN_{OF}$ ) ('thres' = 8) has been extracted. The results showed that  $PN_{OF}$  increases as the impact energy increases.

Due to the complex fibre texture of impact damage samples, OF amplitude in either the horizontal or vertical direction is difficult to determine accurately. A uni-directional sample is used for evaluation of the variation in directional properties in the case study of uni-directional sample under tensile stress along the fibre orientation. The results showed that the OF amplitude in the fibre direction increases as the tensile stress in the same direction increases (*i.e.* electric conductivity increases).

Comparing these three case studies, the advantages and disadvantage of the ECPT investigation at local area level have been shown. Firstly, it achieves relatively good QNDE results for deeper defects from impact damage with a complex woven fibre texture. Secondly, the three types of defect can be classified from the flow patterns at the defective region. However, thirdly, it is not accurate in separating the fibre texture influence away from the defects when the fibre texture is complex. Furthermore, the flow pattern becomes more complex or blurred given the existence of multiple defects. To overcome the drawbacks of the ECPT investigation at the local area level in complex fibre texture, the investigations at the pattern level using PCA and ICA are presented in Chapter 6.

## Chapter 6. ECPT INVESTIGATION AT THE PATTERN LEVEL

As discussed in Chapters 4 and 5, ECPT investigation at the pixel level gives good results in defect evaluation and quantification for simple fibre textures and surface defects. However, it is not accurate when the fibre texture becomes complex and/or the defect is not on the surface of the sample. This is because the correct pixel to demonstrate the defect information is hard to select. However, ECPT investigation at the local area level can obtain flow patterns which can be used to investigate deeper defects, such as impact damage and delamination, but it is still limited in cases of complex fibre texture, such as woven fibre, and also when multiple defects exist. To achieve better results, the investigation at the pattern level using PCA and ICA of thermal image sequences is reported in this chapter.

From the nature of defects in the sample, it can be seen that the area of defect in the sample is much less than those of the surrounding, which indicates the sparse property of inspected sample. Here, 'sparseness' refers to a representational scheme where only a few units out of a large population are effectively used to represent typical data vectors. The deviation of material property at defects refers to variations in electric or thermal properties for the different types of defects. This directly results in the transient thermal responses at defective region, independent to those in defect-free area. Therefore, an integration of PCA and ICA is implemented dedicated for the sparseness and independence of defect in this chapter.

The principles of PCA and ICA applied to thermal image sequences are introduced in Sections 3.4.2. Using PCA, the dimension of data is reduced. The first eight or more weighted orthogonal vectors are then derived to form PC images; whereas ICA [160] seeks the most weighted independent vectors to form the IC images.

In this chapter, the investigation at the pattern level is implemented by applying two processes as discussed in Section 3.4.2. PCA maximizes the variance of the investigated

data along the orthogonal directions and reduces its dimensionality, and ICA finds the vectors onto which the data are independent. The aim of integrating PCA and ICA is to distinguish between the different influences on the thermal sequence and transient temperature responses, which include heat (or eddy current) interaction at defect-free regions and defects, fibre orientation and texture, and induction heating from the coil. In the following two sections, PCA and ICA are implemented respectively in investigating the defects. In Section 6.1, PCA is applied to extract the features for crack, impact damage and delamination with reduction in the dimension of the data. Then in Section 6.2, MMCA, an ICA method dedicated for sparse nature of defects in the inspected sample, is used for separate the patterns from impact damage and its resulting other defects such as delamination. Sample Set 2 is used for both PCA and ICA in the investigation of impact damage for comparison.

## **6.1 ECPT investigation at the pattern level using PCA**

In this section, PCA is applied to three thermal videos of a crack, impact damage and delamination respectively, using the calculation procedure introduced in Section 3.4.2. The first  $m=8$  weighted PCs are reconstructed into PC images to display the patterns of defects. In this section, three types of defects, crack, delamination and impact damage, are processed using PCA. Among the eight PCs, the fifth to eight PCs contain mainly background noise. Therefore, the first four PCs are shown in this section for the different types of defects.

### **6.1.1 Cracks**

ECPT was used to inspect sample Set 1, as shown in TABLE 3-I. The 350 mm  $\times$  38 mm  $\times$  6 mm CFRP sample contains three cracks all with a width of 1 mm, but varying in depth from 0.5 mm to 2 mm. These cracks were manufactured in the workshop at Newcastle University. Reflection mode is used since the crack is not clear when transmission mode is used. In this experimental study, the coil is placed 2 cm away from the crack, in order not to lose information about the defect where the coil hides the crack. A 200 ms heating period followed by a 300 ms cooling period is set.

Figure 6.1 shows the results for the first four PC images taken from a thermal video recording the heating phase of a 2 mm deep crack.

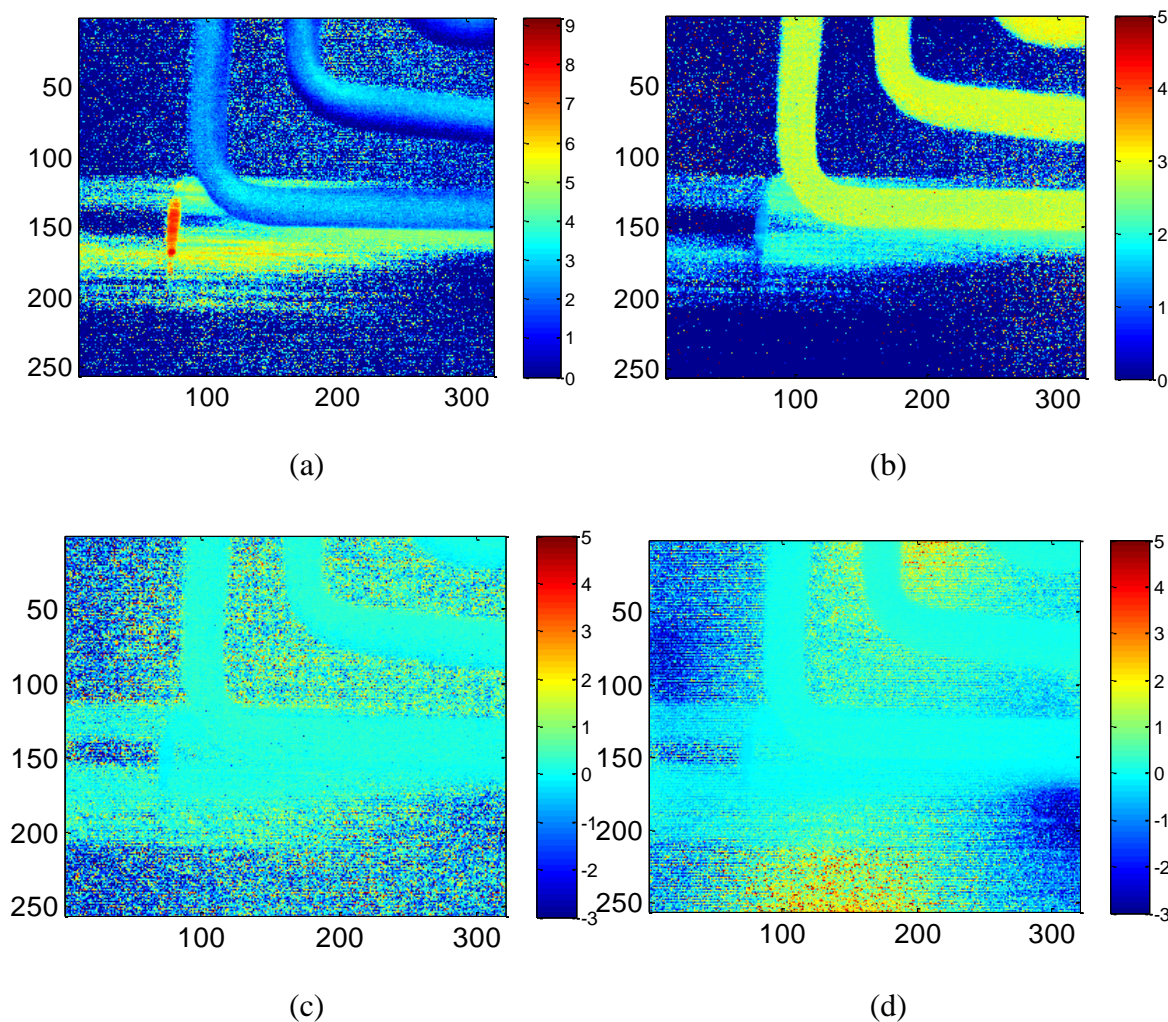


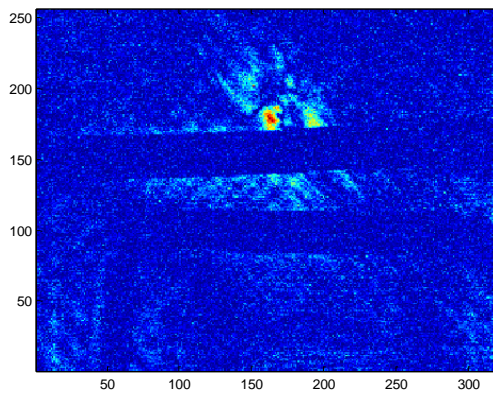
Figure 6.1 (a) 1<sup>st</sup> PC; (b) 2<sup>nd</sup> PC; (c) 3<sup>rd</sup> PC; (d) 4<sup>th</sup> PC of PCA for the thermal sequences in heating phase.

An abnormal area is observed at the bottom of the crack in the first PC image due to the increased eddy current density caused by eddy current diversion around this region. The interaction between the crack and the uniform eddy currents in the sample shows that eddy currents will always follow the path of least resistance. Hence, in a sample without a defect, they will be mainly confined to the surface layer along the sample thickness. When a discontinuity such as a crack interrupts the path of eddy currents, it will be forced to be diverted around the bottom of the crack, which leads to an area of increased

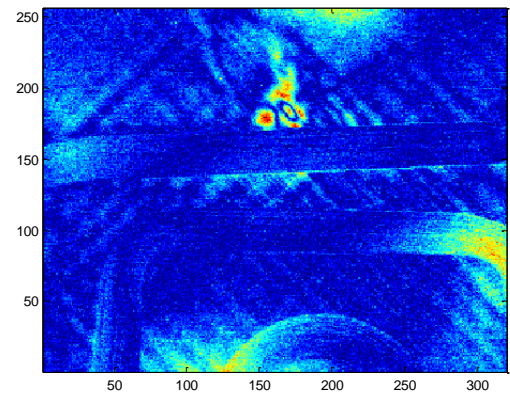
eddy current density and a resultant hot spot, which is enhanced in the 1<sup>st</sup> PC shown in Figure 6.1a.

### 6.1.2 Impact damages

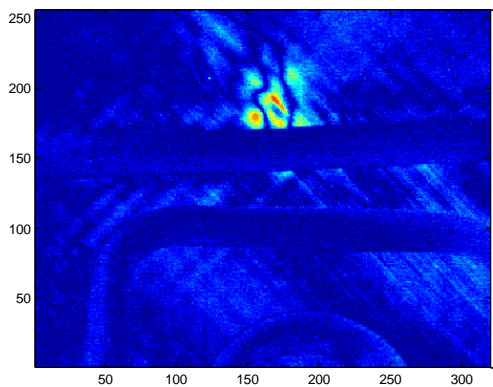
ECPT was used to inspect the impacted samples in Set 2. Reflection mode is used, where the coil and thermal camera are placed at the same side of the sample. A 200 ms heating period followed by an 800 ms cooling period is applied. Among the  $m=8$  PCs, the fifth to eighth PC images contain not only background noise. Thus, the first eight PC images of impact damage on the rear surface of the sample are shown in Figure 6.2.



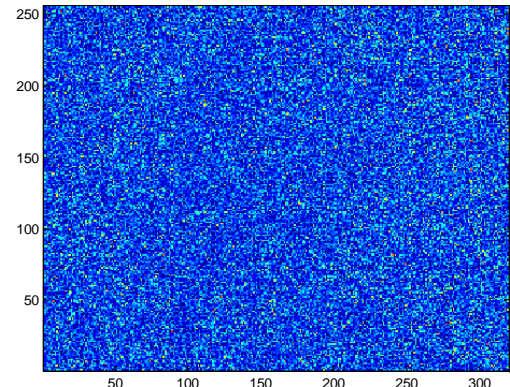
(a)



(b)



(c)



(d)



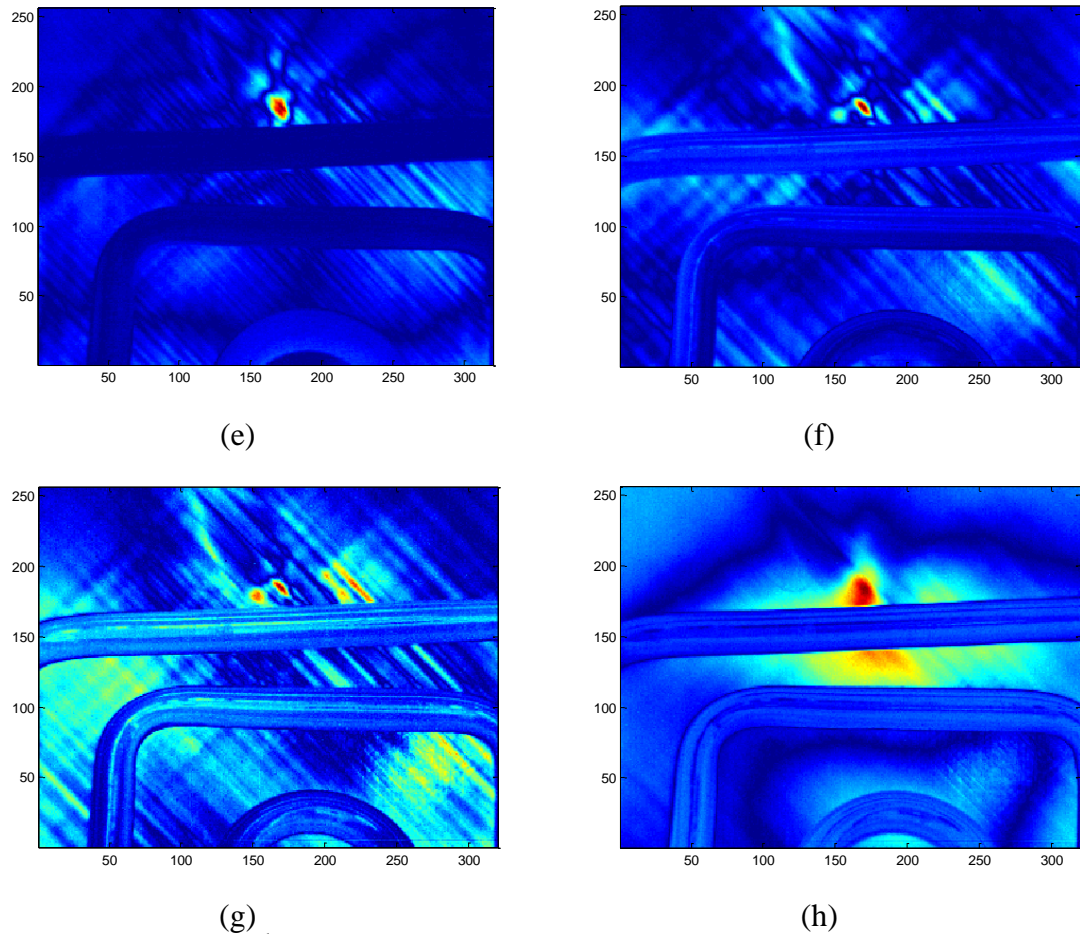


Figure 6.2 (a)-(h): 1<sup>st</sup>-8<sup>th</sup> PCs of PCA for the thermal sequences in heating phase, rear of the sample.

At the rear of the impacted sample, a hot-spot in the centre and a vertical bright line are observed, which shows the impact point on the front surface and a matrix crack generated by the impact. This is because the lower electrical conductivity at the impact point [161] leads to a diversion of eddy current in this area. Besides this, two dark areas at the upper left and lower right of the impact point indicate two delaminations close to the rear surface. Therefore, an impact can cause delaminations and matrix cracks when the impact energy is large enough.

### 6.1.3 Delaminations

A one-second heating period followed by a two-second cooling period with a maximum power output of 2 kW is applied during heating. Samples with delaminations 15 mm in diameter with varying depths are investigated. The left-hand four defects (marked as

numbers 1-4 in Figure 6.3e) are 155  $\mu\text{m}$  deep and the right-hand two (marked as numbers 5-6 in Figure 6.3e) are at a depth of 310  $\mu\text{m}$  deep. Delaminations at depths of 155  $\mu\text{m}$  and 310  $\mu\text{m}$  can also be seen in the PC images shown in Figure 6.3 (a)- Figure 6.3 (d).

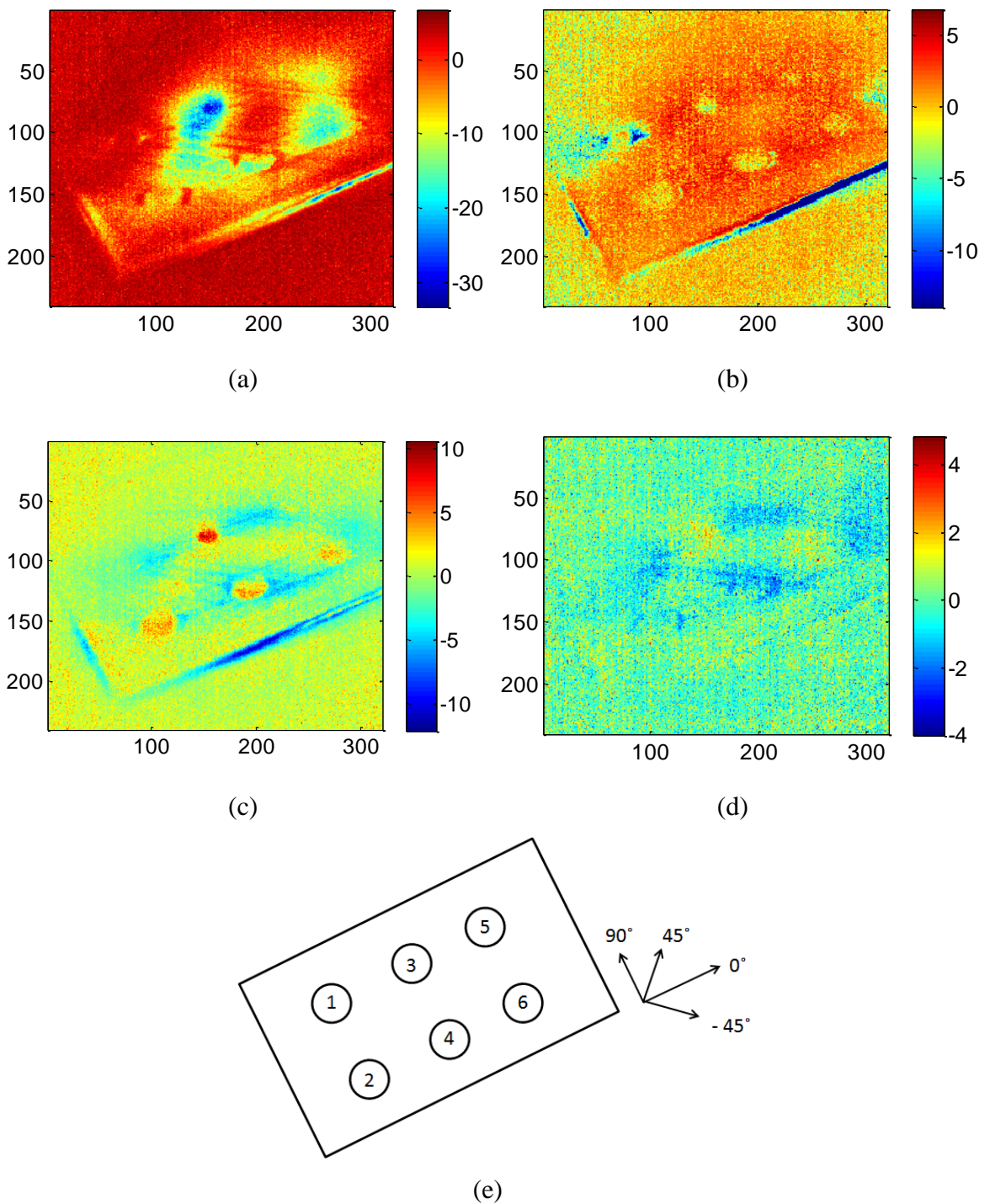


Figure 6.3(a) 1<sup>st</sup> PC; (b) 2<sup>nd</sup> PC; (c) 3<sup>rd</sup> PC; (d) 4<sup>th</sup> PC of PCA for the thermal sequences in heating phase; (e) numbered delaminations and fibre orientation definition

It is known that delaminations cause small distortions in eddy current distribution, since eddy currents parallel to the layers interact slightly with the delaminations. The heat is generated mainly in the  $0^\circ$  and  $-45^\circ$  direction along the fibre orientations, respectively as defined in Figure 6.3e. Since the largest electric and thermal conductivities occur along the fibre orientation, it can be shown that the fibre orientations in the first and second layers are  $-45^\circ$  and  $0^\circ$  respectively. As a thermal barrier, the delamination hinders heat propagation mainly in the  $0^\circ$  and  $-45^\circ$  directions, which makes the delamination edge hotter and the delamination region cooler. As a result, it can be seen that there is a large contrast between the delamination and its edge in the PC images, particularly in the 2<sup>nd</sup> and 3<sup>rd</sup> PCs.

#### **6.1.4 Discussions**

Three types of defects have been demonstrated to exhibit different patterns in the first four PC images. The PC images emphasise a large contrast associated with defects in comparison to non-defective regions, and therefore provide a guide on how to select the proper pixels or regions of transient response in order to classify the three types of defects. In this way, the dimension of data is reduced from  $N \times k$  down to  $m \times k$ , where  $N=383$ ,  $m=8$ ,  $k=320 \times 256=81920$ . Since the abnormal patterns at defect are obtained, transient temperature responses at the most abnormal pixels using the algorithms described in Chapter 4 can enhance the results of the investigation at pixel level.

However, PCA only works well if sources are Gaussian and it cannot guarantee the independence of the extracted patterns. In other words, each of PCs are not completely separated, and this inevitably makes it difficult to classify the defect type for each PC (*e.g.* Figure 6.2b, f and g contain both impact damage and delamination). Thus, the MMCA can be more adaptable for the investigation at the pattern level.

#### **6.2 ECPT investigation at pattern level using ICA**

Since the factors contributing to heating effects in thermal sequences are not necessarily orthogonal, ICA is applied in this section to sample Set 2 based on the dimension-reduced matrix  $\mathbf{I}'_M$  using PCA in previous section. The principle of the ICA algorithm is introduced in Section 3.4.3. A specific ICA algorithm, Multichannel Morphological

Component Analysis (MMCA), is chosen for this sparseness problem. The defect in CFRP described in TABLE 3-I meets the criterion of the sparseness of features in MMCA, because the pixel number of informational data at the defective region is much smaller than that of the overall image

As in Section 6.1.2, ECPT was used to inspect the impacted samples in Set 2. Reflection mode is used as the same setting-up as that using PCA in Section 6.1.2, where the coil is placed below the impact point. A 200 ms heating period followed by an 800 ms cooling period is applied. The thermal image at 200 ms is shown in Figure 6.4.

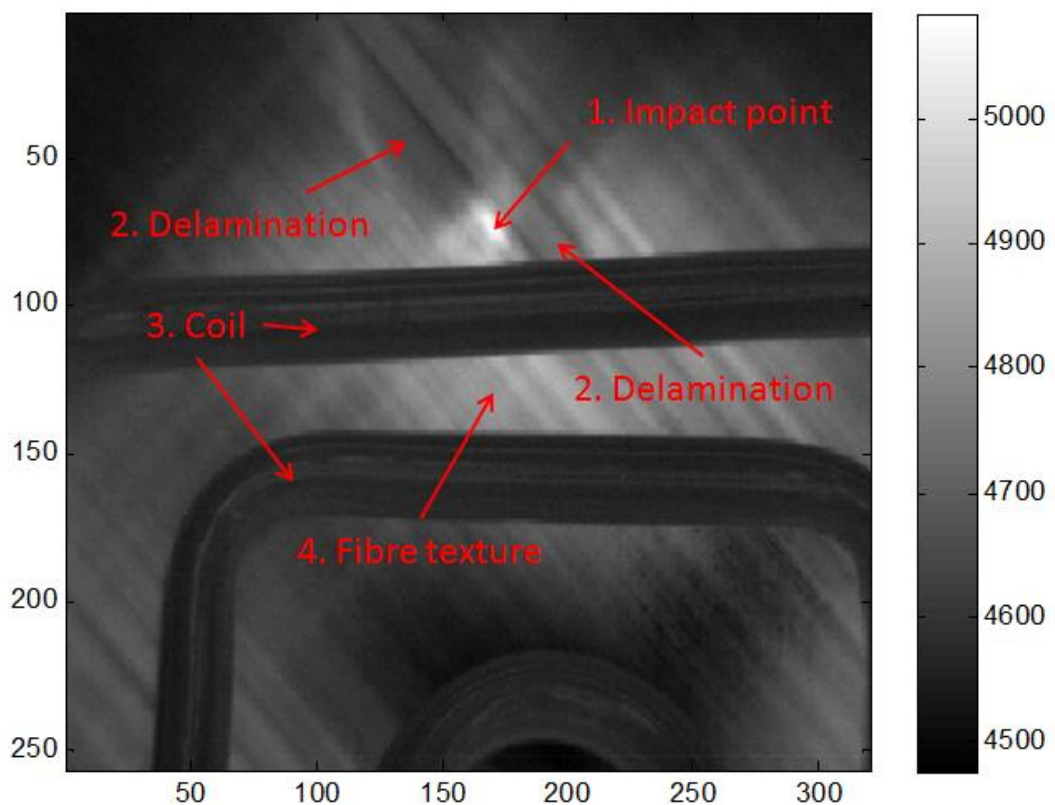


Figure 6.4 Thermal image on the back side of the impact damage sample (sample set 2) at 200ms, reflection mode.

An assumption of independent 'heat sources' contributed to the thermal video is given such as impact point, delamination, coil, fibre texture *etc.*, in Figure 6.4. From Figure 6.4, a hot-spot at the impact point and two dark areas at delaminations, marked as region 1 and 2 respectively can be seen. The coil is in the dark region 3, since the

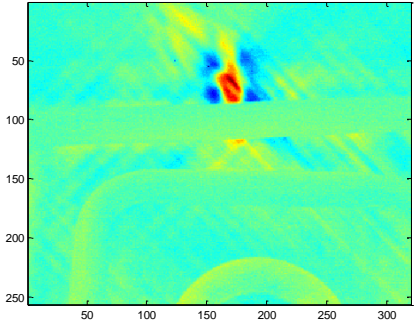
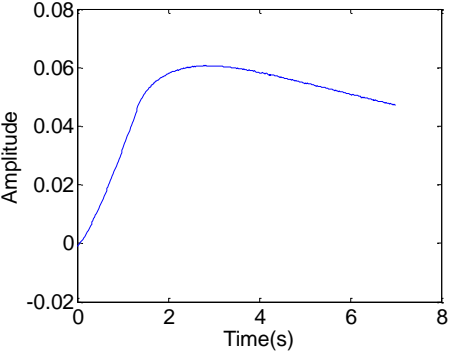
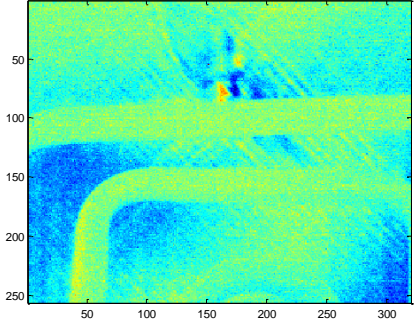
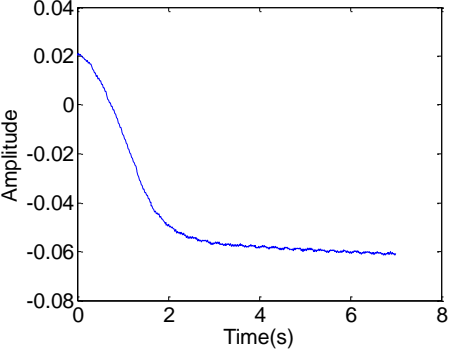
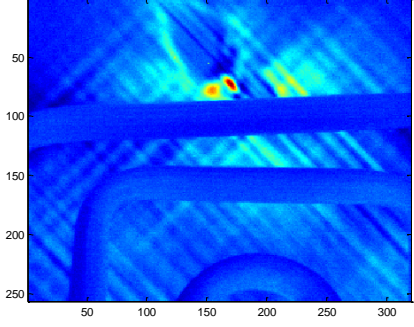
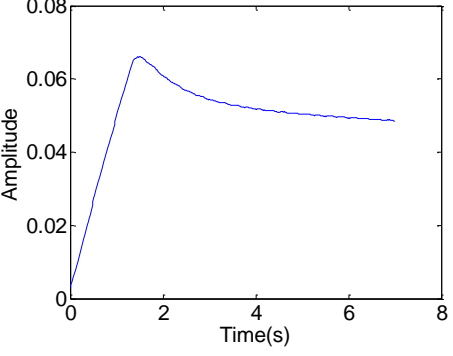
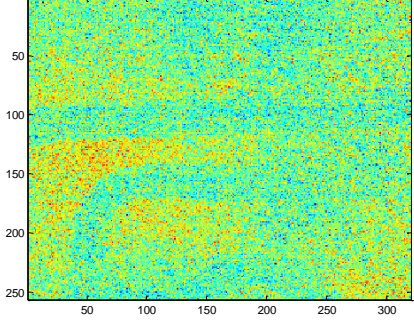
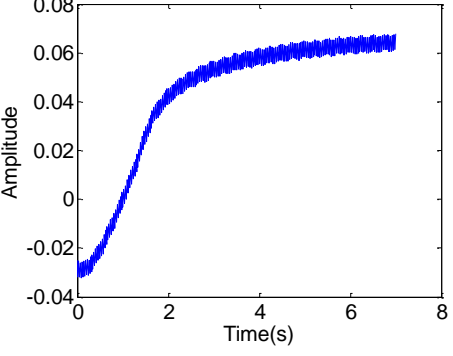
heating of the sample is more than that of the coil. Besides this, the gratings in white show the fibre texture, as marked in region 4. From the thermal images, the fibre orientations in the first and second layers are  $-45^\circ$  and  $45^\circ$ , respectively.

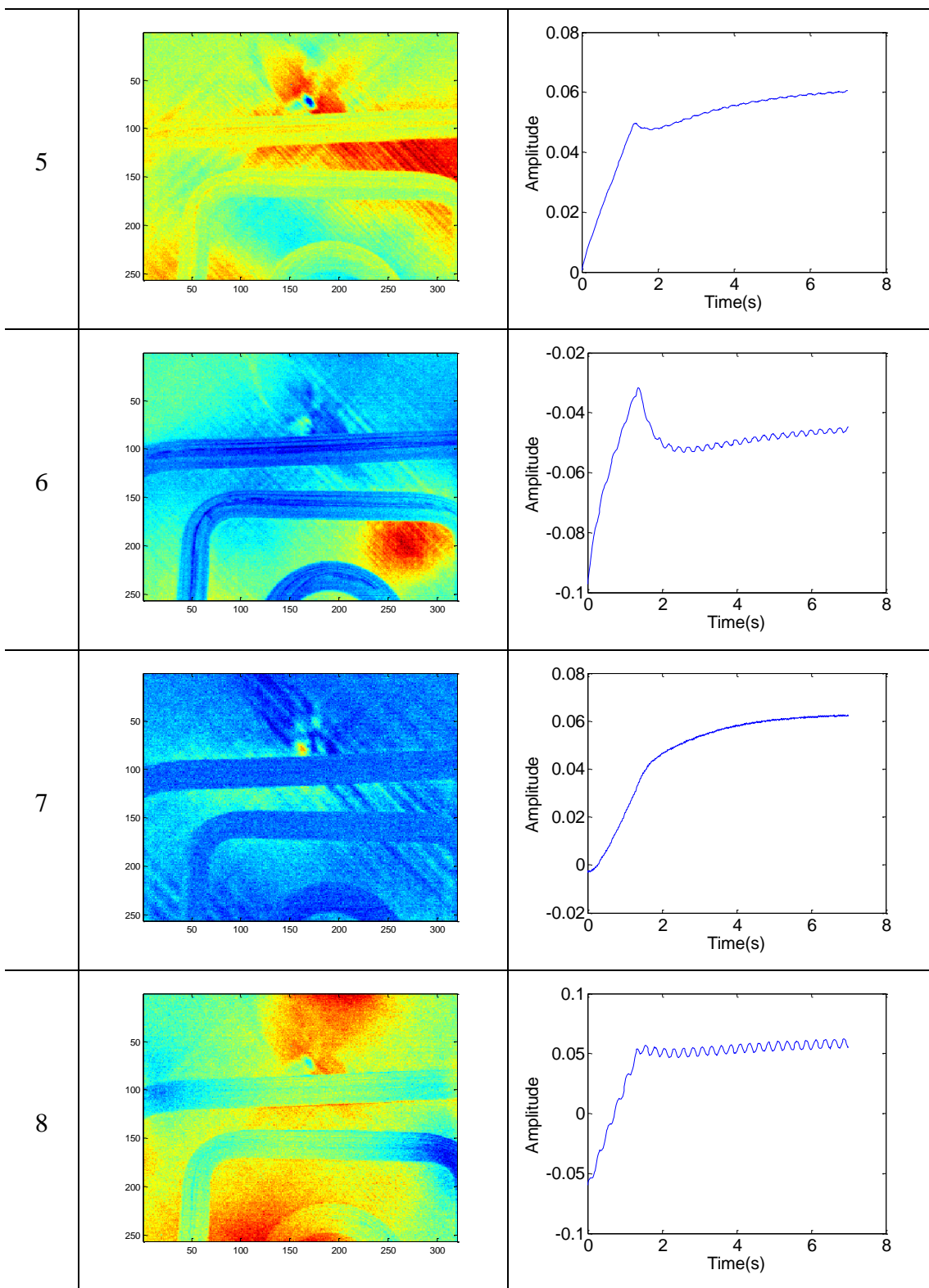
The first eight ICs and their mixing vectors using MMCA are listed in Table 6-I.

In Table 6-I, it can be seen that the impact damage and the resulting delamination are separated using ICA, whilst they were not separated using PCA as shown in Section 6.1.2. IC1 highlights the impact point, shown as region 1 in Figure 6.4, and IC3 highlights the delamination edge, marked as region 2 in Figure 6.4. The time-to-peak value in mixing vectors 1 and 3 reflects the depth where the heat propagates from the defect towards rear surface of the sample. Because of the different values of time-to-peak in the mixing vectors 1 and 3, the depth information can be estimated due to the proportional relationship between square root of time-to-peak and the depth. It can be concluded that the delamination is near to the rear surface of the sample and the impact damage is far away from the rear surface.

To understand the other ICs, a reference study using the same sample but different coil positions is undertaken. The reference thermal video only records the heating and cooling in the defect-free area, in order to compare the ICs with and without defects. The coil positions are shown in Figure 6.5. The thermal video for the ICA investigation in Table 6-I is called the 'impact' video and the reference thermal video is named the 'non-defect' video. Therefore, the 'impact' video contains the heating and cooling responses at the coil, defect-free area (non-defect) and defect, whilst the 'non-defect' video only includes those at the coil and defect-free area.

Table 6-I MMCA results for impact damage, rear side of sample set 2: the first eight ICs and their mixing vectors

#	ICs	Mixing vector
1		
2		
3		
4		



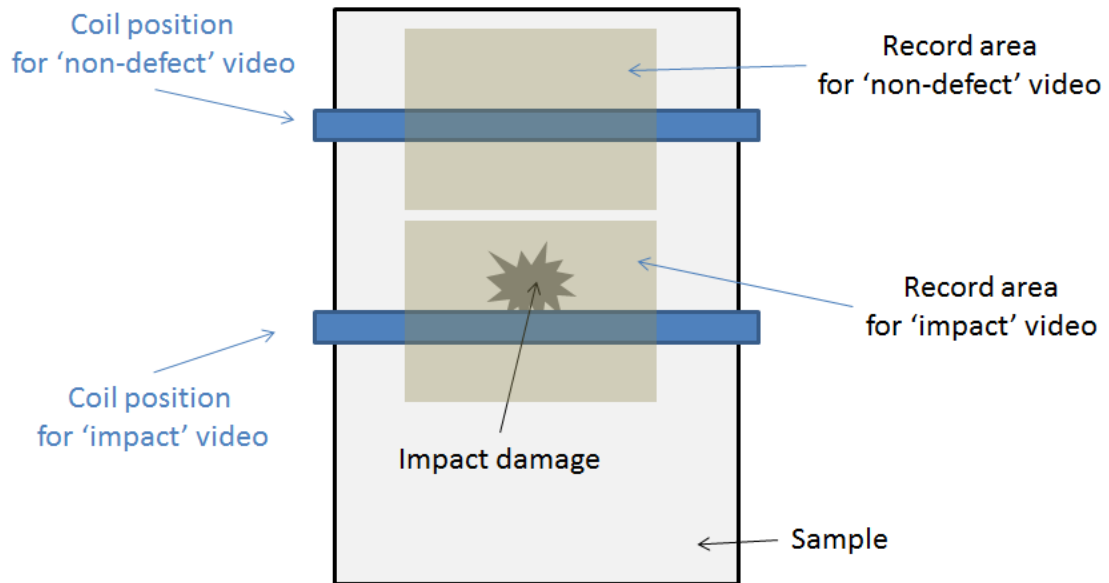


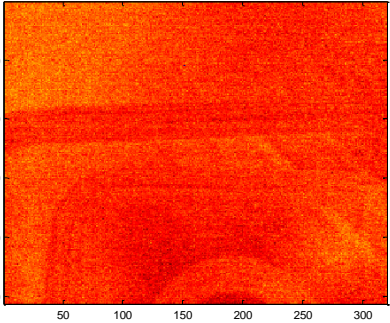
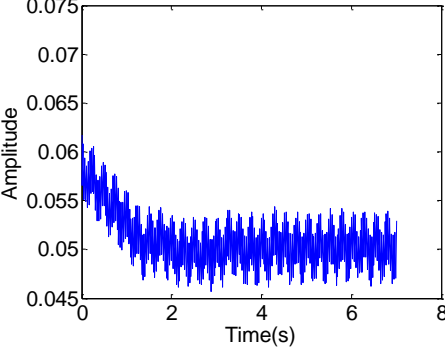
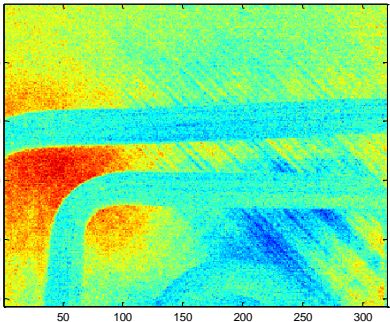
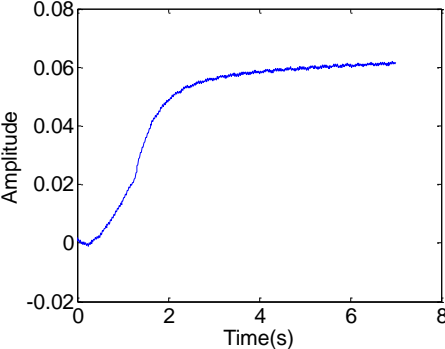
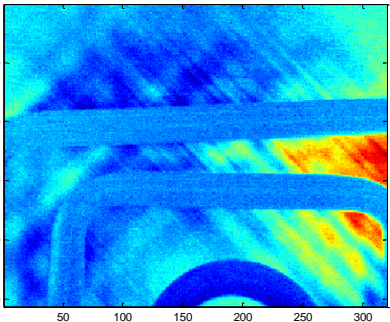
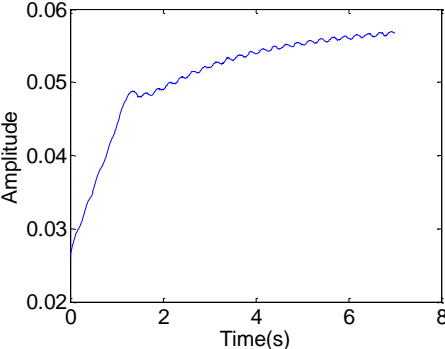
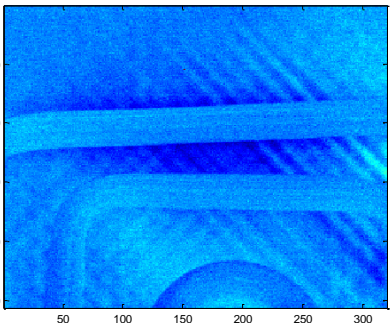
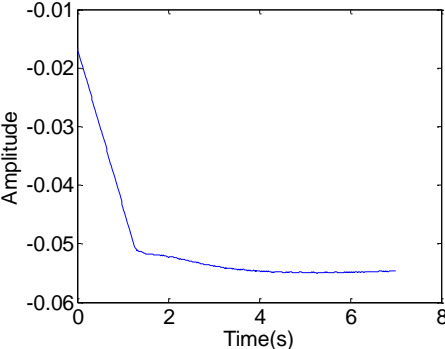
Figure 6.5 Coil positions and recorded areas for 'impact' and 'non-defect' videos

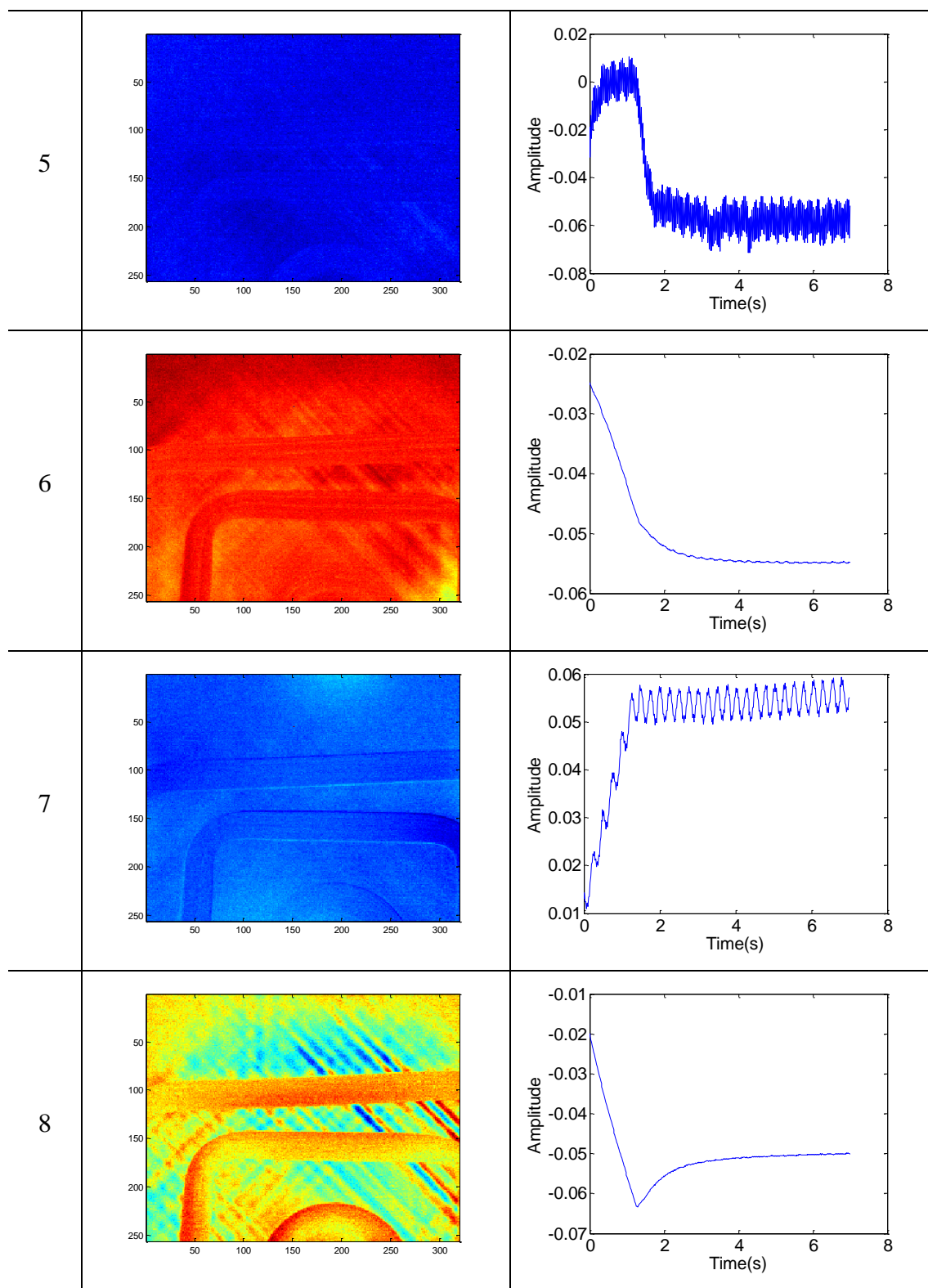
Using the same calculation procedure as the 'impact' video, the first eight ICs and corresponding mixing vectors for the 'non-defect' video are derived and listed in Table 6-II.

It can be seen that the ICs and mixing vectors calculated from the “impact” video includes the defects and non-defect information, and those derived from the “non-defect” video only contains the non-defect information. Thus, similar ICs or mixing vectors show the factors from non-defect which contribute to the thermal videos, including light reflection, and the influence of the coil and fibre texture; whereas different ICs or mixing vectors give information about the defects. To compare the two videos, cross-correlations between any pair of their mixing vectors are calculated and summarised in Table 6-III.



Table 6-II MMCA results for 'non-defect' video, rear side of sample set 2: the first eight ICs and their mixing vectors

#	ICs	Mixing vector
1		
2		
3		
4		



From Table 6-III, it can be seen that the mixing vectors 1, 3 and 6 of the 'impact' video (mv\_imp1, 3, and 6) have no correlation with any of those for the 'non-defect' video. It shows the unity of these three mixing vectors containing defective information where none of the mixing vectors from the 'non-defect' video do. As discussed before, mv\_imp1 and 3 reflect the impact damage and delaminations respectively. In addition,

mv\_imp6 illustrates the reflection of nature lights rather than any defect on the red region in IC6 of 'impact' video. Therefore, mv\_imp1 and 3 can be used in reconstructing the video to demonstrate the transient patterns from impact damage and delamination respectively, which can then be used to improve the ECPT investigation at the local area level in the future work. Meanwhile, IC1 and IC3 from the 'impact' video can guide pixel selection for the ECPT investigation at the pixel level.

Table 6-III Cross-Correlation between the mixing vectors from the 'impact' and the 'non-defect' videos

mv_imp \ mv_bg	1	2	3	4	5	6	7	8
1	-0.597	0.891	0.872	-0.951	-0.786	-0.955	0.917	-0.733
2	0.592	<b>-0.991</b>	-0.969	0.958	0.886	<b>0.990</b>	-0.907	0.557
3	-0.544	0.611	0.700	-0.852	-0.465	-0.785	0.867	-0.966
4	-0.473	<b>0.993</b>	0.963	-0.924	-0.851	-0.965	0.860	-0.474
5	-0.582	0.939	<b>0.996</b>	-0.980	-0.774	-0.980	0.940	-0.664
6	-0.470	0.487	0.703	-0.778	-0.258	-0.678	0.799	-0.922
7	-0.573	<b>0.991</b>	0.981	-0.941	-0.878	-0.976	0.886	-0.503
8	-0.603	0.893	0.953	<b>-0.992</b>	-0.731	-0.974	0.967	-0.786

(mv\_imp denotes the mixing vectors from the 'impact' video; mv\_bg stands for the mixing vectors from the 'non-defect' video. The correlation value above 0.99 means that two mixing vectors are cross-correlated)

### 6.3 Chapter summary

In this chapter, the ECPT investigation at pattern level using PCA and ICA has been reported.

From the PCA processing on the thermal sequence with three types of defects, it can be found out that PCA can enhance the abnormal regions caused by defects and reduce the dimension of data. This allows us to identify and classify the defects through the

---

extracted patterns. However, PCA only works well if sources are Gaussian and it cannot guarantee the independence of the separated patterns. On the other hand, the influence of different defects, fibre texture and other factors are not necessarily orthogonal. Consequently, they are not completely separated, and inevitably make it difficult to classify the defect type for each PC.

MMCA algorithm concentrates on the sparse representation and independence whereas highly matches the situation with defects in the CFRP samples. Therefore, the proposed defect detection has been achieved. Comparing the results of PCA and MMCA for the sample with impact damage and delamination, MMCA can not only separate the influences from defect and non-defect such as fibre texture, but also discriminate those defects into different ICs and also show the depth information from the time-to-peak values in the mixing vectors. This allows the reconstruction of video using individual mixing vectors to investigate the impact damage and delamination along with depth/layer information in the future work.

## **Chapter 7. CONCLUSION AND FUTURE WORK**

In this chapter, the research work presented in previous chapters is summarised, and the contribution of the study to research in eddy current pulsed thermography for composites is highlighted. Based on the research outcomes, recommendations are made for further work.

### **7.1 Conclusion**

This thesis focuses on research into the simulation and experimental study of eddy current pulsed thermography (ECPT) for defect detection and characterisation in carbon fibre reinforced plastic (CFRP), which is one of the major materials used in wind turbine blades. The thesis includes an extensive literature survey on failure models for composite-based wind turbine blades, the state-of-the-art of NDT&E techniques used for composite materials, and the interpretation and characterisation algorithms for the proposed ECPT technique, as well as challenges and problems identification with the proposed solution are discussed. The theoretical basis of ECPT techniques is considered, including Maxwell's equations, heat diffusion equations and EM-thermal coupling; and numerical modelling and an experimental system are developed for ECPT including the re-design of directional excitation for non-homogeneous and anisotropic composites, as well as appropriate algorithms for interpretation and characterisation. Three investigations are implemented for defect detection, classification and characterisation, according to defect location and the complexity of fibre textures: (1) an ECPT investigation at the pixel level is conducted, based on transient temperature responses and their feature extraction for crack quantification and defect classification; (2) an ECPT investigation at the local area level is carried out using optical flow patterns for defect classification, QNDE for defect through counting pixel number above selected threshold, and evaluation of directional physical properties via directional flow

amplitudes; (3) an ECPT investigation at the pattern level is conducted using PCA and ICA for the evaluation of patterns associated with the three types of defects, as well as to discriminate between multiple defects. A summary of the outcome of each investigation is given in detail below.

### ***7.1.1 Failure models and state-of-the-art of NDE for composite blades***

Wind turbine blades made of composites have relatively long downtimes compared to other wind turbine components, in spite of low failure rates. This means that the failure of wind turbine blades hinders electric generation during repair or maintenance. Thus, early awareness of potential damage and its status with the help of NDE techniques for condition-based operation and maintenance is extremely important. Blade failure is mainly caused by cracks, delaminations and impact damage which may lead to the final collapse of the blades. Therefore, the evaluation of the generation and propagation of those defects needs to be undertaken.

From the review of NDE techniques for composites, it is clear that each technique has advantages and disadvantages. Ultrasonics can be used to inspect a relatively large area, however a couplant is normally required which is not always appropriate. Acoustic emission techniques can detect the generation and propagation of defects in online and in-situ monitoring, but it is difficult to obtain quantitative information about the defects. Fibre optics is good for monitoring the large scale of blades, but the signal is strongly influenced by other factors such as strain, temperature *etc.* Eddy current or magnetic flux leakage methods are sensitive to surface and sub-surface defects, but deeper defects are difficult to detect due to skin effects. Microwave methods provide a means for fast inspection and visualisation with high sensitivity and resolution for dielectric material, but microwaves cannot efficiently penetrate through conductive materials. This means that surface defects can be sensed but it is difficult to detect deeper defects. The major advantage of thermography over other techniques is the potential for the rapid inspection of a large area within a short period of time, even though it has so far been mostly applied to samples in the laboratory rather than in-situ structures. Among thermographic techniques, eddy current pulsed thermography is a non-contact approach which concentrates heat generation at defects not only at the surface but also under the surface of inspected specimens. It allows large contrast to be produced between defective regions and defect-free areas, which is useful for defect detection and characterisation with an optimised directional excitation.

The interpretation and characterisation algorithms used in ECPT techniques are mainly based on transient thermal responses and their features, which allow the quantification of defects at pixel level. Few algorithms have been proposed which take into account the non-homogeneity of composite materials at the local area or pattern level. A comprehensive algorithm to deal with various defect types in different fibre textures is required for effective defect detection and characterisation.

### ***7.1.2 Numerical modelling and the experimental system***

COMSOL Multiphysics is chosen for numerical modelling of EM-thermal interaction. With a defined excitation current density in COMSOL, the magnetic vector potential  $\bar{A}$  can be derived via equation (3.14). Then the EM variables are calculated from  $\bar{A}$ . The link between induction currents and heat transfer is the resistive heating  $Q$ , which can be derived from equation (3.15). Finally, the temperature distribution  $T$  can be solved in 'heat transfer' module via equation (3.16).

An experimental system is developed and redesigned for non-homogeneous and anisotropic composite materials. Directional excitation is implemented to maximise the heating in the selected orientation, for example along the fibre orientation, in order to enhance the contrast between defective regions and defect-free areas. Samples with man-made crack and delamination, low-energy impact damage are manufactured for the investigation of those three types of defects. Different fibre textures are also prepared for the investigation of non-homogeneous and anisotropic conditions, including uni-directional, multiple-directional and woven fibre structures.

### ***7.1.3 ECPT investigation at the three levels***

Three investigations at the pixel level, local area level and pattern levels are developed and implemented for different defect locations and fibre textures. In the investigations, the challenges associated with following problems are addressed: (1) the non-homogenous and anisotropic properties and the multiple-layered structure of CFRP materials; (2) the detection and classification of different types of defects at the surface

or inside the sample; and (3) quantitative non-destructive evaluation (QNDE) of different defects and in varied fibre textures.

Table 7-I shows the results concerning the comparison of advantages and disadvantages of the investigations at the three levels, and following conclusions can be drawn. The pixel level is efficient for surface cracks, in particular within uni-directional fibres; whereas the local area level has advantages for identifying delamination and impact damage in specimens with multiple fibre orientation; whilst the pattern level is good for separating the influence from defects, coil, fibre texture and others. From the comparison, it can be seen that both the local area and pattern levels can be used for complex fibre textures. The detection and characterisation ability from the pixel level towards the pattern level is increased in terms of defect depth. Only the pattern level can separate multiple defects. As a trade-off, the computational complexity involved also increases. This requires the selection of an appropriate level of investigation for each inspection situation. The outcomes of the investigation at each level are summarised below.

Table 7-I Comparison and merits of three investigation levels

	Pixel level	Local area level	Pattern level
Defect location	Surface defects	Surface and inner defects	Surface and inner defects
Fibre texture	Uni-directional	Uni-directional, multi-directional	Uni-directional, multi-directional, woven structure
Ability to detect multiple defects	Not good	Not good	Good
Computation complexity	Low	Medium	High



### 7.1.3.1. Investigation at the pixel level

The advantages and disadvantage of the ECPT investigation at pixel level are that it achieves good QNDE results for surface cracks in simple fibre textures (uni-directional fibre), but it is not accurate when the fibre texture becomes complex and/or if the defect is not on the surface of the sample.

From the case study of cracks, it is found that the relationship between the crack depth and transient temperature change shows that a deeper crack leads to a greater temperature rise at the bottom of the crack. A deeper crack results in a faster normalised temperature decay rate in the cooling phase, but the normalised transient temperature behaviour in the heating phase is not affected. The results also show that a narrower crack leads to not only a greater temperature rise, but also faster rates of temperature rise and decay at the beginning of the heating phase and in the cooling phase respectively.

From the case study of impact damages, the following conclusions can be drawn. Firstly, electrical conductivity  $\sigma$  and thermal conductivity  $k$  determine the temperature response in the heating and cooling phases respectively, which enables the separation of  $\sigma$  and  $k$  by using the first derivative of the temperature responses in the heating and cooling phases as two features. Secondly, a larger decrease in  $\sigma$  leads to a rapid temperature rise in the heating phase, while a larger decrease in  $k$  leads to a slower temperature decrease in the cooling phase. Thirdly, as the impact energy increases, if not enough to produce a surface crack, the electrical conductivity in the impact area decreases but thermal conductivity there increases.

From the classification of crack, delamination and impact damage via PCA, the first two weighted PCs of the transient temperature responses are calculated for defect classification.

### 7.1.3.2. Investigation at the local area level

The advantages and disadvantage of the ECPT investigation at the local area level are found to be that, firstly, it achieves relatively good QNDE results for deeper defects such as impact damage) in complex fibre textures. Secondly, the three types of defect

can be classified according to the flow patterns at the defective region. However, thirdly, it is not accurate in separating the influence of fibre texture from that of the defect when fibre texture is complex.

From the case study of defect classification, it is found that the flow patterns at the local area of the defect are different for crack, impact damage and delamination. This is because the variations in directional electric or thermal conductivity for different types of defects are not the same. This allows defects to be classified using the OF patterns, which can be summarised as follows. For the case of cracks, the flow is mainly diverted from the bottom of the crack, and some of the flows go around the crack interface. For the case of impact damages, the flow spreads from the impact point to all surrounding directions. But with delamination, the flow mainly propagates around the edge of the delamination.

Through the case study of QNDE, impact damages can be quantified in terms of the area of defects against impact energy, by extracting the pixel number of OF above the selected threshold. The results showed that  $PN_{OF}$  increases as the impact energy increases.

Due to the complex fibre texture of the impact damage samples, the amplitudes in either the horizontal or vertical directions are difficult to determine accurately. A uni-directional sample is used for the evaluation of directional property variation in the case study on uni-directional samples under tensile stress. The results showed that the OF amplitude parallel to the tensile direction increases as the tensile stress increases (*i.e.* the electrical conductivity increases).

#### 7.1.3.3. Investigation at the pattern level

PCA and ICA are implemented for the pattern-level investigation. From the PCA processing of the thermal sequence with the three types of defects, it is found that PCA can enhance the abnormal regions caused by defects and reduce the dimension of the data. This allows defects to be classified according to their different patterns. There are two problems with the use of PCA, however. On one hand, the representation of linear combinations of PCs is not accurate for non-linear data, and On the other hand, the

influence of factors such as the interaction of eddy currents with defects, and heat propagation along the fibre and at defects is not necessarily orthogonal.

To overcome the problems with the use of PCA, ICA is then applied. Multichannel morphological component analysis (MMCA) as one of typical ICA algorithm has been chosen for this non-linear problem, because of its advantage of sparse representation which matches the situation with defects in CFRP samples. Comparing the results from PCA and ICA of impact damage, ICA can separate multiple defects such as impact damage and delamination into different ICs and also provides depth information from the time-to-peak value in the mixing vectors.

In real application, the selection of different investigation levels can follow the steps below, shown in Figure 7.1: (1) if there are clear hot-spots, it means the defect is on the surface. Then the pixel level is selected; (2) if there are any clear flow patterns for typical defect, the local area level is selected. Otherwise, the pattern level is selected.

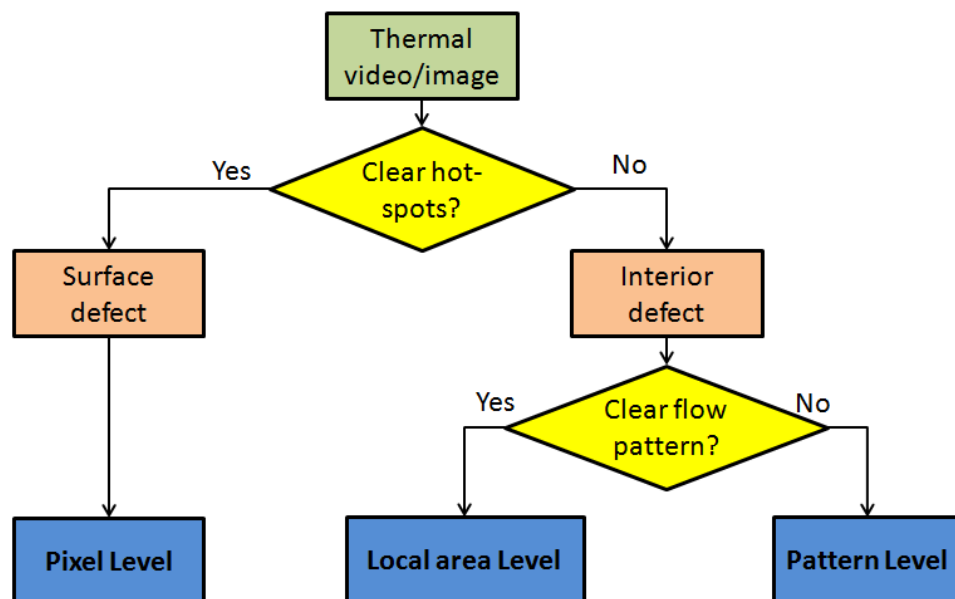


Figure 7.1. Flow chart for selection of investigation levels

## 7.2 Future work

Following the research outcomes which have been achieved in this study, several directions for future work can be suggested in terms of system refinement and reduction in size, automation of defect identification and characterisation, and the 3D reconstruction of defects and material properties.

### *7.2.1 System refinement and reduction in size for online monitoring*

In the current system, the thermal video is recorded using the commercial software Altair provided by FLIR, and the video data is imported to Matlab for further investigation. This does not satisfy the requirements of online monitoring. The interface between the IR camera and Matlab should be built based on FLIR SC7500 SDK for Matlab, so that video acquisition and post-processing can be achieved simultaneously.

The current experimental system is designed for laboratory studies, which is relatively expensive and unwieldy to use in real applications. Therefore, reductions of both the cost and dimensions of the system are required. This should include coil design for specific specimens, such as a flexible coil for use with the complex geometry of objects to be inspected. Also a fixed power and carrier frequency for the induction heater should be based on the numerical simulation for real applications in order to reduce costs. Furthermore, user-friendly IT tools for automatic defect identification and characterisation are needed, and Figure 7.2 shows a demonstration Graphic User Interface (GUI) program which could be used to load the thermal video/images, conduct investigations at the pixel and local area levels for transient response and flow plots, as well as applying the Fourier Transform to video, and performing noise reduction, *etc.* User-friendly IT tools will allow the updating of real-time thermal video acquisition and display, the automatic identification of abnormal regions, and defect classification with the automatic selection of investigation level based on such a version.

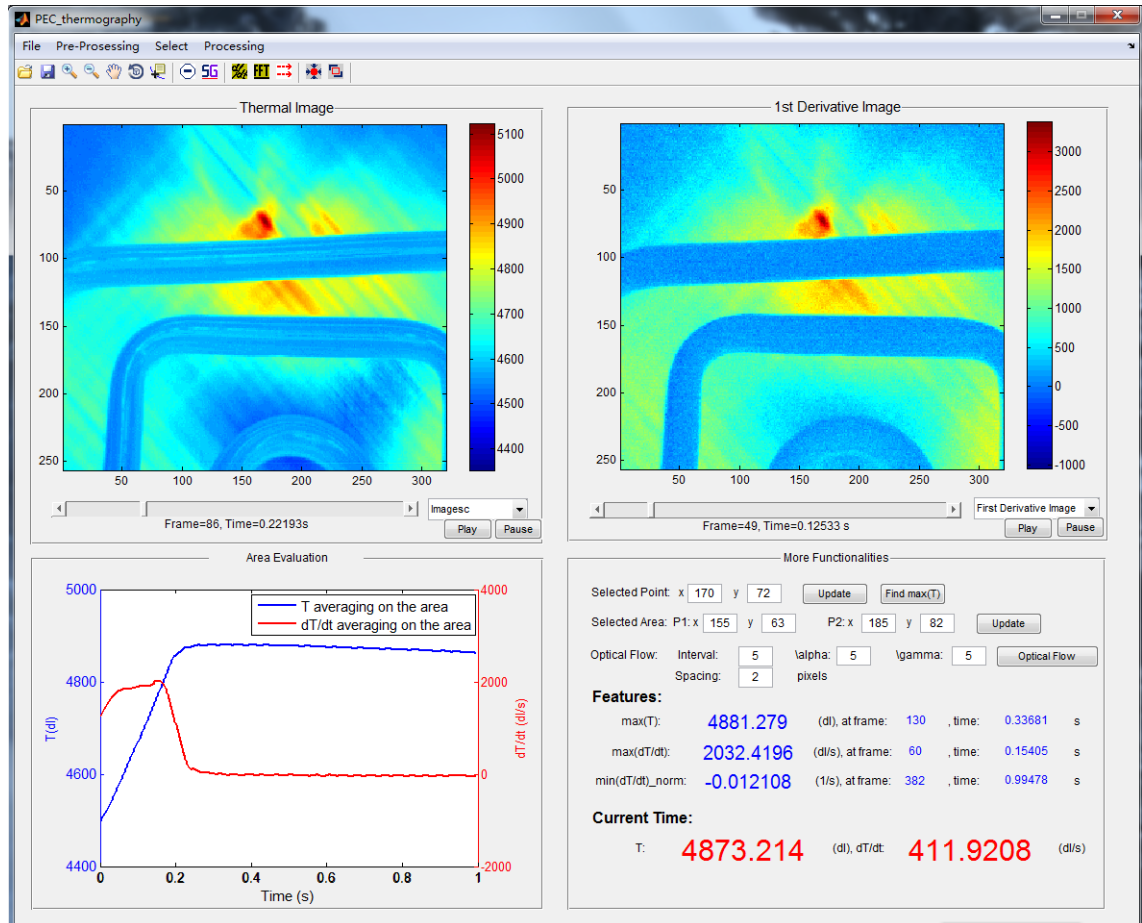


Figure 7.2 Matlab GUI for thermal video display and processing

### 7.2.2 Automatic defect identification and characterisation

The current defect identification and characterisation algorithms at the pixel, local area and pattern levels are all human-supervised. This requires experienced staff capable of choosing the appropriate Region of Interest (ROI) from the thermal video when the IR camera and specimen are fixed.

To adapt the ECPT system for real applications, future work can be proposed as follows. First task is to undertake simulation modelling and experimental studies to extract invariant features and material characterisation at the pixel, local area and pattern levels when the IR camera and/or specimen inspected are in motion. Second task is to investigate data reduction methods for on-line monitoring, including feature extraction from randomly selected thermal images or a specific short time-slot from the on-line thermal video without losing any information about the defect and material status.

Identification of the minimum thermal images required for feature extraction should be also investigated. An automatic selection of investigation is to be developed at the pixel, local area or pattern levels based on the material status in order to reduce calculation costs. Furthermore, appropriate models are to be developed for ICA in order to maximise the invariance of ICs denoting the different defects in line with the physical model of the ECPT in composites.

### ***7.2.3 3D reconstruction of defects and material properties***

The current investigation has only considered the surface temperature profile. This means that the investigation is at the 2D level. Future work should involve the 3D reconstruction of defects and material properties from heat diffusion and propagation data in line with analytical and numerical modelling with the time slides of thermal generation and propagation. Since numerical modelling allows information about temperature distribution and variations against time inside the specimen to be obtained, 3D optical flow, divergence of temperature and PCA/ICA on 4D temperature response ( $x$ ,  $y$ ,  $z$  and time dimensions) can be investigated to validate the experimental estimation. In this way, cases with varying interior defects will be simulated to match the experimental results for the reconstruction of actually 3D shape of defects. The time-to-peak values obtained from either transient thermal responses or PCA/ICA results can be used to reconstruct the information in each layer. The contribution to the surface temperature profile made by the interior temperature distribution and its variation can then be evaluated for inverse problem and the prediction for 3D reconstruction.

---

**LIST OF REFERENCES**

- [1] G. N. Tiwari and M. K. Ghosal, “Renewable energy resources: basic principles and applications”, ISBN 1-84265-125-0, Alpha science international Ltd, pp. 381-383, 2005
- [2] H. L. Hess, N. A. A. Melek and E. Muljadi, “Power Converter for Wind Turbine Application”, *IEEE Power Engineering Society Summer Meeting*, vol. 2, pp. 1275–1276, Jul 2000
- [3] P. J. Tavner, J. Xiang and F. Spinato, “Reliability analysis for wind turbines”, *Wind Energy*, vol. 10, No. 1, pp. 1-18, 2007
- [4] P. J. Tavner, “Wind energy session report”, *UK-China Clean Energy Event*, The Royal Society, London, Mar 2004
- [5] D. J. Lekou, P. Vionis, P. A. Joosse, D. R. V. van Delf, D. Kouroussis, A. Anastassopoulos, M. J. Blanch, A. G. Dutton, “Full-scale blade testing enhanced by acoustic emission monitoring”, *Proc. European Wind Energy Conference (EWEC 2003), Madrid, Spain, Jun 2003*
- [6] J. Paquette, J. van Dam and S. Hughes, “Structural testing of 9 m carbon fiber wind turbine research blades”, *AIAA 2007 Wind Energy Symposium*, Reno, USA, NREL/CP-500-40985, Jan 2007
- [7] J. van Dam, E. Jacobson, H. Link and M. Meadors, “wind turbine generator system duration test report for the atlantic orient 15/50 wind turbine”, <http://www.nrel.gov/wind/pdfs/34017.pdf>, Apr 2003
- [8] B. F. Sørensen, E. Jørgensen, C. P. Debel, F. M. Jensen, H. M. Jensen, T. K. Jacobsen and K. M. Halling, “Improved design of large wind turbine blade of fibre composites based on studies of scale effects (Phase 1) Summary Report”, Risø-R-1390(EN)/ ISBN 87-550-3176-5, Risø National Laboratory, Denmark, 2004
- [9] W. Musial, S. Butterfield and B. McNiff, “Improving wind turbine gearbox reliability: preprint”, *European Wind Energy Conference*, Milan, Italy,

- NREL/CP-500-41548, May 2007, available at <http://www.nrel.gov/wind/pdfs/41548.pdf>
- [10] S. Polak, “Gearbox & Gear System problems”, available at <http://www.tribology.co.uk/publish/p004.htm>
- [11] P. J. Tavner, “Review of condition monitoring of rotating electrical machines”, *IET Electric Power Applications*, vol. 2, No. 4, pp. 215-247, 2008
- [12] Z. Hameed, Y.S. Hong, Y.M. Cho, S.H. Ahn and C.K. Song, “Condition monitoring and fault detection of wind turbines and related algorithms: A review”, *Renewable and Sustainable Energy Reviews*, vol. 13, pp. 1-39, 2009.
- [13] J Ribrant, “Reliability performance and maintenance—a survey of failures in wind power systems”, Master thesis, KTH School of Electrical Engineering, Sweden, 2005/2006
- [14] M. L. Flemming and S. Troels, “New lightning qualification test procedure for large wind turbine blades”, *Int. Conf. Lightning and Static Electricity*, Blackpool, UK, pp 36.1–10, 2003
- [15] P. Tavner, *Offshore wind turbines: reliability, availability and maintenance*, IET, ISBN: 978-1-84919-229-3, 2012
- [16] D. J. Wilkins, “The Bathtub Curve and Product Failure Behavior”, *Reliability HotWire eMagazine*, Issue 21, 2002, available at <http://www.weibull.com/hotwire/issue21/hottopics21.htm>
- [17] D. McMillan and G. W. Ault, “Condition monitoring benefit for onshore wind turbines: sensitivity to operational parameters”, *IET Renewable Power Generation*, vol. 2, Issue 1, pp. 60-72, 2008
- [18] S. Ebersbach, Z. Peng and N.J. Kessissoglow, “The investigation of the condition and faults of a spur gearbox using vibration and wear debris analysis techniques”, *Wear*, vol. 260, Issues 1-2, pp. 16-24, 2006
- [19] <http://www.ndt.net/>
- [20] Fu-Kuo Chang, W. H. Prosser and M. J. Schulz, “Editorial: Letter of introduction from the editors of structural health monitoring” *Structural Health Monitoring*, vol. 1, pp. 3-4, 2002
- [21] P. A. Joosse, M. J. Blanch, A. G. Dutton, D. A. Kouroussis, T. P. Philippidis and P. S. Vionis, “Acoustic emission monitoring of small wind turbine blades”, *Proc. 21st ASME Wind Energy Symp. in conjunction with 40th AIAA Aerospace Sciences Meeting*, Reno, USA, AIAA-2002-0063, pp. 1–11, 2002



- [22] A. G. Beattie, “Acoustic emission monitoring of a wind turbine blade during a fatigue test”, *ASME Wind Energy Symposium/AIAA Aerospace Sciences Meeting*, Reno, USA, pp. 239-248, 1997
- [23] M. A. Rumsey, J. Paquette, J. R. White, R. J. Werlink, A. G. Beattie, C. W. Pitchford and J. van Dam, “Experimental Results of Structural Health Monitoring of Wind Turbine Blades”, <http://www.sandia.gov/wind/asme/AIAA-2008-1348.pdf>
- [24] E. R. Jørgensen, K. K. Borum, M. McGugan, C. L. Thomsen, F. M. Jensen, C. P. Debelog and B. F. Sørensen, “Full scale testing of wind turbine blade to failure - flapwise loading”, Risø National Laboratory, Risø-R-1392(EN), Roskilde, Denmark, Jun 2004
- [25] E. Jasiūnienė, R. Raišutis, R. Šliteris, A. Voleišis and M. Jakas, “Ultrasonic NDT of wind turbine blades using contact pulse-echo immersion testing with moving water container”, *Ultragarsas (Ultrasound)*, vol.63, No.3, pp. 28-32, 2008
- [26] E. Jasiūnienė, R. Raišutis, R. Šliteris, A. Voleišis, A. Vladisauskas, D. Mitchard and M. Amos, “NDT of wind turbine blades using adapted ultrasonic and radiographic techniques”, *Insight*, vol. 51, No. 9, pp. 477-483, 2009
- [27] P. Sendrup, “Fundamentals for remote structural health monitoring of wind turbine blades – a Preproject: Annex C - Fibre transducer for damage detection in adhesive layers of wind turbine blades”, Risø-R-1342(EN), Risø National Laboratory, 2002
- [28] S. Park, G. Park, C. B. Yun and C. R. Farrar, “Sensor self-diagnosis using a modified impedance model for active sensing-based structural health monitoring”, *Structural Health Monitoring*, vol. 8, No. 71, pp. 71-82, 2009
- [29] M. J. Schulz and M. J. Sundaresan, “Smart sensor system for structural condition monitoring of wind turbines”, Subcontract Report NREL/SR-500-40089, National Renewable Energy Laboratory, 2006
- [30] G. Kister, D. Winter, R.A. Badcock, Y.M. Gebremichael, W.J.O. Boyle, B.T. Meggitt, K.T.V. Grattan and G.F. Fernando, “Structural health monitoring of a composite bridge using Bragg grating sensors. Part 1: Evaluation of adhesives and protection systems for the optical sensors”, *Engineering Structures*, vol. 29, Issue 3, pp. 440-448, Mar 2007

- [31] T. Ashwill, “Blade Technology Innovations for Utility-Scale Turbines”, Sandia National Laboratories, Aug 2006, available at <http://www.sandia.gov/wind/other/BladeTechInnovations-AWEA06.pdf>
- [32] M. Jureczko, M. Pawlak and A. Mezyk, “Optimisation of wind turbine blades”, *J. Mater. Process. Technol*, vol. 167, pp. 463–71, 2005
- [33] D. A. Griffin, “WindPact Turbine Design Scaling Studies Technical Area 1: Composite Blades for 80- to 120-Meter Rotor”, NREL Report No. SR-500-29492, March 2001
- [34] D. A. Griffin, T. Ashwill, “Alternative Composite Materials for Megawatt-Scale Wind Turbine Blades: Design Considerations and Recommended Testing”, *Journal of Solar Energy Engineering*, vol. 125, pp. 515-521, 2003
- [35] M.J. Sundaresan, M.J. Schulz and A. Ghoshal, “Structural health monitoring static test of a wind turbine blade”, *Subcontract Report NREL/SR-500-28719*, National Renewable Energy Laboratory, CO, USA, 2002
- [36] C.C. Ciang, J.-T. Lee and H.-J. Bang. “Structural health monitoring for a wind turbine system: a review of damage detection methods”. *Measurement Science and Technology*, vol 19, Issue 12, 122001, pp. 1-20, 2008
- [37] J.K. Kim, D.B. Mackay and Y.W. Mai, “Drop-weight impact damage tolerance of CFRP with rubber-modified epoxy matrix”, *Composites*, vol. 24, pp. 485-491, 1993
- [38] <http://www.chipsbooks.com/strchlth.htm>
- [39] [http://en.wikipedia.org/wiki/Life\\_cycle\\_assessment](http://en.wikipedia.org/wiki/Life_cycle_assessment)
- [40] M. A. Rumsey and J. A. Paquette, “Structural health monitoring of wind turbine blades”, Sandia national laboratories, <http://www.sandia.gov/wind/other/SPIE-2008-6933-14.pdf>, 2008
- [41] L. Lading, M. McGugan, P. Sendrup, J. Rheinlander and J. Rusborg, “Fundamentals for remote structural health monitoring of wind turbine blades— a preproject ANNEX B”, *Risø-R-1341(EN) Report* Risø National Laboratory, 2002
- [42] T.E. Michaels, B.D. Davidson, “Ultrasonic inspection detects hidden damage in composite”, *Advance Materials &Processes*, vol.14, pp.1295-1300, 1995
- [43] H. Kocznarech, “Ultrasonic detection of damage in carbon fibre reinforced plastics”, *J. of Composite Materials*, 29, pp.59-95, 1995

- [44] D.N. Alleyne and P. Cawley, "The interaction of Lamb waves with defects", *IEEE Transactions on Ultrasonics, Ferroelectrics and Frequency Control*, vol. 39, No. 3, pp. 381 – 397, 1992
- [45] H. Saito and I. Kimpara, "Evaluation of impact damage mechanism of multi-axial stitched CFRP laminate", *Composites Part A: Applied Science and Manufacturing*, vol. 37, Issue 12, pp. 2226–2235, 2006
- [46] N. Guo and P. Cawley, "The interaction of Lamb waves with delaminations in composite laminates", *J. Acoust. Soc. Am*, vol. 94, Issue 4, pp. 2240-2246, 1993
- [47] D. Tuzzeo and F. Lanza di Scalea, "Noncontact air-coupled guided wave ultrasonics for detection of thinning defects in aluminum plates", *Res. Nondestr. Eval.*, vol. 13, pp. 61–78, 2001
- [48] Y. Sohn and S. Krishnaswamy, "Interaction of a scanning laser-generated ultrasonic line source with a surface-breaking flaw", *J. Acoust. Soc. Am*. vol. 115 pp. 172–181, 2003
- [49] W. Gao, C. Glorieux and J. Thoen, "Laser ultrasonic study of Lamb waves: determination of the thickness and velocity of a thin plate", *Int. J. Eng. Sci.* vol. 41, pp. 219–228, 2003
- [50] C. Zuluage-Giraldo, D. Mba and M. Smart, "Acoustic emission during run-up and run-down of a power generation turbine", *Tribology International*, vol. 37, Issue 5, pp. 415-422, 2004
- [51] V. M. Baranov, E. Kudryavtsev, G. Sarychev and V. Schavelin, *Acoustic emission in friction*, Elsevier, ISBN-13: 9780080451503, 2007
- [52] A.G. Dutton, M. Blanch, P. Vionis, D. Lekou, D. R. V. van Delft and P. Joosse, "Acoustic emission monitoring during certification testing of wind turbine blades", *European Wind Energy Conference*, Copenhagen, Denmark, July 2001
- [53] A.G. Dutton, P. Vionis, D. Lekou, D.R.V. van Delft, P. Joosse, et al, "Acoustic emission condition monitoring of wind turbine rotor blades: laboratory certification testing to large scale in-service deployment", *Proc. European Wind Energy Conference (EWEC 2003)*, Madrid, Spain, Jun 2003.
- [54] G.R. Kiriker, V. Shinde, M.J. Schulz, A. Ghoshal, M. Sundaresan and R. Allemang, "Damage localisation in composite and metallic structures using a structural neural system and simulated acoustic emissions", *Mechanical Systems and Signal Processing*, vol. 21, No.1, pp. 280–297, 2006.
- [55] A. Ghoshal, W.N. Martin, M.J. Schulz, A. Chattopadhyay, W.H. Prosser and H.S. Kim, "Health monitoring of composite plates using acoustic wave

- propagation, continuous sensors and wavelet analysis", *Journal of reinforced plastics and composites*, vol. 26, No. 1, pp. 95–112, 2007
- [56] [http://en.wikipedia.org/wiki/Optical\\_fiber](http://en.wikipedia.org/wiki/Optical_fiber)
- [57] T.H.T. Chan, L. Yu, H.Y. Tam, Y.Q. Ni, S.Y. Liu, W.H. Chung and L.K. Cheng, "Fiber Bragg grating sensors for structural health monitoring of Tsing Ma bridge: Background and experimental observation", *Engineering Structures*, vol. 28, Issue 5, pp. 648-659, 2006
- [58] G. Kister, D. Winter, R.A. Badcock, Y.M. Gebremichael, W.J.O. Boyle, B.T. Meggitt, K.T.V. Grattan and G.F. Fernando, "Structural health monitoring of a composite bridge using Bragg grating sensors. Part 1: Evaluation of adhesives and protection systems for the optical sensors", *Engineering Structures*, vol. 29, Issue 3, pp. 440-448, 2007
- [59] D. Roach and K. Rackow, "Health monitoring of aircraft structures using distributed sensor systems", Sadia national laboratories.
- [60] W. J. B. Grouve, L. Warnet, A. de Boer, R. Akkerman and J. Vlekken, "Delamination detection with fibre Bragg gratings based on dynamic behaviour", *Composites Science and Technology*, vol. 68, Issue 12, pp. 2418-2424, 2008
- [61] K. Schroder, W. Ecke, J. Apitz, E. Lembke and G. lenschow, "A fibre Bragg grating sensor system monitors operational load in a wind turbine rotor blade", *Meas. Sci. Technol*, vol. 17, pp. 1167-1172, 2006
- [62] N. Takeda, "Characterization of microscopic damage in composite laminates and real-time monitoring by embedded optical fiber sensors", *International Journal of Fatigue*, vol. 24, Issues 2-4, pp. 281-289, 2002
- [63] W. Y. Cheng, S. Kanemoto, I. Komura and M. Shiwa, "Depth sizing of partial-contact stress corrosion cracks from ECT signals", *NDT&E International*, vol. 39, No. 5, pp. 374-383, 2006
- [64] Y. Hatsukade, A. Kosugi, K. Mori and S. Tanaka, "Detection of micro-flaws on thin copper tubes using SQUID-NDI system based on eddy current technique", *Physica C: Superconductivity*, vol. 426-431, Part 2, pp. 1585-1590, 2005
- [65] V. Sundararaghavan, K. Balasubramaniam, N. R. Babu and N. Rajesh, "A multi-frequency eddy current inversion method for characterizing conductivity gradients on water jet peened components", *NDT&E International*, vol. 38, Issue 7, pp. 541-547, 2005

- [66] Y. Li, T. P. Theodoulidis and G. Y. Tian, "Magnetic field-based eddy-current modeling for multilayered specimens", *IEEE Transactions on Magnetics*, vol. 43, No. 11, pp. 4010-4015, 2007
- [67] G. Y. Tian, A. Sophian, D. Taylor and J. R. Rudlin, "Pulsed eddy current system for dynamic inspection of defects", *Insight*, vol. 46, No. 5, pp. 256-259, 2004
- [68] M. S. Safizadeh, B. A. Lepine, D. S. Forsyth and A. Fahr, "Time-frequency analysis of pulsed eddy current signals", *Journal of Nondestructive Evaluation*, vol. 20, No. 2, pp. 73-86, 2001
- [69] X. E. Gros, "An eddy current approach to the detection of damage caused by low-energy impacts on carbon fibre reinforced materials", *Materials & Design*, vol. 16, Issue 3, pp. 167-173, 1995
- [70] Y. He, M. Pan, D. Chen and F. Luo, "PEC defect automated classification in aircraft multi-ply structures with interlayer gaps and lift-offs", *NDT&E International*, vol. 53, pp. 39-46, 2013
- [71] G. Mook, R. Lange, and O. Koeser, "Non-destructive characterisation of carbon-fibre-reinforced plastics by means of eddy-currents", *Composites Sci. Technol.*, vol. 61, pp. 865-873, 2001
- [72] W. Yin, P. J. Withers and A. J. Peyton, "Noncontact characterization of Carbon-Fiber-Reinforced Plastics using multifrequency eddy current sensors", *IEEE Transactions on Instrumentation and Measurement*, vol. 58, No. 3, pp. 738-743, 2009
- [73] A. Ruosi, M. Valentino, G. Peluso and G. Pepe, "Analysis of low-velocity impact damage in reinforced carbon fiber composites by HTS-SQUID magnetometers", *IEEE Transaction on Applied Superconductivity*, vol. 11, No. 1, pp. 1172-1175, 2001
- [74] C. Carr, D. Graham, J. C. Macfarlane and G. B. Donaldson, "SQUID-based nondestructive evaluation of carbon fiber reinforced polymer", *IEEE Transaction on Applied Superconductivity*, vol. 13, No. 3, pp. 196-199, 2003
- [75] M. Afzal and S. Udpa, "Advanced signal processing of magnetic flux leakage data obtained from seamless gas pipeline", *NDT&E International*, vol. 35, Issue 7, pp. 449-457, 2002
- [76] L. Udpa, S. Udpa and A. Tamburrino, "Adaptive wavelets for characterizing magnetic flux leakage signals from pipeline inspection", *IEEE Transactions on Magnetics*, vol. 42, Issue 10, pp. 3168-3170, 2006

- [77] M. Chen, Y. Sun, W. Lord, S. Nath and Y.K. Shin, "Pulsed RFEC probe response", *IEEE Transactions on Magnetics*, vol. 28, No. 2, pp. 1430-1433, 1992
- [78] S. Saha, S. Mukhopadhyay, U. Mahapatra, S. Bhattacharya and G.P. Srivastava, "Empirical structure for characterizing metal loss defects from radial magnetic flux leakage signal", *NDT&E International*, vol. 43, Issue 6, pp. 507-512, 2010
- [79] Y. Li, J. Wilson and G.Y. Tian, "Experiment and simulation study of 3D magnetic field sensing for magnetic flux leakage defect characterisation", *NDT&E International*, vol. 40, Issue 2, pp. 179-184, 2007
- [80] M. Gomez-Parra, P. Munoz-Condes, M.A.G. San Andres, F.J. Gonzalez-Fernandez, J. Carpio and R. Guirado, "Advanced maintenance of rail traction motors using a magnetic leakage flux technique", *IEEE Transactions on Industry Applications*, vol. 48, Issue 3, pp. 942-951, 2012
- [81] N.J. Diserens and S.P. Sullivan, "Simulation of a remote field eddy current detector in eccentric thin-walled non-ferrous tubes using a 3D finite-element program", *IEEE Transactions on Magnetics*, vol. 30, No. 5, pp. 3737-3740, 1994
- [82] Y. Li, G.Y. Tian and S. Ward, "Numerical simulation on magnetic flux leakage evaluation at high speed", *NDT&E International*, vol. 39, Issue 5, pp. 367-373, 2006
- [83] S. Kharkovsky and R. Zoughi, "Microwave and millimetre wave nondestructive testing and evaluation", *IEEE Instrumentation & Measurement Magazine*, pp. 26-38, 2007
- [84] J. Polivka, "An overview of microwave sensor technology", *High Frequency Electronics*, pp.32-42, April 2007
- [85] K. Bois, L. Handjojo, A. Benally, K. Mubarak and R. Zoughi, "Dielectric plug-loaded two-port transmission line measurement technique for dielectric property characterization of granular and liquid materials," *IEEE Transactions on Instrumentation and Measurement*, vol. 48, no. 6, pp. 1141-1148, 1999
- [86] B.K. Chung, "A convenient method for complex permittivity measurement of thin materials at microwave frequencies", *Journal of Physics D: Applied Physics*, vol. 39, pp.1926-1931, 2006
- [87] K. Arunachalam, V.R. Melapudi, L. Udpa and S.S. Udpa, "Microwave NDT of cement-based materials using far-field reflection coefficients", *NDT&E International*, vol. 39, pp. 585-593, 2006

- [88] T.Y. Yu and O. Büyüköztürk, "A far-field airborne radar NDT technique for detecting debonding in GFRP-retrofitted concrete structures", *NDT&E International*, vol. 41, pp. 10–24, 2008
- [89] A.S.B. Sediq and N.Qaddoumi, "Near-field microwave image formation of defective composites utilizing open-ended waveguides with arbitrary cross sections", *Composite Structures*, vol. 71, Issues 3-4, pp. 343-348, 2005
- [90] A. McClanahan, S. Kharkovsky, A. R. Maxon, R. Zoughi and D. D. Palmer, Jr., "Depth evaluation of shallow surface cracks in metals using rectangular waveguides at millimeter-wave frequencies", *IEEE Transactions on instrumentation and measurement*, vol. 59, No. 6, pp.1693-1704, 2010
- [91] M. Abou-Khousa, S. Kharkovsky and R. Zoughi, "Novel near-field millimeter wave differential probe using a dual-loaded modulated aperture," *IEEE Transactions on Instrumentation and Measurement*, vol. 58, no. 5, pp. 1273-1282, 2009
- [92] S. Kharkovsky, A.C. Ryley, V. Stephen and R. Zoughi, "Dual-polarized near-field microwave reflectometer for non-invasive inspection of carbon fiber reinforced polymer (CFRP)-strengthened structures," *IEEE Transactions on Instrumentation and Measurement*, vol. 57, no. 1, pp. 168-175, 2008
- [93] M.T. Ghasr, D. Pommerenke, J.T. Case, A.D. McClanahan, A. Aflaki-Beni, M. Abou-Khousa, S. Kharkovsky, K. Guinn, F. DePaulis and R. Zoughi, "Rapid Rotary Scanner and Portable Coherent Wideband Q-Band Transceiver for High-Resolution Millimeter Wave Imaging Applications", *IEEE Transactions on Instrumentation and Measurement*, vol. 60, no. 1, pp. 186-197, 2011
- [94] S. Kharkovsky, M.T. Ghasr and R. Zoughi, "Near-field millimeter wave imaging of exposed and covered fatigue cracks" *IEEE Transactions on Instrumentation and Measurement*, vol. 58, no. 7, pp. 2367-2370, 2009
- [95] C. Yeh and R. Zoughi, "A novel microwave method for detection of long surface cracks in metals," *IEEE Trans. Instrum. Meas.*, vol. 43, no. 5, pp. 719–725, 1994
- [96] C. Huber, H. Abiri, S. Ganchev, and R. Zoughi, "Modeling of surface hairline-crack detection in metals under coatings using open-ended rectangular waveguides," *IEEE Trans. Microw. Theory Tech.*, vol. 45, no. 11, pp. 2049–2057, 1997
- [97] F. Mazlumi, S. H. H. Sadeghi, and R. Moini, "Interaction of an open-ended rectangular waveguide probe with an arbitrary-shape surface crack in a lossy

- conductor,” *IEEE Trans. Microw. Theory Tech.*, vol. 54, no. 10, pp. 3706–3711, Oct. 2006
- [98] M.T. Ghasr, M.A. Abou-Khousa, S. Kharkovsky, R. Zoughi, and D. Pommerenke, “Portable Real-Time Microwave Camera at 24 GHz”, *IEEE Transactions on Antennas and Propagation*, vol. 60, No. 2, pp. 1114-1125, 2012
- [99] N.P. Avdelidis, B.C. Hawtin and D.P. Almond, “Transient thermography in the assessment of defects of aircraft composites”, *NDT&E International*, vol. 36, pp. 433-439, 2003
- [100] N.P. Avdelidis and D.P. Almond, "Through skin sensing assessment of aircraft structures using pulsed thermography", *NDT & E International*, vol. 37, pp. 353-359, 2004
- [101] J. Liu, Q. Tang and Y. Wang, “The study of inspection on SiC coated carbon-carbon composite with subsurface defects by lock-in thermography”, *Composites Science and Technology*, vol. 72, Issue 11, pp. 1240-1250, 2012
- [102] C. Ibarra-Castenedo, J.-M. Piau, S. Guilbert, N.P. Avdelidis, M. Genest, A. Bendada, X.P.V. Maldague, “Comparative study of active thermography techniques for the nondestructive evaluation of honeycomb structures”, *Research in Nondestructive Evaluation Journal*, vol. 20, no. 1, pp. 1–31, 2009
- [103] R. Mulaveesala and S. Tuli, "Theory of frequency modulated thermal wave imaging for non-destructive sub-surface defect detection", *Applied Physics Letters*, vol. 89, No.19, pp. 191913 - 191913-3, 2006
- [104] M. Morbidini and P. Cawley, “The detectability of cracks using sonic IR”, *J. Appl. Phys.*, vol. 105, 093530, doi: 10.1063/1.3125444, 2009
- [105] X. Han and Y. Song, “Study the effect of engagement force of ultrasound transducer on crack detectability in sonic IR imaging”, *AIP Conf. Proc.* vol. 1511, 532, doi:10.1063/1.4789093, 2013
- [106] X. Han, L.D. Favro and R.L. Thomas, “Sonic IR imaging of delaminations and disbonds in composites”, *J. Phys. D: Appl. Phys.* vol. 44, 034013(5pp.), 2011
- [107] S.X. Zhao, X. Han, L.D. Favro, G. Newaz and R.L. Thomas, “Composite delamination depth profiling in sonic-IR imaging”, *AIP Conf. Proc.* vol. 1430, 533, doi: 10.1063/1/4716273, 2012
- [108] N.P. Avdelidis, E.T. Delegou, D.P. Almond and A. Moropoulou, “Surface roughness evaluation of marble by 3D laser profilometry and pulsed thermography”, *NDT&E International*, vol. 37, pp. 571-575, 2004



- [109] A. Rashed, D.P. Almond, D.A.S. Rees, S. Burrows and S. Dixon, “Crack detection by laser spot imaging thermography”, *AIP Conf. Proc.* vol 894, 500, doi: 10.1063/1.2718013, 2007
- [110] J. Schlichting, Ch. Maierhofer and M. Kreutzbruck, “Crack sizing by laser excited thermography”, *NDT&E International*, vol. 45, pp. 133-140, 2012
- [111] E. Kuhn, E. Valot and P. Herve, “A comparison between thermosonics and thermography for delamination detection in polymer matrix laminates”, *Composite Structures*, vol. 94, pp. 1155-1164, 2012
- [112] I.Z. Abidin, G.Y. Tian, J. Wilson, S. Yang and D. Almond, “Quantitative evaluation of angular defects by pulsed eddy current thermography”, *NDT & E International*, vol. 43, Issue 7, pp. 537-546, 2010
- [113] M. Noethen, Klaus-Jürgen Wolter and Norbert Meyendorf, “Surface crack detection in ferritic and austenitic steel components using inductive heated thermography”, *33rd International Spring Seminar on Electronics Technology (ISSE)*, pp. 249 – 254, 2010
- [114] B. Oswald-Tranta and G. Wally, “Thermo-inductive surface crack detection in metallic materials”, *9th European Conference on NDT*, Berlin, We.3.8.3, 2006
- [115] S. Yang, G.Y. Tian, I.Z. Abidin and J. Wilson, “Simulation of edge cracks using pulsed eddy current stimulated thermography”, *Journal of Dynamic Systems, Measurement, and Control*, vol. 133, 011008, 2011
- [116] B. Ramdane, D. Trichet, M. Belkadi and J. Fouladgar, “3-D numerical modelling of the thermo-inductive technique using shell elements”, *IEEE Transactions on Magnetics*, vol. 46, No. 8, pp. 3037-3040, 2010
- [117] Y. He, M. Pan and F. Luo, “Defect characterisation based on heat diffusion using induction thermography testing”, *Review of Scientific Instruments*, vol. 83, Issue 10, pp. 104702-104702-10, 2012
- [118] S.M. Shepard, T. Ahmed, B.A. Rubadeux, D. Wang and J.R. Lhota, “Synthetic processing of pulsed thermographic data for inspection of turbine components”, *Insight*, vol. 43, No. 9, pp. 587-589, 2001
- [119] D.L. Balageas, “Thickness or diffusivity measurements from front-face flash experiments using the TSR (thermographic signal reconstruction) approach”, *10<sup>th</sup> International Conference on Quantitative InfraRed Thermography*, Quebec, Canada, July, 2010

- [120] S. Quek and D.P. Almond, "Defect detection capability of pulsed transient thermography", *Insight- Non-Destructive Testing and Condition Monitoring*, vol. 47, No. 4, pp. 212-215, 2005
- [121] J.-M. Roche, D. Balageas, B. Lamboul, G. Bai, F. Passilly, A. Mavel and G. Grail, "Passive and active thermography for in situ damage monitoring in woven composites during mechanical testing", *AIP Conference Proceedings*, vol. 1511, pp. 555-562, 2012
- [122] B.K.P. Horn and B.G. Schunck, "Determining optical flow," *Artificial Intell.*, vol. 17, pp. 185–203, 1981
- [123] V. Beushausen, K. Roetmann, W. Schmunk, M. Wellhausen, C. Garbe, and B. Jähne, "2D-Measurement Technique for Simultaneous quantitative determination of mixing ratio and velocity field in microfluidic applications", *Imaging Measurement Methods*, NNFM 106, pp. 155–164, 2009
- [124] Y.M.C. Delaure, V.S.S. Chan, D.B. Murray, "A simultaneous PIC and heat transfer study of bubble interaction with free convection flow", *Experimental Thermal and Fluid Science*, pp. 911–926, 2003
- [125] Q. Duan, E. Angelini, S. Homma and A. Laine, "Validation of optical flow for quantification of myocardial deformations on simulated rt3d ultrasound", *ISBI 2007*
- [126] Q. Duan, K.M. Parker, A. Lorsakul, E.D. Angelini, E. Hyodo, S. Homma, J.W. Holmes, and A.F. Laine, "Quantitative validation of optical flow based myocardial strain measures using sonomicrometry", *ISBI*, 2009
- [127] A. Rochel, D. Ziou and M.F. Auclair-Fortier, "Computational Algebraic Topology-Based Video Restoration", *Image and Cideo Communications and Processing Proceeding*, San Jose, CA, vol. 5685, doi:10.1117/12.586874, 2005
- [128] J. P. Lindemann, R. Kern, J. H. van Hateren, H. Ritter, and M. Egelhaaf, "On the Computations Analyzing Natural Optic Flow-quantitative model analysis of the blowfly motion vision pathway", *The Journal of Neuroscience*, vol. 25, No. 27, pp. 6435– 6448, 2005
- [129] J. L. Barron, D. J. Fleet, and S. Beauchemin, "Performance of optical flow techniques," *Int. J. Comput. Vis.*, vol. 12, no. 1, pp. 43–77, 1994
- [130] T. Gautama and M. M. Van Hulle, "A phase-based approach to the estimation of the optical flow field using spatial filtering", *IEEE Transactions on Neural Networks*, vol. 13, No. 5, pp. 1127-1136, 2002

- [131] T. Brox, A. Bruhn, N. Papenberg and J. Weickert, "High Accuracy Optical Flow Estimation Based on a Theory for Warping", *ECCV 2004 In Proc. 8th European Conference on Computer Vision*, Springer LNCS 3024, vol. 4, pp. 25-36, 2004
- [132] R. Chaudhry, A. Ravichandran, G. Hager and R. Vidal, "Histograms of oriented optical flow and Binet-Cauchy kernels on nonlinear dynamical systems for the recognition of human actions", *IEEE Conference on Computer Cision and Pattern Recognition, CVPR*, pp. 1932-1939, Jun 2009
- [133] H. Franco, A. Perea, E. Romero, and D. Rodriguez, "Fluid flow measurement in thermographic video sequences", *ACIVS 2008*, LNCS 5259, pp. 310–321, 2008
- [134] M. Svantner, P. Vacikova and M. Honner, "IR thermography heat flux measurement in fire safety applications", *Infrared Physics & Technology* 55, pp. 292–298, 2012
- [135] H.W. Haussecker, "Simultaneous estimation of optical flow and heat transport in infrared image sequences", *IEEE Workshop on Computer Cision Beyond the Cisible Spectrum: Methods and Applications*, pp. 85-93, 2000
- [136] S Marinetti, E Grinzato, P G Bison, E Bozzi, M Chimenti, G Pieri and O Salvetti, "Statistical analysis of IR thermographic sequences by PCA," *Infrared Physics & Technology*, vol. 46, pp, 85-91, 2004
- [137] A.A. Khan, V. Vrabie, J.I. Mars, A. Girard and G.D. Urso, "A source separation technique for processing of thermometric data from fiber-optic DTS measurement for water leakage identification in dikes," *IEEE Sensors Journal*, vol. 8, no. 7, pp. 1118-1129, 2008
- [138] N Rajic, "Principal component thermography for flaw contrast enhancement and flaw depth characterisation in composite structures," *Composite Structures*, vol. 58, pp. 521-528, 2002
- [139] G. Yang, G.Y. Tian, P.W. Que and T.L. Chen, "Independent component analysis-based feature extraction technique for defect classification applied for pulsed eddy current NDE", *Research in Nondestructive Evaluation*, vol. 20, pp. 230-245, 2009
- [140] L. Bai, B. Gao, G.Y. Tian, W.L. Woo and Y. Cheng, "Spatial and time patterns extraction of eddy current pulsed thermography using blind source separation", *IEEE sensors Journal*, 2013, in publication
- [141] Electromagnetic Testing, Nondestructive Testing Handbook, 3<sup>rd</sup> Edition, Vol. 5. ASNT Press, ISBN 1-57117-116-9, 2004

- [142] J. Dong, "Microwave lens designs: optimization, fast simulation algorithms, and 360-degree scanning techniques", PhD dissertation, Virginia Polytechnic Institute and State University, Sep. 2009
- [143] J. Van hese, J. Sercu, D. Pissoort and H. S. Lee, "State of the art in EM software for microwave engineers", white paper, available at <http://cp.literature.agilent.com/litweb/pdf/5990-3225EN.pdf>
- [144] T. Weiland, "Time domain electromagnetic field computation with finite difference methods," *Int. J. Numer. Model.*, vol. 9, no. 4, pp. 295–319, 1996
- [145] T. Weiland, M. Timm and I. Munteanu, "A practical guide to 3-D simulation", *IEEE Microwave Magazine*, vol. 9, issue 6, pp.62-75, 2008
- [146] Bin Gao, W.L. Woo, S.S. Dlay, "Adaptive Sparsity Non-negative Matrix Factorization for Single Channel Source Separation", *IEEE Journal of Selected Topics in Signal Processing*, vol. 5, pp. 1932-4553, 2011
- [147] G. Y. Tian, A. Sophian, D. Taylor, and J. Rudlin, "Wavelet-based PCA defect classification and quantification for pulsed eddy current NDT," in *IEE Proceedings: Science, Measurement and Technology*, pp. 141-148, 2005
- [148] A. Sophian, G. Y. Tian, D. Taylor, and J. Rudlin, "A feature extraction technique based on principal component analysis for pulsed Eddy current NDT," *NDT and E International*, vol. 36, pp. 37-41, 2003
- [149] J. Bobin, Y. Moudden, J.\_L. Starch and M. Elad, "Morphological diversity and source separation", *IEEE Signal Processing Letters*, vol. 13, Issue 7, pp. 409-412, 2006
- [150] H. Menana and M. Féliachi, "3-D Eddy Current Computation in Carbon-Fiber Reinforced Composites", *IEEE Transactions on Magnetics*, vol. 45, No. 3, pp.1008-1011, 2009
- [151] J. K. Humphrey, A. G. Gibson, J. Carruthers and M. Tobinson, "Carbon fibre reinforced plastic (CFRP) thermal diffusivity measurements", *Graduate Conference 2010, School of Mechanical and Systems Engineering*, Newcastle University, Newcastle upon Tyne, UK, 2010
- [152] J. Wilson, G. Y. Tian, I. Z. Abidin, S. Yang and D. Almond, "Modelling and evaluation of eddy current stimulated thermography", *Nondestr. Test. Eval.*, vol. 25, No. 3, pp. 205-218, 2010.
- [153] S. Yang, G. Y. Tian, I. Z. Abidin and J. Wilson, "Simulation of edge cracks using pulsed eddy current stimulated thermography", *Journal of Dynamic Systems, Measurement, and Control*, vol. 133, pp. 011008.1-011008.6, 2011

- 
- [154] D. P. Pritzkau, *RF pulsed heating*, Ph.D. thesis, Stanford, CA 94309, 2001.
- [155] W.J. Parker, R.J. Jenkins, C.P. Butler, and G.L. Abbott, "Flash method of determining thermal diffusivity, heat capacity, and thermal conductivity," *J. Appl. Phys.*, vol. 32, pp. 1679–1684, 1961
- [156] H.S. Carslaw and J.C. Jaeger, *Conduction of heat in solids*. 2nd ed. Oxford University Press; 1959
- [157] S. S. Wicks, R. G. de Cilloria and V. L. Wardle, "Tomographic electrical resistance-based damage sensing in nano-engineered composite structures", *51st AIAA/ASME/ASCE/AHS/ASC Structures, Structural Dynamics and Materials Conference*, 2010
- [158] L. Hou and S. A. Hayes, "A resistance-based damage location sensor for carbon-fibre composites", *Smart Mater. Struct.*, vol. 11, pp. 966-969, 2002
- [159] M. Morozov, G.Y. Tian, and P.J. Withers, "Noncontact evaluation of the dependency of electrical conductivity on stress for various Al alloys as a function of plastic deformation and annealing", *J. Appl. Phys.*, 108, 024909, 2010
- [160] C. Bugli and P. Lambert, "Comparison between principal component analysis and independent component analysis in electroencephalogram modelling", *Biometrical Journal*, vol. 48, No. 5, pp. 1-16, 2006
- [161] N.J. Loh, T.C. Hou, J.P. Lynch and N.A. Kotov, "Carbon nanotube sensing skins for spatial strain and impact damage identification", *J. Nondestruct Eval.*, vol. 28, pp. 9-25, 2009.